Microscopic Theory of Supercapacitors

A DISSERTATION
SUBMITTED TO THE FACULTY OF THE GRADUATE SCHOOL
OF THE UNIVERSITY OF MINNESOTA
BY

Brian Joseph Skinner

IN PARTIAL FULFILLMENT OF THE REQUIREMENTS
FOR THE DEGREE OF
Doctor of Philosophy

BORIS I. SHKLOVSKII

August, 2011

Acknowledgements

I have, throughout my life, been the beneficiary of great kindness and great patience. For my successful upbringing and education I have an uncountable number of family members and friends to whom I am deeply indebted.

For the successful completion of this thesis I have most directly to thank my parents, for showing me that the world is a wonderful place, and my advisor, for teaching me that science is a matter of imagination.

Chapters 2 and 5 of this thesis represent a collaborative effort with M. M. Fogler. Chapter 3 is a collaboration with M. S. Loth, and Chapter 4 is a collaboration with M. S. Loth and Tianran Chen.

Abstract

As new energy technologies are designed and implemented, there is a rising demand for improved energy storage devices. At present the most promising class of these devices is the electric double-layer capacitor (EDLC), also known as the supercapacitor. A number of recently created supercapacitors have been shown to produce remarkably large capacitance, but the microscopic mechanisms that underlie their operation remain largely mysterious. In this thesis we present an analytical, microscopic-level theory of supercapacitors, and we explain how such large capacitance can result.

Specifically, we focus on four types of devices that have been shown to produce large capacitance. The first is a capacitor composed of a clean, low-temperature two-dimensional electron gas adjacent to a metal gate electrode. Recent experiments have shown that such a device can produce capacitance as much as 40% larger than that of a conventional plane capacitor. We show that this enhanced capacitance can be understood as the result of positional correlations between electrons and screening by the gate electrode in the form of image charges. Thus, the enhancement of the capacitance can be understood primarily as a classical, electrostatic phenomenon. Accounting for the quantum mechanical properties of the electron gas provides corrections to the classical theory, and these are discussed. We also present a detailed numerical calculation of the capacitance of the system based on a calculation of the system's ground state energy using the variational principle. The variational technique that we develop is broadly applicable, and we use it here to make an accurate comparison to experiment and to discuss quantitatively the behavior of the electrons' correlation function.

The second device discussed in this thesis is a simple EDLC composed of an ionic liquid between two metal electrodes. We adopt a simple description of the ionic liquid and show that for realistic parameter values the capacitance can be as much as three times larger than that of a plane capacitor with thickness equal to the ion diameter. As in the previous system, this large capacitance is the result of image charge formation in the metal electrode and positional correlations between discrete ions that comprise the electric double-layer. We show that the maximum capacitance C_{max} scales with the

temperature T as $C_{max} \propto T^{-1/3}$ and that at moderately large voltage V the capacitance decays as $C \propto V^{-1/3}$. These results are confirmed by a Monte Carlo simulation.

The third type of device we consider is that of a porous supercapacitor, where the electrode is made from a conducting material with a dense arrangement of narrow, planar pores into which ionic liquid can enter when a voltage is applied. In this case we show that when the electrode is metallic the narrow pores aggressively screen the interaction between neighboring ions in a pore, leading to an interaction energy between ions that decays exponentially. This exponential interaction between ions allows the capacitance to be nearly an order of magnitude larger than what is predicted by mean-field theories. This result is confirmed by a Monte Carlo simulation. We also present a theory for the capacitance when the electrode is not a perfect metal, but has a finite electronic screening radius. When this screening radius is larger than the distance between pores, ions begin to interact across multiple pores and the capacitance is determined by the Yukawa-like interaction of a three-dimensional, correlated arrangement of ions.

Finally, we consider the case of supercapacitor electrodes made from a stack of graphene sheets with randomly-inserted "spacer" molecules. For such devices, experiments have produced very large capacitance despite the small density of states of the electrode material, which would seem to imply poor screening of the ionic charge. We show that these large capacitance values can be understood as the result of collective entrance of ions into the graphene stack (GS) and the renormalization of the ionic charge produced by nonlinear screening. The collective behavior of ions results from the strong elastic energy associated with intercalated ions deforming the GS, which creates an effective attraction between them. The result is the formation of "disks" of charge that enter the electrode collectively and have their charge renormalized by the strong, nonlinear screening of the surrounding graphene layers. This renormalization leads to a capacitance that at small voltages has the form $C \propto V$ and is enhanced over mean-field predictions by a large factor proportional to the number of ions within the disk to the power 9/4. At large voltages, the capacitance is dictated by the physics of graphite intercalation compounds and adopts the form $C \propto V^{-4/5}$. We also examine theoretically the case where the fine structure constant α of the GS is a small parameter, and we uncover a wealth of scaling regimes.

Contents

List of Tables

List of Figures

Chapter 1

Introduction

1.1 The need for a theory of supercapacitors

When considering humanity's long-term use of energy resources, a twofold dilemma becomes apparent. First, the vast majority of our energy currently comes from non-renewable sources, including nuclear and fossil fuels, the latter of which could easily be depleted in the next hundred years or so if we continue to consume it at the current rate [1]. Second, there is growing evidence that human use of fossil fuels is significantly altering the global climate [2, 3]. Eventually, these two problems must be solved by the development of new energy technologies, such as improved photovoltaic devices [4].

As new energy conversion technologies are created to address our energy problems, and as the global demand for energy rises, there is an increased need for new and more efficient energy storage devices [4, 5]. At present the most important of these are electrical energy storage devices, *i.e.* batteries and capacitors. Typically, batteries are able to store more energy per unit volume or per unit mass than capacitors, while capacitors offer the benefit of faster charging/discharging times and much longer life cycles. These benefits, along with improved reliability and reduced environmental risks, have stimulated in recent years a significant amount of research into improved capacitors. Among new capacitor technologies, the most promising class of devices is the electrochemical double-layer capacitor (EDLC), also called a "supercapacitor" or

"ultracapacitor" [5, 6, 7].[1] Thanks to recent research efforts, the energy storage capacity of supercapacitors has improved to the point that they are replacing batteries in a number of applications, including cranes and electric buses [7] and in backup power applications for wind turbines, the Toyota Prius, and the Airbus 380 [8].

The basic idea behind the operation of an EDLC is as follows. Suppose that a pair of large, parallel, planar metal electrodes is placed on either side of a solution containing mobile ions and then the electrodes are attached to opposite terminals of a voltage source. As a voltage V is applied between the electrodes, the resulting electric field drives positive/negative ions to the negative/positive electrode, so that the electronic charge $\pm Q$ on each electrode is compensated by an equal and opposite ionic charge. This situation is shown schematically in Fig. 1.1. The layer of ionic charge that accumulates at each electrode is referred to as the "electric double-layer" (EDL), and has been a subject of study in physics ever since a seminal paper by Hermann von Helmholtz in 1853 [9] (for an English translation, see Ref. [10]). In an EDLC, as in a conventional capacitor, energy is stored in the strong electric fields that are present in the electric double-layer. The EDLC releases its energy through discharge of the capacitor, wherein the electronic charge is allowed to flow out from the electrodes and through an external electrical circuit, at which point the ions comprising the EDL return to the bulk of the ionic solution. It is through this reversible process that the capacitor can be discharged and recharged, indefinitely, at a rate that is limited only by the electrical conductivity of the ionic solution.

The ability of any capacitor to store charge is characterized by its differential capacitance $C = dQ/dV$; the primary focus of this thesis is the theoretical calculation of C for a number of devices. In order to estimate the capacitance of the simple EDLC described above, one can imagine that neutralizing ions within the double-layer approach the charged electrode surfaces as closely as possible in order to minimize the system's electrostatic energy. In this way the ions form a flat layer of charge adjacent to the electrode surface, as shown in Fig. 1.1. This configuration is apparently similar to a conventional parallel plate capacitor – in fact, two such capacitors are formed, one at either electrode surface, and they are connected in series through the conducting

[1] In this thesis, the term "supercapacitor" is used to refer both to the specific type of devices discussed in Refs. [5, 6, 7], which exhibit large capacitance per unit volume, and more generally to any capacitor with anomalously large capacitance.

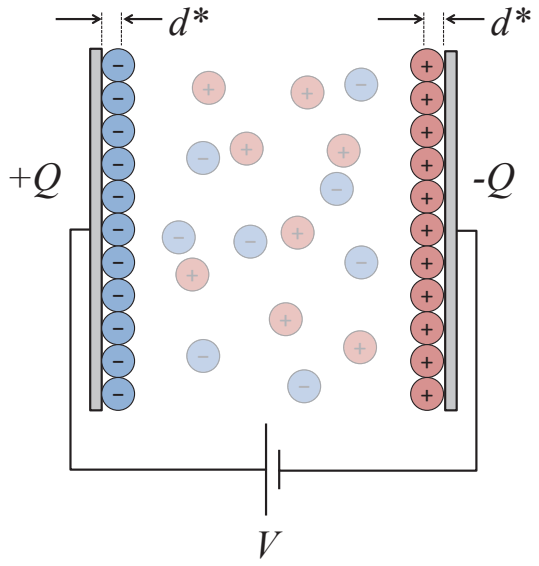

Figure 1.1: A schematic picture of a simple EDLC. When a voltage V is applied between the two electrodes, $+/-$ ions from the intervening solution are attracted to the $-/+$ electrodes, effectively forming two series-connected capacitors of thickness d^* on either side.

bulk of the ionic solution. One can think, therefore, that the capacitance of a given electrode/ion interface can be estimated as being equal to the capacitance of a plane capacitor:

$$C = \frac{\varepsilon_0 \varepsilon A}{d^*}, \tag{1.1}$$

where ε_0 is the permittivity of free space, ε is the dielectric constant of the ionic solution, A is the electrode area, and d^* is the capacitor thickness. This standard equation immediately implies that in order to produce large capacitance one should construct a device with high dielectric constant, large area, and small thickness.

Given the picture in Fig. 1.1, it is natural to think that the effective thickness d^* of the capacitor formed at each electrode can be no smaller than the radius $a/2$ of the ions themselves, and therefore that the capacitance must always be smaller than

$$C_H = \frac{2\varepsilon_0 \varepsilon A}{a}. \tag{1.2}$$

If the ions have finite thermal energy, for example, it is natural to expect that the thickness of the capacitor increases due to the ions "jumping" thermally away from

the electrode. This idea, that d^* must satisfy $d^* \leq a/2$, or in other words that the capacitance per electrode cannot exceed $C_H = \varepsilon_0 \varepsilon A/(a/2)$, is a universal conclusion of mean-field theories of double-layer capacitance [6, 11, 12].

However, the picture in Fig. 1.1, and therefore the applicability of Eq. (1.1), becomes questionable in a number of situations. For example, if the ions covering the electrode are sparse, then one cannot in general say that they form a uniform plane of charge. Further, in many EDLC devices the charged surfaces cannot be described as planes at all, but rather consist of tortuous pores within the volume of a bulk conductor. Finally, EDLC electrodes are usually not made from perfect metals, but rather from carbons or other materials where the quantum behavior of the conducting electrons must be taken into account. For such cases, which are highly relevant to the operation of real devices, a different paradigm from that of Fig. 1.1 is needed.

In order to begin to address these problems, we must first adopt a definition of the capacitance that goes beyond the plane capacitor formula. In the following chapters we employ a thermodynamic definition of capacitance, rather than viewing capacitance simply as a proportionality relation between the charge of the system and the electric potential across it. Indeed, this second, more familiar concept is not always well-defined, since in problems where the discreteness of charge is important the electric potential is not uniform across any meaningful surface or volume. The more general thermodynamic definition of capacitance can easily be understood as follows. Consider a system that can be charged in some way by an external source – this is the capacitor. When a total amount of charge Q is introduced to the system, the charges (electrons or ions) rearrange themselves so as to arrive at their minimum energy configuration, which corresponds to some total energy $U(Q)$ relative to the uncharged state. This energy $U(Q)$ is the energy stored by the capacitor. The charging process is driven by the external voltage source, which operates with a fixed, constant voltage V. In charging the capacitor, the voltage source expends some energy $-QV$, which is referred to as the "source work". The system "decides" how much charge should be moved from the source to the capacitor by finding the value of Q which optimizes the energy of the entire system (capacitor + source), $U - QV$. In other words, the equilibrium value of Q is determined by the relation $d(U - QV)/dQ = 0$. This immediately leads to a relation between the voltage

and the charge:

$$V = \frac{dU}{dQ}. \tag{1.3}$$

Using the definition of capacitance $C = dQ/dV = (dV/dQ)^{-1}$ gives a similar relation for the capacitance in terms of the total energy U:

$$C = \left(\frac{d^2U}{dQ^2}\right)^{-1}. \tag{1.4}$$

In this way the capacitance is a unique property of the thermodynamic ground state of the system. Notice that the standard plane capacitor formula, $C = \varepsilon_0\varepsilon A/d$, can be recovered from Eq. (1.4) by calculating the total energy stored in the electric field $\vec{E}$ between two parallel plates with uniform charge Q and area A. This gives $U = (\varepsilon_0\varepsilon/2)\cdot|\vec{E}|^2\cdot Ad = Q^2d/2\varepsilon_0\varepsilon A$, so that the inverse second derivative of U indeed gives the proper result.

Eqs. (1.3) and (1.4) are general relations, and they will be employed throughout the following chapters. They assume only that the charging/discharging process of the capacitor is slow enough that the system has ample time to reach its thermodynamic ground state. Equivalently, one can say that all results in this thesis correspond to the low-frequency limit. In situations where entropic, finite-temperature effects are important, the energy U in Eqs. (1.3) and (1.4) should be replaced by the system's *free* energy F. Thus, the capacitance of a system can be thought of as equivalent to its "charge compressibility" or "charge susceptibility"; it is uniquely determined by the system's free energy. Understanding the behavior of an EDLC is therefore a problem that falls squarely in the domain of equilibrium statistical physics.

In this way, the description of large-capacitance devices raises an interesting set of questions in fundamental physics. Most prominent among these is: what determines the fundamental limit of the capacitance? How large can the capacitance be? In this thesis we report on a number of novel theoretical investigations aimed at addressing these questions for a variety of different capacitor devices. These investigations show that, in many cases, the essential physics of large capacitance devices can only be understood by considering the structure of the double-layer at the level of individual charges. As will be shown below, the screened nature of the Coulomb interaction between charges and the strong positional correlations between them produce results that are significantly

different from conventional, mean-field theories. Further, inclusion of these effects allows the capacitance to be much larger than the simple picture of Fig. 1.1 suggests. It is the main result of this thesis that the capacitance of a device is not fundamentally limited by the physical separation between the electrode and its countercharge, a result which can only be understood by microscopic-level, non-mean-field theories.

In the following section, we briefly review the main conclusions of the thesis, which are developed over the course of Chapters 2 – 5. The majority of the discussion of previous literature on these topics is reserved for the relevant chapters.

1.2 Main results of this thesis

In essence, all of the theories of large capacitance presented in this thesis follow the same general, two-component recipe. The first component is the description of capacitor charges as discrete objects whose repulsive interaction leads to positional correlations. The second component is the inclusion of electronic screening effects by the conducting electrode. Taken together, these two ingredients are sufficient to explain capacitance that is enhanced over the traditional "plane capacitor" formula of Eq. (1.1) and over all mean-field results in general.

In order to elucidate the way in which correlations and electronic screening together produce large capacitance, in Ch. 2 this thesis first considers a simple, clean, experimentally viable system – namely, a capacitor made from a low temperature, two-dimensional electron gas (2DEG) separated by a distance d from a conducting electrode. Such a device, shown schematically in Fig. 1.2, was recently examined experimentally [13] and shown to have a capacitance significantly larger than the plane capacitor result of Eq. (1.1) when the density n of the 2DEG is small. We explain this result by means of a simple, classical calculation and then confirm its validity with a more accurate, quantum-mechanical calculation.

The main results of Ch. 2 can be summarized as follows. When the 2DEG is sufficiently sparse that every electron is separated from its neighbors by a distance larger than the effective size a_B of its quantum wave function, then the electrons within the 2DEG can be treated as classical point charges. (Here, a_B is the effective electron Bohr radius.) In this sparse limit every electron makes for itself an electrostatic image charge

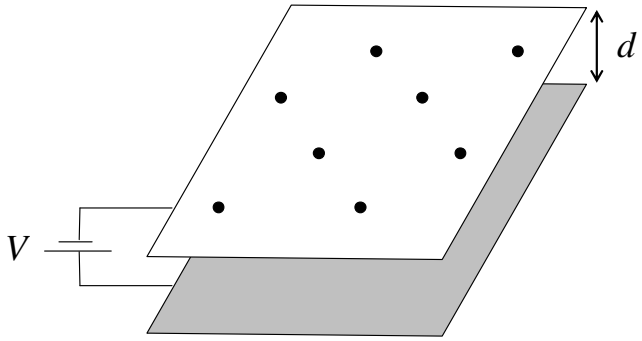

Figure 1.2: Schematic picture of the system studied in Ch. 2. A two-dimensional electron gas (black circles) is separated from a metal electrode by a distance d from a metal electrode (gray rectangle). The electrode and 2DEG are coupled by a voltage source with voltage V.

in the surface of the nearby metal electrode. Thus, the capacitor is best described not as two uniform planes of charge but as an arrangement of electron-image dipoles with dipole arm $2d$. When dipoles are sparse enough that their concentration $n \ll 1/d^2$, then their repulsive interaction takes the weakened form $\sim e^2d^2/r^3$ rather than the normal Coulomb interaction $\sim e^2/r$. Through this screening, and aided by the positional correlations that are adopted by electrons as they maximize their separation from each other, the total energy is reduced and therefore the capacitance becomes larger than the plane capacitor result. Equivalently, one can say that the effective capacitor thickness d^* becomes smaller than the geometrical thickness d. A classical calculation of the energy of a lattice of dipoles gives at small density

$$d^* \simeq d \times 2.7\sqrt{nd^2}, \qquad (nd^2 \ll 1). \tag{1.5}$$

This equation implies that the capacitance becomes much larger than the geometric value when the electron density approaches zero. This surprising result can be seen as a consequence of the vanishing short-ranged interaction between dipoles as their separation becomes large. At large electron density $nd^2 \gtrsim 1$, d^* approaches the geometric value d. The result of this classical calculation is shown schematically by the dashed line in Fig. 1.3.

If the quantum mechanical properties of the electrons in the 2DEG are taken into

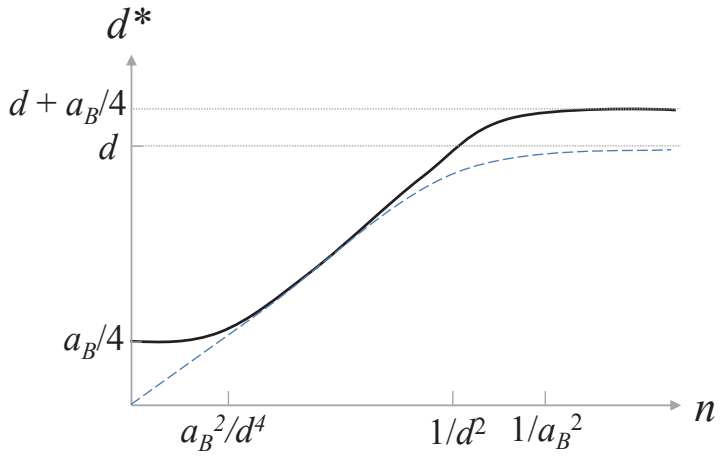

Figure 1.3: Schematic dependence of the effective capacitor thickness d^* on the electron concentration n for a parallel-plate capacitor made with a 2DEG next to a metal electrode. $d^* < d$ suggests that the capacitance is *enhanced* relative to the geometric value. The thin, dashed line shows the prediction of a classical calculation, whose low-density limit corresponds to Eq. (1.5), and the thick, black line incorporates quantum effects. The axes have been somewhat distorted to more clearly show the different scales of n and d^*.

account, then the total energy of the system becomes larger and the capacitance is somewhat reduced. In the range of electron densities $a_B^2/d^4 \ll n \ll 1/a_B^2$, quantum effects are relatively unimportant and the classical calculation of capacitance is accurate. At large concentrations, $n \gg 1/a_B^2$, electron wave functions overlap and the capacitance becomes equal to the geometric value minus a correction associated with the electrons' quantum kinetic energy. This gives $d^* \to d + a_B/4$. At very small concentrations, $n \ll a_B^2/d^4$, the Coulomb energy vanishes from the capacitance and only the quantum kinetic energy of electrons contributes. This gives a constant effective thickness $d^* = a_B/4$.

These results for the capacitance are confirmed by a more detailed calculation that makes use of the variational principle to determine the ground state energy of the system for arbitrary electron density n. The resulting capacitance compares favorably with experimental values [13]. We also use the variational method to examine the non-monotonic dependence of the strength of electron correlations on the electron density and to predict the dependence of the capacitance on electron spin polarization. The variational method we develop is applicable to a broad class of problems concerning

screened electron interactions in two or three dimensions.

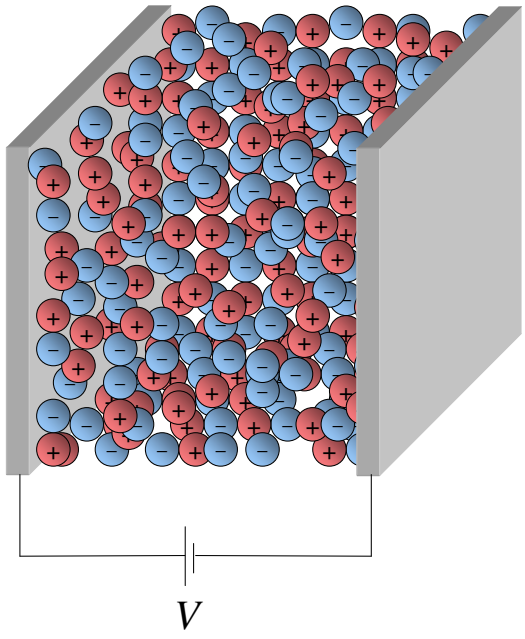

Figure 1.4: Schematic picture of the system studied in Ch. 3. A dense ionic liquid, modeled as a collection of hard spheres with charges $\pm e$, is placed between two metal electrodes with a voltage V applied between them.

In Ch. 3 we turn our attention to the simplest realistic model of an EDLC device. That is, we consider a pair of planar metal electrodes with an intervening layer of ionic liquid with high density, as shown schematically in Fig. 1.4. We focus on the "restricted primitive model" (RPM) of the ionic liquid, in which positive and negative ions are described as nonpolarizable hard spheres of equal size residing in a solventless environment. We employ a similar theory to the classical calculation presented in Ch. 2, describing the EDL at each electrode as a collection of correlated ion-image dipoles. We again find that $d^* \propto n^{1/2}$, which when expressed in terms of capacitor voltage gives a capacitance that is significantly larger than the Helmholtz value C_H given in Eq. (1.2):

$$\frac{C(V)}{C_H} \propto (V - V_t)^{-1/3}. \tag{1.6}$$

Here, V_t is the voltage at which the capacitor has zero charge. We also study the dependence of the capacitance on temperature. We show that when the applied voltage

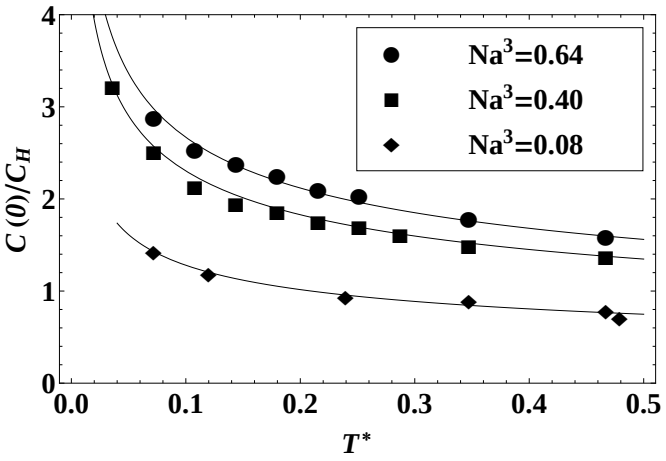

Figure 1.5: The zero-voltage capacitance of the double-layer formed at metal/ionic liquid interface as a function of temperature, plotted for different values of the ionic liquid density N. Solid lines are the theoretical prediction of Eq. (1.7), as derived in Sec. 3.3, and symbols are simulation data, as explained in Sec. 3.2. This figure is repeated in Sec. 3.2, where it is explained more fully.

is low, so that the density of ions in the EDL is small, positional correlations between distant ions are lost because of thermal motion and the capacitance is truncated at a finite maximum value. Using a simple argument we show that this maximum C_{max} occurs at zero voltage and scales as

$$C_{max} \propto T^{-1/3}. \tag{1.7}$$

The results of Eqs. (1.6) and (1.7) are confirmed with a Monte Carlo simulation. We use our simulation results to determine the relevant constants of proportionality and to propose a general form of the dependence of capacitance on both voltage and temperature, $C(V,T)$. We also briefly examine the case where the electrode is made from an imperfect metal and show that the experimental puzzle of a *minimum* capacitance at $V = 0$ for imperfectly-conducting electrodes can be understood. Simulation results for $C_{max}(T) = C(V = 0, T)$ are shown in Fig. 1.5 along with our theoretical prediction [Eq. (1.7)].

In real supercapacitor devices, charge is stored not at a single, planar electrode/ionic liquid interface but within a porous volume where there is a dense arrangement of many such interfaces. In Ch. 4 we examine such devices, focusing on the capacitance

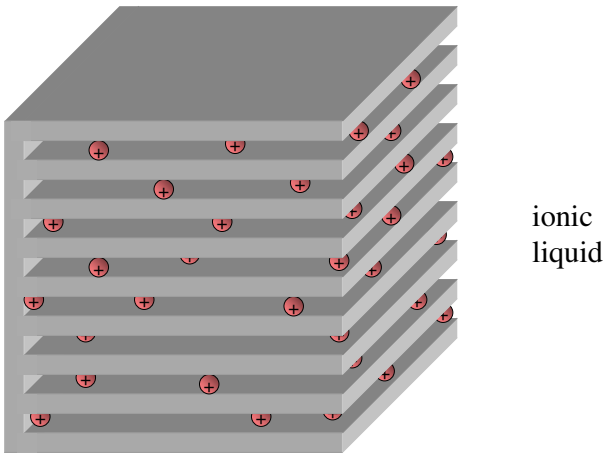

Figure 1.6: Schematic picture of the system studied in Ch. 4. A conducting supercapacitor electrode has a series of deep, planar pores. When a voltage is applied between the electrode and an external ionic liquid reservoir, ions are induced to enter the electrode's pores in order to neutralize the electronic charge.

per unit volume of an electrode with narrow, planar pores throughout its volume. A schematic picture is shown in Fig. 1.6. When the electrode is metallic, the electrode strongly screens the repulsive interaction between discrete ions that enter a given pore, making their repulsive interaction exponentially small. This small interaction allows for a capacitance per pore that is again much larger than the Helmholtz prediction C_H at small voltages. We show that at small $V - V_t$, the capacitance

$$\frac{C(V)}{C_H} \propto \frac{1}{(V - V_t)\ln^3[1/(V - V_t)]}. \tag{1.8}$$

This result is verified with a MC simulation, which includes an exploration of finite temperature effects. The primary theoretical and MC results are shown in Fig. 1.7.

Ch. 4 also examines the case where the electrode is not metallic, but rather has a finite Fermi level density of states $\nu(\mu_F)$. When $\nu(\mu_F)$ is small enough, the charge of a single ion is not screened within the thickness of one pore and ions begin to interact across multiple pores. In this case one can no longer talk about the capacitance per area of a single interface, and instead one should discuss the capacitance per unit volume of the electrode as a whole. We explore this idea and find that at large voltages the

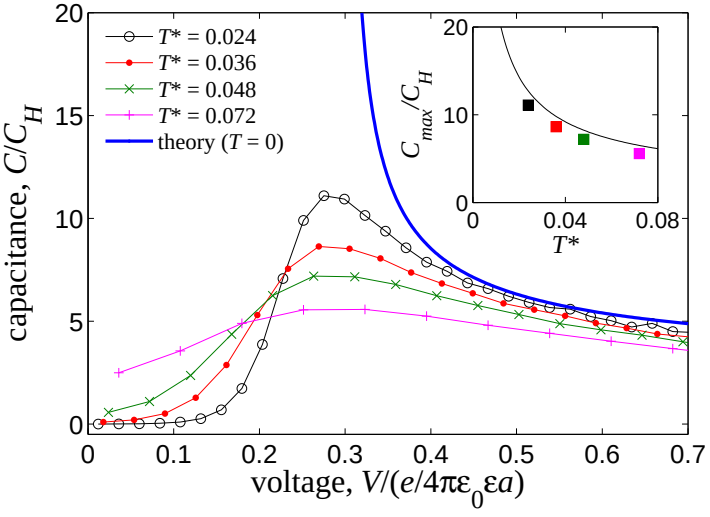

Figure 1.7: The capacitance C of ions within a narrow 2D pore of width $d = a$ can be much larger than the Helmholtz value C_H. This behavior is explained theoretically and confirmed by Monte Carlo simulations in Ch. 4. Different curves in this plot correspond to different values of the system temperature. The thick blue line is the theoretical prediction of Eq. (1.8). This figure is repeated in Sec. 4.3, where it is explained more fully.

capacitance is dominated by the quantum kinetic energy associated with uniformly raising the Fermi level in the electrode, which gives a capacitance per unit volume $\mathbb{C}$

$$\mathbb{C} = \frac{\varepsilon_0 \varepsilon}{R_s^2}, \tag{1.9}$$

where R_s is the screening radius determined by the volume-averaged density of states of the electrode. At small voltages, the capacitance is determined by the weak, Yukawa-like interaction between discrete ions that are three-dimensionally correlated, which gives

$$\mathbb{C}(V) \propto \frac{1}{(V - V_t)\ln^4[1/(V - V_t)]}. \tag{1.10}$$

The finite temperature behavior of this diverging capacitance at small voltage is also calculated.

Finally, in Ch. 5 we turn our attention to supercapacitors made from graphene. A number of high-performance supercapacitor devices have recently been made from stacks

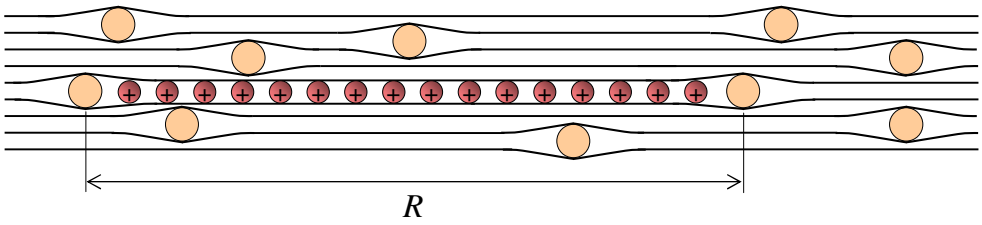

Figure 1.8: A schematic picture of a graphene-based electrode, as studied in Ch. 5. A stack of graphene layers (black lines) has some density of "spacer" molecules (filled, tan circles) in it with average in-plane separation R. When a voltage is applied, ions (filled, red circles with +'s) from an external reservoir intercalate into the GS in the form of disks of ionic charge. This figure is repeated in Sec. 5.2, where it is explained more fully.

of graphene sheets with randomly-inserted "spacer" molecules, as shown schematically in Fig. 1.8. Naïvely, one would expect that such a graphene stack (GS) capacitor should have a relatively poor capacitance, since graphene has a vanishing Fermi level density of states $\nu(\mu_F)$ and therefore usually does not screen electric charges very effectively. Indeed, in mean-field descriptions of a GS capacitor the large quantum kinetic energy of electrons in the graphene dominates the total energy and leads to a small capacitance $C \propto V$ over the entire range of voltage. Nonetheless, capacitors made from graphene have been shown experimentally to generate large capacitance even at small voltages.

We show that these surprisingly large capacitance values can be understood by first considering the strong elastic energy associated with deforming the GS around intercalated ions. This elastic energy produces an effective attraction between ions, so that as a consequence ions enter collectively in "disks" of ionic charge with some characteristic size R defined by the in-plane distance between spacer molecules. The nonlinear screening of the GS produces a strongly-bound screening atmosphere of electronic charge around each disk, which effectively *renormalizes* the ionic charge. This renormalization leads to a significantly weaker repulsion between disks which allows the capacitance to be large. The result at small voltages is a capacitance that increases linearly with voltage, as in the mean-field result, but with a greatly-enhanced slope:

$$C \propto R^{9/2} V, \qquad \left(V \ll \frac{e c^{3/2}}{\varepsilon_0 \varepsilon R^{5/2}} \right), \tag{1.11}$$

where c is the spacing between graphene sheets. This linear capacitance quickly reaches

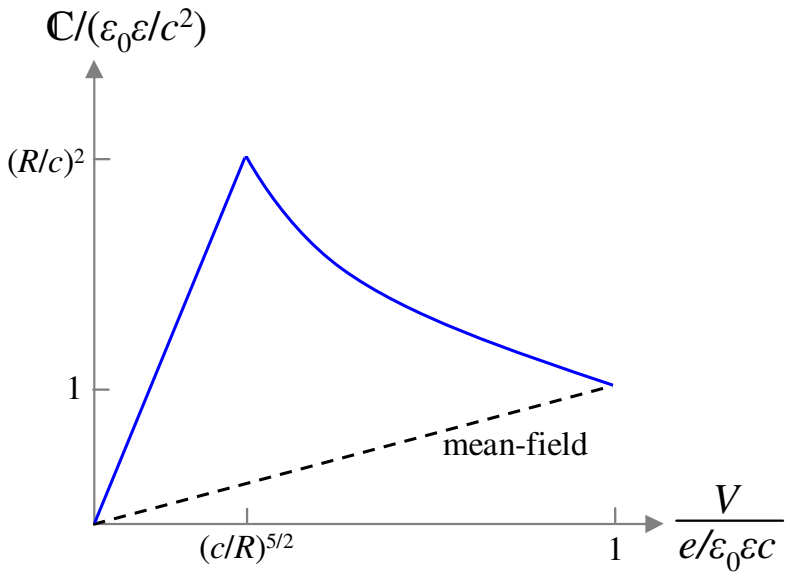

Figure 1.9: A schematic plot of the capacitance per unit volume $\mathbb{C}$ as a function of voltage in a graphene stack supercapacitor (blue line), showing large enhancement of the capacitance over the mean-field result (dashed black line). The low voltage portion of the curve is described by Eq. (1.11) and the high voltage portion corresponds to Eq. (1.12). A more detailed version of this figure is given in Sec. 5.5.

a maximum value $C_{max} \propto R^2$ before decaying at large voltages as

$$C \propto V^{-4/5}, \qquad \left(V \gg \frac{ec^{3/2}}{\varepsilon_0 \varepsilon R^{5/2}}\right), \tag{1.12}$$

a result that follows from the well-studied physics of graphite intercalation compounds. In this way the large capacitances observed in real devices can be understood. The dependence implied by Eqs. (1.11) and (1.12) is plotted schematically in Fig. 1.9.

Ch. 5 also explores theoretically situations where the effective fine structure constant α of graphene is a small parameter. We demonstrate a wealth of different scaling regimes associated with small α and map out the resulting C–V relationships.

Chapter 2

Capacitance of a plane capacitor with a two-dimensional electron gas

2.1 Introduction

In a standard parallel-plate capacitor, the capacitance C is equal to the "geometric capacitance" $C_g = \varepsilon_0 \varepsilon A/d$, where ε_0 is the vacuum permittivity, ε is the dielectric constant of the medium separating the two plates, A is the area of each plate, and d is the separation between them. The expression $C = C_g$ is correct when both electrodes are made from a "perfect" metal, which by definition screens electric field with a vanishing screening radius, so that the charge of a given electrode is located exactly on the electrode surface and the electric field from the opposite electrode does not penetrate into the metal. If one of the electrodes is made from a material with finite (positive) Debye screening radius R_s (for example, a doped bulk semiconductor), then the imperfect charge screening at this electrode allows the electric field to penetrate a distance R_s into the electrode and the capacitance decreases. If one describes the capacitance by the effective capacitor thickness $d^* = \varepsilon_0 \varepsilon A/C$, then the effect of positive screening radius is to increase the effective capacitor thickness from $d^* = d$ to $d^* = d + R_s$.

On the other hand, capacitors with $d^* < d$, or in other words with effective three-dimensional electrode screening radius $R_s < 0$, are known in semiconductor physics [14, 15, 16, 17, 18, 19, 20, 21, 22, 23, 24, 25, 26, 27, 28, 29, 30]. Examples include Si MOSFETs and gated GaAs-AlGaAs heterostructures, where one electrode consists of a clean, low density, two-dimensional electron gas (2DEG) [16, 17, 18, 19, 20, 21, 22]. In these devices, the total capacitance can be written as

$$\frac{1}{C} = \frac{1}{C_g} + \frac{d\mu/dn}{Ae^2}, \tag{2.1}$$

where n is the electron area density, μ is the chemical potential of the 2DEG, and e is the elementary charge. In terms of the effective thickness d^*, Eq. (2.1), implies

$$d^* = d + R_s/2, \tag{2.2}$$

where $R_s = (2\varepsilon_0\varepsilon/e^2)(d\mu/dn)$ is the Debye screening radius of the 2DEG. Capacitance larger than the geometric value, or $R_s < 0$, is possible when the thermodynamic density of states $dn/d\mu$ of the 2DEG is negative (or, equivalently, when the compressibility $(n^2 d\mu/dn)^{-1} < 0$).

In the limit of low electron density, such that the average distance $n^{-1/2}$ is much larger than the effective Bohr radius $a_B = 4\pi\varepsilon_0\varepsilon\hbar^2/me^2$ of the electrons, or in other words the dimensionless parameter $\rho_s = (\pi n a_B^2)^{-1/2} \gg 1$, a 2DEG is a classical system whose physics is dominated by the Coulomb interaction between electrons. This interaction leads to a Wigner crystal-like strongly-correlated liquid state with negative chemical potential $\mu \simeq -0.23e^2 n^{1/2}/\varepsilon_0\varepsilon$. The corresponding Debye screening radius $R_s = -0.23n^{-1/2}$ produces a negative correction [14] [1] to d^*:

$$d^* \simeq d - 0.12n^{-1/2}, \quad (n^{1/2}d \gg 1). \tag{2.3}$$

What happens to d^* when $n^{-1/2} \gg d$? This is the main question addressed in this chapter. Thermodynamic stability criteria ensure that the capacitance cannot be

[1] Ref. [14] dealt with the case of a small number of repelling holes in the almost filled Na impurity band of a Si MOSFET. In this case the kinetic energy is frozen and the Coulomb repulsion of holes creates Wigner crystal-like order. For a free electron gas it is known that $d\mu/dn$ becomes negative [31] at $\rho_s = 2.1$, while classical formulas for energy and chemical potential become accurate only at large enough $\rho_s > 10$. In the intermediate range $2.1 < \rho_s < 10$ one can use quantum mechanical expressions for the energy of the 2DEG, [15, 16, 17, 18, 19, 20, 21, 22, 24, 25, 26, 29, 30] leading to qualitatively similar conclusions.

negative [32], so Eq. (2.3) must not apply at such low densities. In Sec. 2.2 of this chapter we find the function $d^*(d,n) = d \cdot f(n^{1/2}d)$, valid over the whole range of nd^2. The dimensionless function $f(x)$ is shown in Fig. 2.3. We show that in the limit $nd^2 \ll 1$ the effective thickness d^* becomes very small:

$$d^* = 2.7d \cdot (nd^2)^{1/2}, \quad (n^{1/2}d \ll 1). \tag{2.4}$$

This dramatic capacitance growth is due to the coupling of each electron in the 2DEG to its image charge in the metal electrode. At low density, compact electron-image dipoles are separated from each other by a distance much larger than their dipole arm. These dipoles interact weakly with each other, providing only a small resistance to capacitor charging.

Until recently, only relatively small corrections to the geometrical capacitor thickness d were observed experimentally [16, 17, 18, 19, 20, 21, 22]. The most recent paper on this subject [13], however, claims a much larger correction $(d - d^*)/d \sim 0.4$ for a $YBa_2Cu_3O_7/LaAlO_3/SrTiO_3$ (YBCO/LAO/STO) capacitor with a 2DEG at the LAO/STO interface separated by $d = 4$ nm of LAO insulator from the metallic YBCO gate. Theoretical estimates show that $a \sim 1$ nm is by far the smallest length scale in the problem, so that as a zero-order approximation one can use a classical description of the 2DEG. This measurement calls for a comparison of our function $d^*(d,n)$ with the experimental data of Ref. [13]. Such a comparison is shown in Fig. 2.1 and looks quite good without the use of adjustable parameters. We return to a more detailed discussion of this comparison in Sec. 2.5.

In Sec. 2.3 we study the case where both sides of the capacitor are made from 2DEGs with equal electron density n. Such a capacitor in principle can be realized in devices with two parallel quantum wells with tunable concentrations of electrons [18], but we do not know of any published results. The capacitance of such devices was addressed theoretically in Ref. [30]. In the limit $nd^2 \gg 1$, the authors of Ref. [30] arrive at a small correction to d which is twice larger than for that of one 2DEG: $d^* = d + R_s$. In the classical limit $\rho_s \gg 1$, this gives $d^* = d - 0.23n^{-1/2}$. The authors of Ref. [30] assume that this equation remains valid even at $nd^2 \ll 1$, which leads them to the prediction that C diverges and becomes negative at a finite value of nd^2. As the authors themselves recognized, however, their assumption ignores correlations between the two 2DEGs. In

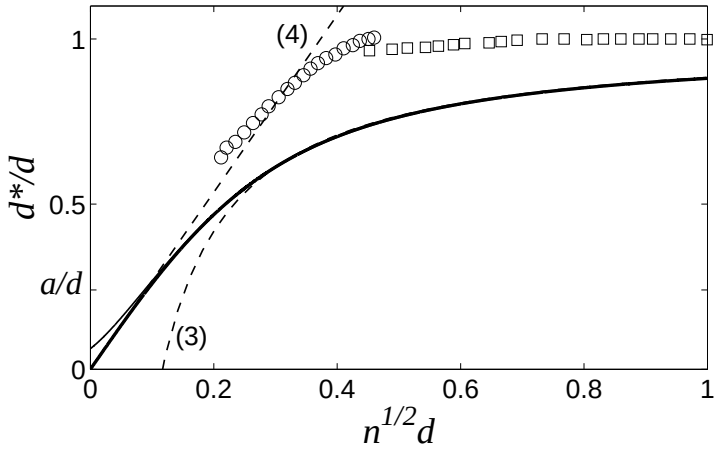

Figure 2.1: The effective thickness d^*/d of a capacitor made from a 2DEG and a metal electrode as a function of the dimensionless parameter $n^{1/2}d$. Open squares and circles correspond to data from Ref. [13] for devices 1 and 2, respectively; in each case the geometric capacitance C_g was assumed to be equal to the largest recorded value of the capacitance. The thick solid curve, which contains no adjustable parameters, is the prediction of this chapter for a classical 2DEG. At relatively large density, there is a small downward correction to d^*, described by Eq. (2.3). At $n^{1/2}d \ll 1$, d^* is described by Eq. (2.4). The thin solid line schematically shows the role of quantum mechanical motion for finite a_B, which at $d^* \approx a_B$ produces a deviation from Eq. (2.4) and leads to a saturation of the capacitance at $d^* = a_B/4$. To draw it we used $a_B = d/4$.

Sec. 2.3 we account for these correlations and demonstrate that they dramatically alter the results of Ref. [30] for d^*. Namely, d^* vanishes and C diverges only in the limit $nd^2 \to 0$, as in the case of a single 2DEG. The transition from large to small nd^2 for two 2DEGs is described by the equation $d^* = d \cdot f(n^{1/2}d/2)$, where $f(x)$ is the same function as for the single 2DEG case. Also similar to the single 2DEG case, the diverging capacitance can be explained by strong correlations between the Wigner crystals of the two 2DEGS, so that an electron transferred from one 2DEG to the other is still bound to its image charge (the hole left behind in the opposite electrode, see Fig. 2.5). Thus, at $nd^2 \ll 1$ only the weak dipole-dipole repulsion between two electron-hole dipoles is responsible for resistance to charging of the 2DEGs capacitor.

Of course, the divergence of the capacitance at $nd^2 \to 0$ takes place only at simultaneously vanishing Bohr radius a, temperature, disorder, and, in the case of two 2DEGs,

probability of tunneling through the insulator. At some strength these factors destroy the Coulomb correlations between electrons at a particular value of nd^2 and truncate the capacitance growth, so that at $nd^2 \to 0$ the capacitance remains finite. Such a behavior is shown schematically by the thin line in Fig. 2.1, which assumes vanishing temperature and disorder but finite $a_B = d/4$. We see that the capacitance can grow as much as 16 times from the geometrical value.

In Sec. 2.4 we confirm the approximate results of Fig. 2.1 with a more careful calculation that fully incorporates the quantum nature of the electrons and is based on the variational principle. We use our results to make an accurate comparison with the experiment of Ref. [13] and to discuss the non-monotonic behavior of the electron correlation function. We also make predictions for the dependence of the capacitance on spin polarization. The variational technique that we develop is broadly applicable for problems of calculating the energy of an electron gas with truncated interactions.

In the theoretical treatment of Secs. 2.2 – 2.4, we neglect the effects of any disorder potential acting on the plane of the 2DEG. In real devices, however, disorder is usually so severe that it closes the window of nd^2 in which d^* is substantially smaller than d. Nonetheless, the experiment of Ref. [13] shows a large correction, so that apparently such a window is open. In Sec. 2.5 we discuss this experiment in greater detail in an attempt to understand why it represents a special case where large capacitance can be observed. We also discuss the effects of the quantum kinetic energy of electrons in the 2DEG, and show that in the absence of disorder it provides an upper limit for the capacitance at $d^* = a_B/4$.

We note that this chapter represents an extension of an approach we have previously used to study large capacitance at the interface between a metal and an ion-conducting glass [33, 34]. The present chapter describes a similar effect for systems where the countercharge consists of a 2DEG separated from the metal by an insulator. Over a certain range of the electron density $a_B^2/d^4 \ll n \ll 1/a_B^2$, the capacitance in such systems is dominated by the strong Coulomb interactions between discrete charges and can therefore be described using a classical analysis similar to that of Refs. [35, 33, 34].

Our general approach to calculating the capacitance in the sections below is as follows. We first describe the total electrostatic energy $U(n)$ associated with the ground state configuration of n electrons per unit area. If the two sides of the capacitor are

coupled through a voltage source with voltage V, then the value of the charge Q of the capacitor is that which minimizes the total energy $U - QV$, where the term $-QV$ represents the work done by the voltage source relative to the situation $V = 0$. Using the (zero-temperature) equilibrium condition $d(U-QV)/dQ = 0$ along with $dQ = eAdn$ gives

$$V = \frac{dU}{dQ} = \frac{1}{eA}\frac{dU}{dn}. \tag{2.5}$$

The differential capacitance (or "charge susceptibility") of the system $C = (dV/dQ)^{-1}$ can therefore be written

$$C = e^2 A^2 \left(\frac{d^2U}{dn^2}\right)^{-1}. \tag{2.6}$$

These equations are equivalent to the thermodynamic relations between capacitance and voltage presented in Sec. 1.1. We can solve for the capacitance as a function of voltage, $C(V)$, by combining Eqs. (2.5) and (2.6). Finally, the effective capacitor thickness d^* is also defined by the total energy U as

$$d^* = \frac{\varepsilon_0 \varepsilon}{e^2 A}\frac{d^2U}{dn^2}. \tag{2.7}$$

In this way a description of the total energy is sufficient to determine the capacitance, and it is not necessary to invoke the Poisson equation or to make mean-field approximations of the electric potential.

2.2 Capacitor with a classical 2DEG and a metal electrode

In this section we describe a 2DEG with area density n separated from a perfect metal electrode by an insulator of thickness d. This can be, for example, a Si MOSFET or a gated GaAs-AlGaAs heterostructure, where a 2DEG is created at the semiconductor-insulator interface and connected to one terminal of a voltage source by ohmic contacts. The metal electrode is connected to the opposite terminal of the voltage source. For simplicity, we assume that the dielectric constant ε is uniform everywhere. We treat the 2DEG in the classical limit $na^2 \ll 1$.

In the ground state for low electron density n, the repulsion between electrons within the 2DEG causes them to form a strongly-correlated liquid, reminiscent of a two-dimensional Wigner crystal, in which electrons are separated from their nearest

neighbors by a distance $\sim n^{-1/2}$. Each electron, of charge $-e$, also induces an image charge, $+e$, in the metal surface, which is effectively located a distance $2d$ from the 2DEG. This situation, which was first envisioned by Widom and Tao [36], is shown schematically in Fig. 2.2. We suppose that the 2DEG is connected to some voltage source which maintains a difference in electric potential V between the 2DEG and the metal electrode. The charge Q of the capacitor is defined as the amount of charge that has moved through the voltage source relative to the state $V = 0$.

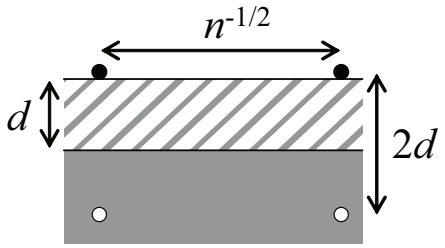

Figure 2.2: Two neighboring electrons (black circles) in a 2DEG formed at the semiconductor-insulator interface. The electrons are separated from a metal electrode (solid area) by an insulator of thickness d (hatched area). The electrons form positive image charges in the metal (white circles).

A given electron within the 2DEG and its image charge effectively form an electron-image dipole, with dipole moment $2ed$, which repels an adjacent electron. In the limit $n^{-1/2} \gg d$, we can use the point-dipole approximation and the repulsive energy between two adjacent electrons is $e^2 d^2 n^{3/2}/2\pi\varepsilon_0\varepsilon$. More generally, we can write the total electrostatic energy of the nS electrons in the 2DEG by first calculating the electrostatic potential ϕ_0 experienced by each electron relative to infinity. Specifically, for an electron located at the origin

$$\phi_0 = \frac{e}{8\pi\varepsilon_0\varepsilon d} - \sum_{\{i,j\}\neq\{0,0\}} \frac{e}{4\pi\varepsilon_0\varepsilon}\left(\frac{1}{r_{i,j}} - \frac{1}{\sqrt{r_{i,j}^2 + (2d)^2}}\right), \tag{2.8}$$

where the indices i, j label the set of electron locations and $r_{i,j}$ is the distance between the electron $\{i, j\}$ and the origin. The term outside the sum in Eq. (2.8) indicates the potential contributed by the electron's own image charge, which is added in place of the self-interaction term $\{i, j\} = \{0, 0\}$. ϕ_0 can be estimated by assuming that the electrons

occupy a regular square lattice with lattice constant $n^{-1/2}$, in which case

$$\phi_0 = \frac{e}{8\pi\varepsilon_0\varepsilon d} - \frac{en^{1/2}}{4\pi\varepsilon_0\varepsilon} \cdot w(n^{1/2}d), \tag{2.9}$$

where $w(x)$ is a dimensionless function

$$w(x) = 4\sum_{i=1}^{\infty}\sum_{j=0}^{\infty}\left(\frac{1}{\sqrt{i^2+j^2}} - \frac{1}{\sqrt{i^2+j^2+4x^2}}\right). \tag{2.10}$$

The sum in Eq. (2.10) is convergent for all x. We note that while the true lowest energy configuration for the electrons is to occupy a triangular lattice, the energy per unit area of a square lattice of dipoles differs from that of a triangular lattice by less than 2% [37], so for computational simplicity we use a square lattice for all calculations.

The total energy of the configuration of electrons is

$$U = -\frac{1}{2}eAn\phi_0 = -\frac{e^2A}{16\pi\varepsilon_0\varepsilon d}n + \frac{e^2A}{8\pi\varepsilon_0\varepsilon}n^{3/2}w(n^{1/2}d). \tag{2.11}$$

Combining Eqs. (2.11) and (2.7) gives

$$\frac{d^*}{d} = \frac{1}{32\pi}\left[\frac{3w(x)}{x} + 5w'(x) + xw''(x)\right] \equiv f(x), \tag{2.12}$$

where $x = n^{1/2}d$.

The dimensionless function $f(x)$ is plotted in Fig. 2.3. At $x \ll 1$, one can expand the summand in Eq. (2.10) to lowest order in x and arrive at the point-dipole approximation for the interaction among electron-image pairs, which after summation gives $w(x) \simeq 18x^2$. The resulting effective capacitor thickness approaches zero linearly with x, and the function $f(x)$ is described by

$$f(x) \simeq 2.7x, \quad (x \ll 1), \tag{2.13}$$

which is equivalent to Eq. (2.4). This vanishing of d^* at $x \to 0$ implies that the capacitance diverges when the electron gas is very sparse. Such diverging capacitance is the result of a vanishing dipole-dipole repulsion between adjacent electron-image pairs as the electron density goes to zero.

At large electron density $x \gg 1$, the effective thickness d^* approaches the geometric thickness d. In other words, C approaches C_g. In the region $x \gg 1$, the difference

between d^* and d can be viewed as a small correction associated with a finite negative screening radius of the 2DEG. In this case $f(x)$ approaches

$$f(x) = 1 - 0.12/x, \quad (x \gg 1), \tag{2.14}$$

which is equivalent to Eq. (2.3). It is only at much larger density $n \gtrsim 1/a^2$, that quantum effects cause the 2DEG screening radius R_s to become positive, so that d^* becomes larger than d.

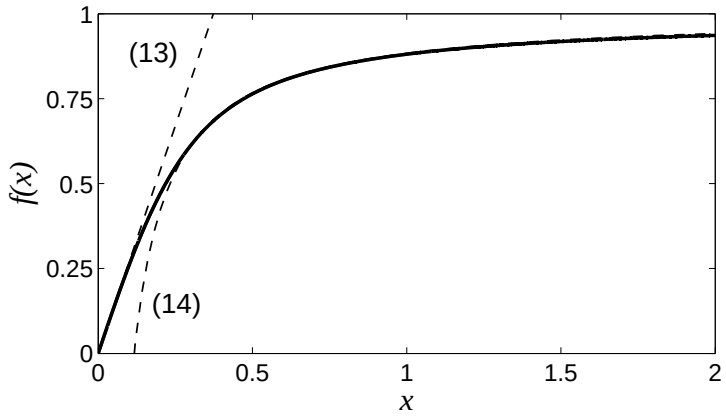

Figure 2.3: The dimensionless function $f(x)$ defined in Eq. (2.12). The function gives the effective thickness d^*/d of a capacitor composed of a 2DEG separated from a metal surface by an insulator of thickness d as a function of the dimensionless electron density $x = n^{1/2}d$. The left side of the plot corresponds to a very sparse 2DEG, where the electrons can be thought to form an array of discrete electron-image dipoles and d^* is described by Eq. (2.13). The right side corresponds to a relatively dense packing of electrons, where the electrons form an almost uniform layer of charge and d^* is described by Eq. (2.14).

We can also derive a relation between the voltage of the capacitor and the electron density n by using Eq. (2.5). If we define V_t to be the "threshold voltage" at which the electron gas is completely depleted ($n = 0$), then the derivative of Eq. (2.11) implies that

$$V - V_t = \frac{e}{4\pi\varepsilon_0\varepsilon d} x \left[3w(x) + xw'(x)\right]. \tag{2.15}$$

Combining the results of Eqs. (2.12) and (2.15) allows us to create a plot of the capacitance as a function of $V - V_t$. The result is shown in Fig. 2.4, with the capacitance

and voltage plotted in the dimensionless forms C/C_g and $V/(e/4\pi\varepsilon_0\varepsilon d)$, respectively. At small voltages $0 < V - V_t \ll e/\varepsilon d$, the capacitance diverges as $C \propto (V - V_t)^{-1/3}$. At large voltages $V - V_t \gg e/\varepsilon d$, the capacitance approaches its geometric value.

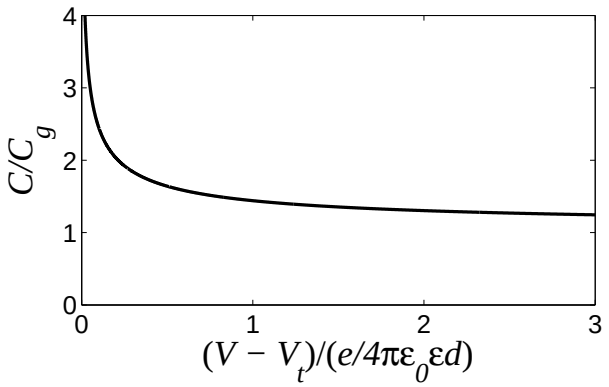

Figure 2.4: The zero-temperature capacitance of a capacitor made from a 2DEG parallel to a perfect metal electrode, plotted as a function of voltage.

2.3 Capacitor made from two 2DEGs

One can also imagine a capacitor where 2DEGs comprise *both* electrodes, as was treated theoretically in Ref. [30]. Such a situation is possible in devices with two parallel quantum wells with tunable concentrations and separate contacts. This can be, for example, a GaAs-AlGaAs-GaAs heterostructure, where 2DEGs are formed at both heterojunctions. The densities of the two 2DEGs can be tuned by applying a large bias voltage V_B above each of them. If a small additional voltage V is applied between the two 2DEGs, then the response to this small voltage can be used to determine the capacitance of the two-2DEG system. This setup is shown schematically in Fig. 2.5(a).

In this section we consider the case of two identical 2DEGs oriented parallel to each other and separated by a distance d. They are connected to opposite terminals of a voltage source maintained at a particular voltage V. We assume that at $V = 0$ both 2DEGs have the same density n of electrons and that charge neutrality is maintained by a uniform plane of surface charge with density $+en$ that coincides with the plane of each 2DEG. We also assume, for simplicity, that the dielectric constant ε is uniform

everywhere.

At zero temperature, the electron positions are strongly correlated, with electrons in a 2DEG seeking to maximize their separation both from each other and from electrons in the opposite plane. As a result, at $V = 0$ electrons form interlocking lattices of electron positions on the two electrodes, as shown schematically in Fig. 2.5(b). The exact configuration of the two lattices can take on one of three arrangements, depending on the value of the parameter nd^2 [38]. However, the energy of these different lattice types differs by only a few percent, so for illustrative purposes we have shown the simplest case of two interlocking square lattices.

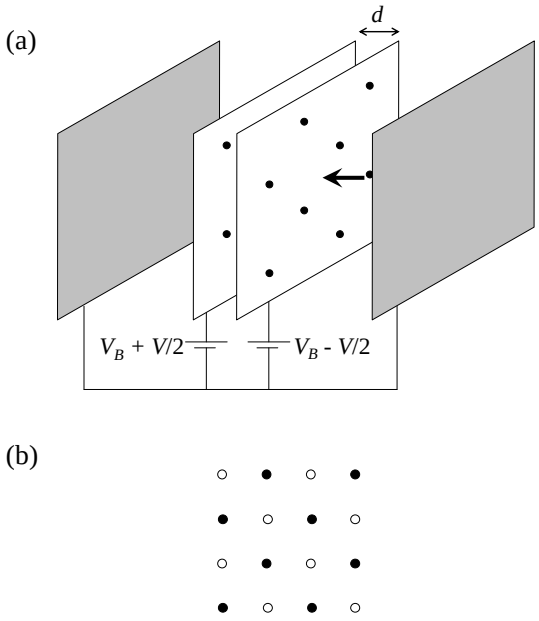

Figure 2.5: (a) A schematic picture of a capacitor made from two parallel, depleted electron gases (black circles on top of white squares). A large bias voltage V_B is applied from either side of the 2DEGs by metallic gates (shaded squares) in order to deplete the 2DEGs to some small density n. An additional small voltage V is applied between the two 2DEGs and determines the capacitance. Insulating layers separating the metallic gates from the 2DEGs and the 2DEGs from each other are not shown. (b) A frontal view of the 2DEGs, as indicated by the thick arrow in (a). On the upper 2DEG, electrons (black circles) form a lattice with lattice constant $\sim n^{-1/2}$. Electrons on the lower 2DEG (white circles) also form a lattice, but this lattice is offset from the other so that electrons in the two 2DEGs minimize their Coulomb interaction energy.

In order to give the two-2DEG capacitor a finite charge Q, some number of electrons must be transferred from one 2DEG to the other. For one electron, this process requires a finite amount of energy Δu, associated with creating a defect in the two lattices. While a careful calculation of Δu is not a major goal of this chapter, we make an estimate of its value at the end of this section.

When the voltage applied between the two 2DEGs is smaller than $\Delta u/e$, no charge transfer is possible and the capacitance $C = 0$. At $V > \Delta u/e$, some finite area density of electrons δn is transferred from one 2DEG to the other and the corresponding capacitor charge is $Q = eS\delta n$. These "excess electrons" also repel each other, and they seek to maximize their distance from each other by forming a Wigner crystal-like lattice of defects in the ground state "checkerboard" of electrons. At low temperature, excess electrons remain coupled to the "holes" they leave behind in the opposite 2DEG and therefore they repel each other by a dipole-dipole repulsion. The form of this repulsion is identical to that of the previous section, where the image charge was formed in the metal electrode, except that in the present case the dipole arm is d rather than $2d$ and there is an overall factor 2 associated with the presence of a repulsive force at both positive and negative sides of the dipole. This similarity allows us to use previous results in writing the total electrostatic energy U of the system relative to the ground state. Namely,

$$U = A\delta n\Delta u + \frac{e^2 A}{4\pi\varepsilon_0\varepsilon}(\delta n)^{3/2} \cdot w\left((\delta n)^{1/2}d/2\right), \tag{2.16}$$

where $w(x)$ is the same function defined in Eq. (2.10).

The density of excess electrons δn can be related to the voltage V by $V = dU/dQ = dU/d(eS\delta n)$. If we define $y = (\delta n)^{1/2}d$, then this relation gives

$$V - \frac{\Delta u}{e} = \frac{e}{8\pi\varepsilon_0\varepsilon d} \cdot \frac{y}{2}\left[3w(y/2) + \frac{y}{2}w'(y/2)\right]. \tag{2.17}$$

As in Eq. (2.7), the corresponding effective thickness is $d^* = \varepsilon_0\varepsilon/e^2A \cdot d^2U/d(\delta n)^2$, which gives

$$\frac{d^*}{d} = f(y/2), \tag{2.18}$$

where $f(x)$, plotted in Fig. 2.3, is the same function as in Eq. (2.12).

Eq. (2.18) is correct when the applied voltage V is low enough in absolute value that neither 2DEG is depleted. At some critical voltage V_c, however, no additional charge

transfer is possible between the two 2DEGs and the capacitance collapses. The value of V_c can be estimated by setting $\delta n = n$, which corresponds to substituting $x = n^{1/2}d$ for y in Eq. (2.17).

We now comment on the threshold energy Δu required to transfer a single electron from one 2DEG to the other at zero voltage. A rough estimate of Δu can be made by imagining that an electron is transferred to the site directly across from it in the opposite 2DEG and that all other electrons remain in their ground state positions. In this case Δu can be evaluated as

$$\Delta u = \frac{e^2 n^{1/2}}{4\pi\varepsilon_0\varepsilon} h(n^{1/2}d), \tag{2.19}$$

where $h(x)$ is a dimensionless function

$$h(x) = 4\sqrt{2}\sum_{i=1}^{\infty}\sum_{j=0}^{\infty}\left[\frac{(-1)^{i+j+1}}{\sqrt{i^2+j^2}} - \frac{(-1)^{i+j+1}}{\sqrt{i^2+j^2+2x^2}}\right]. \tag{2.20}$$

Here, for simplicity, we have again assumed a square lattice of electron positions, as in Fig. 2.5. The function $h(x)$, which is convergent for all x, is plotted in Fig. 2.6. The estimate of Eqs. (2.19) and (2.20) assumes that the lattice of electron positions is undisturbed by the transfer of one electron, which is valid when the 2DEGs are relatively sparse, $x \ll 1$, which is the major focus of this chapter. At larger x the lattice is more easily deformed and Eq. (2.19) represents an upper bound for Δu.

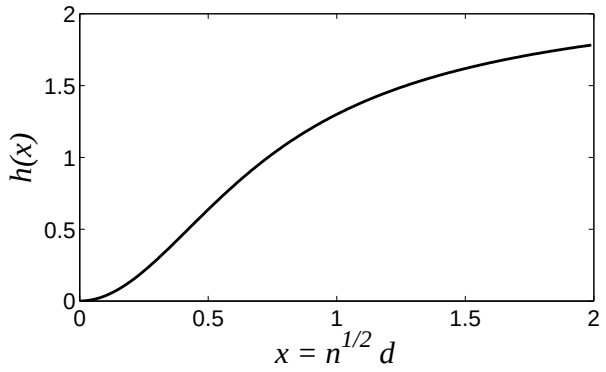

Figure 2.6: The dimensionless function $h(x)$, as defined in Eq. (2.19). This function determines the energy required to move a single electron from one 2DEG to the other at zero temperature.

2.4 Variational calculation

Thus far, we have based all our calculations on a classical approximation, where electrons are treated as motionless point charges. In a particular window of low electron density, $a_B^2/d^4 \ll n \ll 1/a_B^2$, this approximation is valid and provides an accurate calculation of the main term of the capacitance. Outside of this window, however, one must account for the role of quantum fluctuations of the electrons by calculating the energy in a self-consistent way that includes additional contributions to the energy associated with the electrons' quantum kinetic energy. In this section we develop a method for calculating the total energy based on the variational principle and on known results for the correlation function of electrons in a conventional, unscreened 2DEG. We focus on the case of a single 2DEG next to a metal electrode (as in Sec. 2.2) and compare our results to the experiment of Ref. [13]. We also examine the non-monotonic change in the strength of electron correlations with increasing electron density n, and we perform an independent test of the accuracy of our results by comparing with known results for a different system.

2.4.1 The unscreened electron gas as a reference system

The electron gas with $1/r$ Coulomb interactions is a fundamental reference system. It provides both a testing ground for many-body theory and a microscopic input for the density functional theory (DFT), which is the main tool of electron structure calculations [39]. However, there are compelling reasons to study electrons with interactions other than Coulomb. One is a recent interest in mixed DFT schemes, where the Coulomb potential is split into a long-range part, to be handled by other techniques, and a short-range part, to be treated within the usual DFT. This allows one to capture long-range van der Waals interaction effects but necessitates recomputing the exchange-correlation energies for the truncated Coulomb potential [40]. Another and more direct motivation comes from the physics of low-dimensional systems, in which the bare interaction is often modified by the environment. One prominent example is the main problem of this chapter, where a 2DEG is positioned a small distance d away from a metallic gate. The

gate creates an image charge for each electron, leading to the interaction law

$$u(r) = \frac{e^2}{4\pi\varepsilon_0\varepsilon r} - \frac{e^2}{4\pi\varepsilon_0\varepsilon\sqrt{r^2+4d^2}}\,, \tag{2.21}$$

as discussed in Sec. 2.2. At $r \gg d$, this potential rapidly decays: $u(r) \simeq e^2d^2/2\pi\varepsilon_0\varepsilon r^3$. Therefore, electron correlations at low density $n \ll 1/d^2$ are very different from those in the absence of the gate.

Generally speaking, the most reliable results for the electron gas have been obtained by quantum Monte Carlo (MC) simulations. While some non-Coulomb potentials have been examined [41] in applications to ^{3}He and nuclear matter in three dimensions (3D), no simulations for the interaction law $u(r)$ in 2D have been reported. Below we demonstrate a variational method for calculating the total energy E per electron, which is accurate yet simple to implement for any truncated Coulomb potential. Our approach is to treat the electron charge e in e^2/r as an adjustable parameter and use the corresponding ground states as trial states for the system with the desired interaction law $u(r)$. Since the $1/r$ interaction does not have an intrinsic length scale, the variational energies can be obtained from the already existing Monte Carlo data by a suitable rescaling.

Experimentally, the regime $nd^2 < 1$ has been probed in several recent studies [13, 42, 43, 44]. As in previous sections, we focus on that of Ref. [13], which presents the smallest range of nd^2 that has thus far been explored. In Fig. 2.7(a) we present the results for the effective capacitor thickness d^*, which is related to $E(n)$ by

$$d^* = \frac{\varepsilon_0\varepsilon}{e^2}\frac{d\mu}{dn} = \frac{\varepsilon_0\varepsilon}{e^2}\frac{d^2}{dn^2}\big(E(n)n\big)\,, \tag{2.22}$$

where $\mu(n)$ is the electrochemical potential. This relation is equivalent to Eq. (2.7). Our results are in a good agreement with the experiment [13]; however, the gate screening effect becomes important only at the lowest measured densities [see Fig. 2.7(a)]. In the remainder of this section we first describe how these results have been obtained and then show that our method captures the essential physics of the problem at both low and high densities. Next, we check that our solution satisfies the virial theorem and verify the accuracy of our method on a 3D example. Finally, we discuss experimental implications.

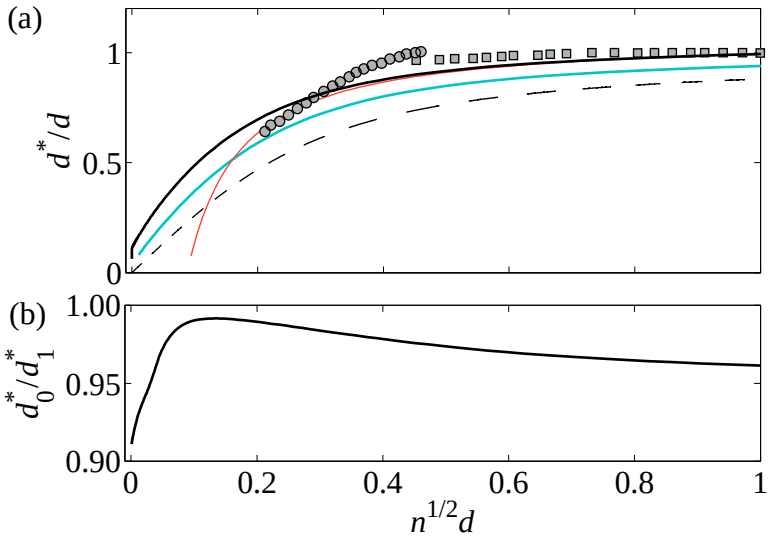

Figure 2.7: (a) The effective capacitor thickness d^* in units of d as a function of $n^{1/2}d$ for the spin unpolarized case, plotted with (thick lines) and without (thin red solid line) the gate screening effect. The upper (black) thick line is for $d/a_B = 4$ and the lower (light blue) thick line shows $d/a_B = 16$. The dashed line is the classical theory of Sec. 2.2. Symbols are the experimental data [13]. (b) The ratio of d^* for the spin unpolarized ($\zeta = 0$) and polarized ($\zeta = 1$) cases.

2.4.2 Variational procedure

The trial states for our variational calculation are the ground-states of the 2D electron gas with the e^2/r interaction on a neutralizing background. The total energy per electron E, the interaction energy $E^{(\mathrm{int})}$, and the pair distribution function (PDF) $g(r)$ of this system are known to scale with n and with the dimensionless parameter $\rho_s = 1/\sqrt{\pi n a_B^2}$. For example,

$$E = E_0 F(\rho_s)\,, \quad E^{(\mathrm{int})} = E_0 F^{(\mathrm{int})}(\rho_s) \quad (\text{no gate})\,. \tag{2.23}$$

Here $E_0 = \pi\hbar^2 n/m$ is the Fermi energy of a noninteracting 2D Fermi gas and $F(\rho_s)$ is a dimensionless function [39]. By the virial theorem, $F^{(\mathrm{int})}(\rho_s) = \rho_s F'(\rho_s)$. Similarly, we can write $g(r) = G(k_F r, \rho_s)$, where G is another dimensionless function and $k_F = \sqrt{2\pi n}$ is the Fermi wave vector. We rely on the fact that F and G have been computed by MC techniques and fitted to analytical expressions [45, 46, 47] over the broad range $1 \le \rho_s \le 40$. This enables us to use e^2, or equivalently, ρ_s, as a variational parameter

that labels the trial wave function. We denote this parameter $\tilde{\rho}_s$ to distinguish it from the physical ρ_s. Large $\tilde{\rho}_s$ describes a strongly-correlated, crystal-like arrangement of electrons [36, 48], while $\tilde{\rho}_s = 0$ corresponds to the free Fermi gas, as in the Hartree-Fock (H-F) approximation. The optimal $\tilde{\rho}_s$ is to be found by minimizing the variational energy $E_{\rm var}(n, \tilde{\rho}_s) = E^{\rm (kin)}_{\rm var}(n, \tilde{\rho}_s) + E^{\rm (int)}_{\rm var}(n, \tilde{\rho}_s)$. We expect $\tilde{\rho}_s < \rho_s$ because screening by the gate reduces electron repulsion and weakens electrostatic correlations.

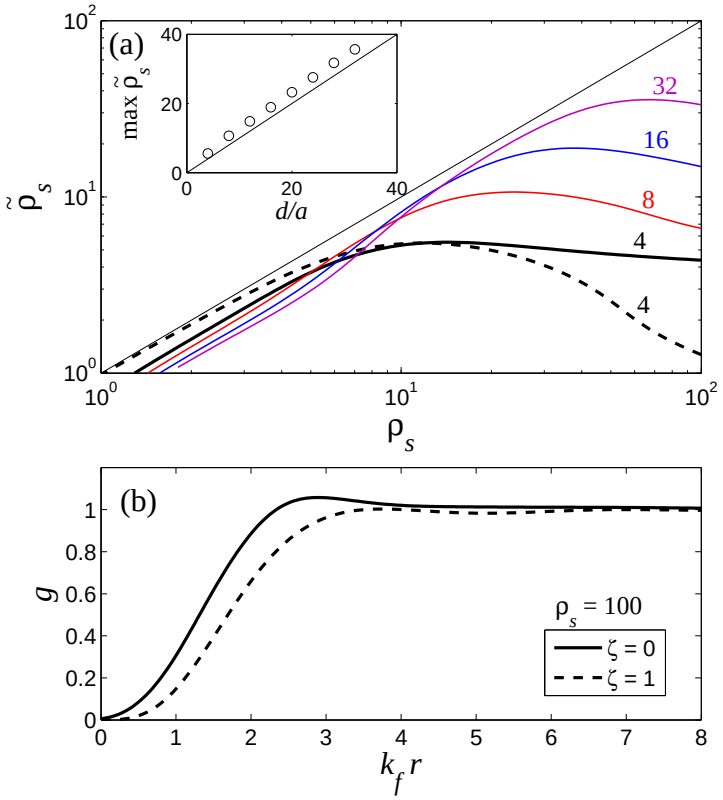

Figure 2.8: (a) Optimal $\tilde{\rho}_s$ *vs.* the physical ρ_s. Solid (dashed) lines correspond to $\zeta = 0$ ($\zeta = 1$). The labels indicate the values of d/a_B. The inset depicts the maximum value of $\tilde{\rho}_s$ for $\zeta = 0$ (circles) as a function of d/a_B (line). (b) Pair distribution functions $g(r)$ for the optimal trial states at $\rho_s = 100$.

For a given trial $\tilde{\rho}_s$, the kinetic energy $E^{\rm (kin)}_{\rm var}(n, \tilde{\rho}_s)$ is obtained by subtracting the interaction energy from the total energy for the $1/r$ interaction:

$$E^{\rm (kin)}_{\rm var}(n, \tilde{\rho}_s) = E_0 \left[F(\tilde{\rho}_s) - \tilde{\rho}_s F'(\tilde{\rho}_s)\right]. \tag{2.24}$$

By making use of the definition $E = E_0(1+\zeta^2)/2 + E_x + E_c$, where E_x is the exchange

energy, $E_c = E_0 F_c(\rho_s)$ is the correlation energy, and $0 \leq \zeta \leq 1$ is the spin polarization, we can rewrite Eq. (2.24) as

$$E_{\rm var}^{\rm (kin)} = E_0 \left(\frac{1+\zeta^2}{2} - \tilde{\rho}_s F_c'(\tilde{\rho}_s) \right). \tag{2.25}$$

The function $F_c(\tilde{\rho}_s)$ is taken from Ref. [46]. The interaction energy $E_{\rm var}^{\rm (int)}$ is computed by numerical quadrature of the potential $u(r)$ weighted by the PDF,

$$E_{\rm var}^{\rm (int)}(n, \tilde{\rho}_s) = \frac{1}{2} \int_0^\infty u\left(\frac{x}{k_F}\right) G(x, \tilde{\rho}_s) x dx - \frac{e^2}{16\pi\varepsilon_0 \varepsilon d}. \tag{2.26}$$

(The last term accounts for the interaction of each electron with its image.) For G, we use the parametrization of Ref. [47]. The minimization of $E_{\rm var}$ over $\tilde{\rho}_s$ is done numerically. Finally, d^* is computed according to Eq. (2.22).

We performed these calculations for d/a_B ranging from 4 to 32 and for two values of the spin polarization, $\zeta = 0$ (unpolarized) and 1 (fully polarized).[2] The optimal $\tilde{\rho}_s$ as a function of the physical ρ_s is shown in Fig. 2.8(a) for $\zeta = 0, 1$. At large electron density (small ρ_s), $\tilde{\rho}_s$ remains close to ρ_s because the average spacing between electrons is much smaller than d, so that the gate plays a minor role. As ρ_s increases, $\tilde{\rho}_s$ attains a maximum value $\tilde{\rho}_s \approx d/a_B$, and then drops off. This is because at $\rho_s > d/a_B$ the interaction between electrons becomes effectively short-ranged, so that electrons lose their electrostatic correlations as the system becomes more dilute. For $\zeta = 1$, the drop of $\tilde{\rho}_s$ at $\rho_s > d/a_B$ is fairly rapid. In contrast, in the unpolarized case, $\tilde{\rho}_s$ exhibits a broad plateau before it also collapses at very high ρ_s [far beyond the range shown in Fig. 2.8(a)].

In the remainder of this section we show that our results withstand several tests: (i) they correctly reproduce the asymptotic behavior at large and small n, (ii) they obey the virial theorem, and (iii) when generalized to 3D, they yield a good agreement with MC simulations [40].

2.4.3 Low and high density asymptotics

Because of its fast $1/r^3$ decay, $u(r)$ belongs to the universality class of short-range potentials. At low n, the energy per particle coincides in the first approximation with

[2] The parameter ζ enters implicitly in the functions f_c and G.

that of the free Fermi gas, except that it is shifted by $-e^2/16\pi\varepsilon_0\varepsilon d$, cf. Eq. (2.26). This is reproduced by our calculation since $\tilde{\rho}_s(n \to 0) = 0$. This fact further implies that $d_0^* \equiv d^*(\zeta = 0)$ and $d_1^* \equiv d^*(\zeta = 1)$ tend to $a_B/4$ and $a_B/2$, respectively, as $n \to 0$ [see Fig. 2.7(a)].

The leading interaction correction to the free gas limit comes from two-body collisions, which are parametrized by the effective hard-core radius [49] $b = 2e^{2\gamma}d^2/a_B$, where $\gamma \approx 0.5772$ is the Euler constant. In the absence of spin polarization ($\zeta = 0$), the perturbative result for the electrochemical potential reads [50] $\mu = E_0[1 + 2v + 4v^2(1 - \ln 2)]$, where [51] $1/v = -2\gamma - \ln(\pi n b^2)$. Accordingly,

$$d_0^* \simeq \frac{a_B}{4}\left[1 + \frac{4}{\ln(a_B^2\,/\,nd^4) - 6.30}\right]. \tag{2.27}$$

This expression is expected to apply at $v \lesssim 1/2$, which corresponds to extraordinary low densities, e.g., $na_B^2 < 10^{-6}$ for $d = 4a_B$. Indeed, our variational method shows that the departure of d_0^* from its zero-density value of $a_B/4$ develops abruptly as a function of n within a narrow interval $n^{1/2}d < 10^{-3}$ [see Fig. 2.7(a)]. Of course, at such n the energy of real electron systems is dominated by disorder [22], which we do not consider here.

The abrupt growth of d_0^* caused by the logarithmic correction in Eq. (2.27) reflects the low-energy behavior of the s-wave scattering phase-shift in 2D. It can be contrasted with the gradual increase of d_1^* for the polarized gas, where p-wave scattering dominates. Here the Pauli exclusion between like-spin electrons ensures that electron pairs do not approach each other too closely and the short-range repulsion is more easily satisfied. As a result, in the polarized gas, we have $d_1^* = (a/2)[1 + \mathcal{O}(nb^2)]$.

We can also consider the opposite limit, $n \gg 1/d^2$, where to the leading order $\tilde{\rho}_s = \rho_s$ and so the kinetic energy is unaffected by the gate. The correction $\Delta E(n, d)$ to the total energy with respect to the reference system without the gate is determined by the interaction energy. To compute the latter, we rewrite Eq. (2.26) as

$$E_{\rm var}^{(\rm int)} = \frac{n}{2}\int u(r)[g(r) - 1]d^2r + \frac{e^2 d}{2\varepsilon_0\varepsilon}\,n - \frac{e^2}{16\pi\varepsilon_0\varepsilon d}\,. \tag{2.28}$$

The difference $g(r)-1$ is appreciable only at $|r| \lesssim n^{-1/2}$ and gives $-1/n$ when integrated over all r. Therefore, to the order $\mathcal{O}(1/d)$ we can set $u(r) = e^2/(4\pi\varepsilon_0\varepsilon r) - e^2/(8\pi\varepsilon_0\varepsilon d)$ in the integral, leading to $\Delta E = (e^2 d/2\varepsilon_0\varepsilon)n$. The corresponding correction to the

electrochemical potential is $\Delta\mu = (e^2 d/\varepsilon_0\varepsilon)n$, which is the classical relation between the voltage μ/e and the charge density en of a parallel-plate capacitor of thickness d.

The parameter d^*, as defined in Eq. (2.22), represents the effective capacitor thickness, with $\mathscr{C} = e^2 dn/d\mu \equiv \varepsilon_0\varepsilon/d^*$ being the capacitance per unit area. In general, d^* differs from the geometric thickness d, which is often called the quantum capacitance (QC) effect (See [30] and references therein). Our preceding calculation shows that at high density the gate can modify the QC only to order $1/nd^2$. A simple expression for this correction can be derived at $n \gg 1/a_B^2$, where the H-F approximation applies. For $\zeta = 0$, we get

$$d^* = d + \frac{a_B}{4} - \frac{1}{(2\pi)^{3/2} n^{1/2}} + \frac{d}{64\sqrt{2\pi^5}(nd^2)^{3/2}}\,. \tag{2.29}$$

The QC is represented by the last three terms in this equation. They account for, respectively, the kinetic energy of the Fermi sea, the exchange energy, and the correction to the exchange due to screening by the gate. Because of the small numerical factor, the last of these becomes important only at $n^{1/2}d \lesssim 0.25$ [see Fig. 2.7(a)].

Finally, the regime of strong correlations induced by the $1/r^3$ tail of the interaction [36, 48] is realized at intermediate densities, $1/b^2 \ll n \ll 1/d^2$. The energy of such a state is largely insensitive to the spin polarization. Indeed, our calculation shows that the relative difference of d_0^* and d_1^* is small at such n. On the other hand, this difference becomes significant in the low-density limit, where the correlations weaken, cf. Fig. 2.7(b). Notice also from Fig. 2.7(a) that for a fixed value of $n^{1/2}d$, the effective thickness d^* approaches the classical result [48] in the limit $d/a_B \to \infty$.

2.4.4 Variational PDF

Our calculation also provides the PDF $g_{\rm var}(r)$ of the screened electron gas [see Fig. 2.8(b)], which has a number of merits. Our PDF is strictly positive, unlike those of some approximate many-body theories [39]. One can show that this $g_{\rm var}(r)$ and the variational energy components satisfy the virial theorem:

$$\frac{D}{n}\,P = 2E^{(\rm kin)} - \frac{n}{2}\int d^D r\, g(r)\, r\frac{du}{dr}\,, \tag{2.30}$$

where $P = [\mu(n) - E(n)]n$ is the pressure and D is the space dimension. (The subscript "var" in P and g is implicit.) The variational estimates of E and μ, which determine

the left-hand side of Eq. (2.30), should be reliable. Therefore, at intermediate values of r, which dominate the value of the integral on the right-hand side, our PDF may be a good approximation. At r much larger or smaller than the mean electron spacing, it is probably less accurate. Thus, we have $g'_{\rm var}(0)/g_{\rm var}(0) = \frac{2}{D-1}\,(\tilde{\rho}_s/\rho_s)$ instead of the exact cusp condition [39] $g'(0)/g(0) = \frac{2}{D-1}$.

2.4.5 Test on a 3D model

The accuracy of our method is best verified by comparison with MC simulations; however, they are not available for our 2D problem. Instead we did such a test for a 3D electron gas with the interaction potential $u(r) = (e^2/4\pi\varepsilon_0\varepsilon r)\,\mathrm{erfc}(\mu_c r)$ [40] (relevant for mixed DFT schemes). The necessary correlation energies and PDF for the standard 3D gas were taken from Refs. [52] and [53]. The results for the cutoff parameter $\mu_c = 0.5/a_B$ are shown in Fig. 2.9. The largest difference between our variational estimate and the MC results [40] for the total energy per particle is $\sim 2\%$, which is a significant improvement over the H-F approximation. This example also illustrates the capability of our method to treat other dimensions and/or interaction laws.[3]

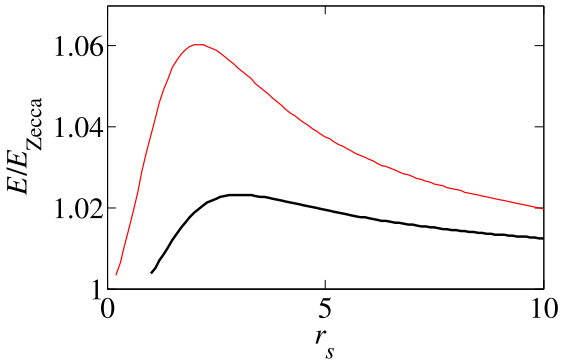

Figure 2.9: The ratio of the total variational energy per particle E and the MC energy $E_{\rm Zecca}$ [40] as a function of ρ_s for a 3D electron gas with the interaction law $u(r) = (e^2/r)\,\mathrm{erfc}(\mu_c r)$ and $\mu_c = 0.5/a$ (thick black line). The thin red line shows the H-F result.

[3] A similar variational method is also successful in 1D, see Ref. [54].

2.4.6 Further applications of our variational method

The variational method we have developed enables us to compute the capacitance of gated nanostructures in which quantum and correlation effects are not mere corrections. Our results agree well with the data of Ref. [13]. Rigorous testing would require additional experiments at still lower densities and/or a strong in-plane magnetic field (to check the predicted spin dependence). Additionally, the energy per particle we compute here is relevant for understanding impurity screening and therefore transport properties of correlated 2D electron liquids near metallic gates [55, 56, 57, 58, 59]. A further, intriguing direction for future work is to devise a variational method suitable for ultrathin gated structures of graphene [42, 43, 44, 60, 61], which is an electron system with a nonparabolic spectrum.

2.5 Discussion

In Sec. 2.4.3 we calculated the low-density limit of the capacitance. Here we discuss it in a somewhat more conceptual way, including in our discussion the effects of disorder in the plane of the 2DEG.

As shown in Sec. 2.4, at zero temperature and in the absence of disorder the capacitance cannot diverge without bound in the limit $nd^2 \to 0$ because of the effects of quantum kinetic energy. This conclusion can be reached by considering that each electron within the 2DEG sits in a potential well created by neighboring electron-image dipoles. If this potential v is expanded to second order in the electron's displacement ρ from the potential well minimum, then we get $v(\rho) = \gamma(e^2d^2n^{5/2}/\varepsilon_0\varepsilon)\rho^2 + e\phi_0$, where $\gamma \approx 4.3$ is a numerical coefficient and $\phi_0 \approx 1.4ed^2n^{3/2}/\varepsilon_0\varepsilon$ is the electrostatic potential described by Eq. (2.9). This potential $v(\rho)$ is that of a two-dimensional harmonic oscillator, and therefore it has a ground state energy $\hbar\omega + e\phi_0$, where ω is defined so that $v(\rho) = m\omega^2\rho^2/2 + e\phi_0$. When $\hbar\omega \ll e\phi_0$, the 2DEG retains its strongly-correlated, Wigner crystal-like structure and the contribution of the quantum kinetic energy to the capacitance is small. At $n^{1/2}d \lesssim 0.2a_B/d$, however, the quantum kinetic energy becomes larger than $e\phi_0$ and the 2DEG loses its electrostatic correlations. This point corresponds to $d^* \approx a_B$. At vanishingly small values of $n^{1/2}d$, the energy of the 2DEG is that of a noninteracting fermion gas, which produces $d^* = a_B/4$. For the experiments

of Ref. [13], $d = 4$ nm and $a_B \approx 1$ nm, so that apparently in this system a capacitance $C \approx 16C_g$ is possible (see Fig. 2.1).

The analysis above has also ignored disorder, which can truncate the divergence of the capacitance by destroying dipole-dipole correlations. The presence of disorder modulates the density of the correlated dipole liquid with some characteristic amplitude δn_d. At small enough average density n, the overall electron density becomes smaller than δn_d. This means that screening becomes nonlinear [23] and multiple pores open in the 2DEG. Electric field lines starting at the metal gate electrode leak through these pores. As a result, the Debye screening radius R_s changes its sign [17, 18, 19, 20, 21, 22, 23, 24, 25, 26, 27, 28] from negative to positive at some $n = n_m$. At smaller n the effective thickness d^* grows sharply. In a 2DEG with moderate mobility and large distance to the gate, $n_m d^2 \gg 1$ and the minimum of d^*/d is very shallow. For example, for the classical 2D hole gas (with large ρ_s) in GaAs/GaAlAs heterojunctions studied in Ref. [22], $n_m d^2 = 5$, while as we see in Fig. 2.3 the crossover between the $nd^2 \gg 1$ and $nd^2 \ll 1$ asymptotic dependencies happens only around $n^{1/2}d \sim 0.25$ or $nd^2 \sim 0.06$.

Larger deviations from the geometrical capacitance can be observed in the cleanest p-GaAs/GaAlAs heterojunction-insulated-gate field-effect transistors (HIGFETs) [62]. In such devices a 2D hole gas is created with concentration as small as $n = 7 \times 10^8$ cm^{-2} by a metallic gate at a distance d from the 2D gas which can be as small as 250 nm. This gives $nd^2 \sim 0.5$, so that if disorder permits $(d - d^*)/d \sim 0.2$ can be reached. There is no published data on capacitance for this case, but there are indications that screening of the Coulomb interaction between 2D holes by the gate (hole images) plays an important role for transport properties [62].

One may be able to reach even larger $(d - d^*)/d$ for the capacitance between two 2DEGs residing in two parallel quantum wells, because in this case d can be as small as 30 nm [17, 18] so that $nd^2 < 1$ already at $n < 10^{11}$ cm^{-2}. We are not aware of any such measurements.

Another system which may provide a good opportunity for studying capacitance larger than C_g is that of a very low density 2DEG which floats on the top of a thin liquid helium film covering a metallic electrode [63, 64].

Let us now return to the most spectacular data, obtained from a YBCO/LAO/STO capacitor [13]. We see from Fig. 2.1 that in this case a much smaller value $nd^2 \sim 0.02$

has been reached than in other cases, resulting in the record for larger-than-geometrical capacitance $(d - d^*)/d = 0.4$. This became possible because of the very small distance between the 2DEG and the gate $d \simeq 4$ nm. Even at relatively large concentration $n = 10^{11}\text{cm}^{-2}$, such small thickness leads to $nd^2 \simeq 0.04$. In Fig. 2.1 the agreement of our classical theory (which has no adjustable parameters) with the experimental data of Ref. [13] looks so good that disorder apparently plays a minor role. The relatively large concentration of electrons may result in a significant resistance to disorder, but the relative unimportance of disorder is nonetheless difficult to understand. No independent estimates of disorder effects in YBCO/LAO/STO capacitor are currently available in literature.

Our comparison with the data of Ref. [13] assumes that the 2DEG is localized within a very narrow layer of STO, on the order of one lattice constant, as was shown in Refs. [65, 66]. There are arguments that the electron layer is actually much wider [67, 68], but these are based on calculations of the nonlinear screening radius of STO using its huge low-temperature dielectric constant $\varepsilon \sim 20,000$. We disagree with using the dielectric constant of STO as measured in uniform crystals when describing nonlinear screening. Indeed, the large dielectric constant of STO (as well as that of displacement ferroelectric crystals) has a strong spatial dispersion. Below we discuss the origin of this dispersion following Ref. [69].

The large, low-temperature, zero-frequency dielectric constant of STO is related to the anomalously small frequency of the transverse optical mode $\omega(q)$ at $q = 0$. At $q = 0$, the dielectric constant $\varepsilon(0) \propto \omega^{-2}(0)$. For finite q, the dielectric constant $\varepsilon(q) \propto \omega^{-2}(q)$. The soft mode is known to have very strong dispersion, so that at large q it returns to the normal optical mode frequency. This dispersion has the form $\varepsilon(q) = \varepsilon(0)/[1 + (q\xi)^2]$, where $\xi = a_0\varepsilon^{1/2}(0)$ and a_0 is the lattice constant [69]. Using such a strongly dispersive dielectric constant for the description of nonlinear screening by electrons in STO self-consistently leads to the conclusion that the nonlinear screening radius, or in other words the width of the 2DEG, is of the order of the lattice constant a_0. (This same dispersion also explains why the large dielectric constant of STO does not lead to strong electron-phonon coupling and a large increase of the critical temperature of superconductivity [70].)

2.6 Conclusion

In this chapter we have shown that in devices where a 2DEG comprises one or both electrodes of a plane capacitor the correlations between electronic charge in opposite electrodes dramatically affect the capacitance at low electron density n. In the absence of disorder, this leads to a capacitance that grows strongly with decreasing nd^2, with a maximum value corresponding to $d^* = a_B/4$ at $nd^2 \to 0$. We have presented a prediction for the effective capacitor thickness d^* which is valid over the entire range of nd^2 and which is based on the Coulomb correlations between electrons and their image charges. The cases of a 2DEG parallel to a metal electrode and of two parallel 2DEGs were considered separately. Our results compare favorably to the recent experiments of Ref. [13], which operate at $nd^2 \ll 1$ and report C larger than C_g by as much as 40%, without the use of adjustable parameters.

The experiments of Ref. [13], which use a 2DEG created at the an LAO/STO interface, are consistent with the 2DEG occupying a very thin layer of STO on the order of one lattice constant, so that the 2DEG can indeed be treated as a two-dimensional system up to fairly high electron density. Further studies on such systems with low disorder and small LAO thickness may provide even better insight into the behavior of the capacitance at small nd^2. Systems of very clean HIGFETs, parallel quantum wells, and electrons floating on liquid helium may also provide good opportunities for studying larger-than-geometrical capacitance.

Chapter 3

Capacitance of an ionic liquid described by the restricted primitive model

3.1 Introduction

Room temperature ionic liquids (RTILs) are molten salts made from ions that are large enough that their Coulomb interaction is relatively small, so that they remain in a fluid state at relatively low temperatures. Essentially, a RTIL is a solvent-free electrolyte, which means that RTILs can be ideally suited for applications which require a thin or intensely concentrated layer of ionic charge. RTILs are already being used for batteries and supercapacitors [71], as well as for gating of new electronic materials. It has therefore become a subject of great interest to understand the nature of the interface between a RTIL and a metallic electrode.

In its simplest form, the question of how a RTIL behaves in the vicinity of a charged metal surface seems remarkably straightforward. While real-life experiments probing the structure of the ionic double-layer can be marked by a number of complications [72], the essential description is encapsulated in a very simple model: an infinite, planar, metallic electrode is placed in contact with a semi-infinite volume that contains a total concentration N of mobile positively- and negatively-charged hard spheres, each with

the same diameter a and the same absolute value of charge e. Such a model of the RTIL is called the "restricted primitive model" (RPM); one can think that it reflects the properties of a real RTIL reasonably well because typical ion sizes in a RTIL, $a \sim 1$ nm, are much larger than atomic sizes. We set the dielectric constant of the RTIL equal to unity, since we are considering a model of non-polarizable ions in a solvent-free environment. If a voltage V is applied between the electrode and the bulk of the RTIL, how large is the charge density σ of the metal surface? In other words, what is the capacitance per unit area $\mathscr{C}(V) = d\sigma/dV$ of the interface?

The answer to this question is well-known in the limit of large temperature and low applied voltage. In this case the ionic double-layer is well-described as a diffuse screening layer with a characteristic size equal to the Debye-Hückel (DH) screening radius

$$r_{DH} = \sqrt{\frac{\varepsilon_0 k_B T}{e^2 N}}. \tag{3.1}$$

The diffuse layer of counter-charge effectively comprises the second half of a parallel-plate capacitor of thickness r_{DH}, so that the capacitance per unit area is equal to $\mathscr{C}_{DH} = \varepsilon_0/r_{DH}$. At large density $Na^3 \sim 1$ this result for capacitance is valid as long as the temperature is high enough that $T \gg T_0 \equiv e^2/4\pi\varepsilon_0 k_B a$ and the voltage is small enough that $eV \ll k_B T$.

More generally, one can characterize the capacitance by the effective thickness of the double-layer $d^* = \varepsilon_0/\mathscr{C}$. In the DH limit, $d^* = r_{DH}$. In realistic situations, however, the characteristic temperature T_0 is very large and the DH approximation fails at room temperature. One can think that as a result ions become more strongly bound to the charged electrode and the size of the double-layer shrinks, so that d^* decreases and the capacitance grows. One may ask, then, how thin the double-layer can be, or in other words, how large the capacitance can be. The apparent answer to this question goes back to Helmholtz [9, 10], who imagined that in an extreme case a neutralizing layer of ions could collapse completely onto the electrode surface, thereby forming the second half of a plane capacitor at a distance equal to the ion radius $a/2$. The result is a double-layer of size $d^* = a/2$ and a capacitance per unit area equal to the "Helmholtz capacitance"

$$\mathscr{C}_H = 2\varepsilon_0/a, \tag{3.2}$$

as introduced in Sec. 1.1. In classical mean-field theories of the electrostatic double-layer [73, 74, 75], and in the recent influential theory of the metal/RTIL capacitance which accounts for the excluded volume among ions [12], $\mathscr{C}_H$ plays the role of a maximum possible capacitance per unit area. Monte Carlo simulations [76, 77, 78] seem to confirm this statement. However, these and the majority of other simulations make the simplification of replacing the metal electrode by a uniformly-charged, insulating plane. We argue below that in this way the essential physics of image charges in the metal surface is lost (see also Refs. [79, 80, 81]).

It is the purpose of this chapter to demonstrate that capacitance $\mathscr{C} > \mathscr{C}_H$ is possible, or in other words, that the effective thickness of the double-layer can be smaller than the ion radius. Our previous work [34] has demonstrated that capacitance $\mathscr{C} > \mathscr{C}_H$ can occur for highly asymmetric RTILs (where the cation has a much smaller radius than the anion, or vice-versa). Here we show that even in the RPM, where cations and anions have equal diameter, capacitance significantly larger than the Helmholtz value is possible. As we describe below, the metallic nature of the electrode — specifically, the ability of ions to form image charges in the metal surface — plays a key role in the development of large capacitance. We present the results of Monte Carlo (MC) simulations of the restricted primitive model of a RTIL at various temperatures and densities, and we suggest a basic theoretical explanation of these results based on the weak repulsion between dipoles composed of bound ions and their images in the metal surface.

We note that the critical role of image charges for the structure of the double-layer has in fact been recognized by previous authors [82], who performed similar simulations which account explicitly for the electronic polarization of the electrode. However, Ref. [82] explored only very low ion density $Na^3 = 0.01$, where $\mathscr{C}(V = 0) < \mathscr{C}_H$. Another paper [83] studied the capacitance of a RTIL between two identical metal plates and obtained large capacitance $\mathscr{C}(0) \sim 2\mathscr{C}_H$, but this study used a much more complicated model of the RTIL.

The remainder of this chapter is organized as follows. In Sec. 3.2 we present our MC results for $\mathscr{C}(T)$ at small voltage and describe our MC procedure. Sec. 3.3 is devoted to our analytic theory, including both temperature and voltage dependence of the capacitance $\mathscr{C}(V, T)$. Sec. 3.4 considers the role of the electrode material on $\mathscr{C}(V, T)$.

We conclude in Sec. 2.6 with a summary of our main results.

3.2 Temperature dependence of the capacitance and Monte Carlo simulation method

Fig. 3.1 shows the zero voltage capacitance $\mathscr{C}(0)/\mathscr{C}_H$, as measured by our MC simulations, as a function of reduced temperature $T^* = T/T_0$ for three different dimensionless ion densities Na^3. The points correspond to results from the MC simulation and solid lines are a fit to the form $\mathscr{C}/\mathscr{C}_H = K \cdot (T^*)^{-1/3}$, where K is a numerical constant. The motivation for this $(T^*)^{-1/3}$ dependence is explained in Sec. 3.3. For all three values of the density that we examined, the capacitance at low temperature is significantly higher than the Helmholtz value.

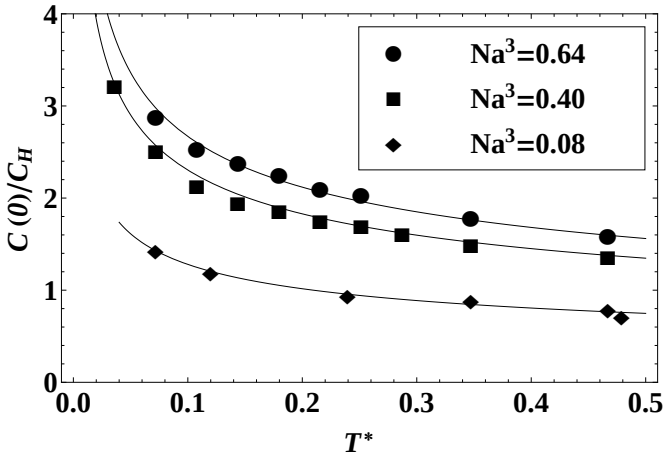

Figure 3.1: The capacitance of the metal/RTIL double-layer at zero voltage as a function of the dimensionless temperature T^*, plotted for three values of the dimensionless ion density Na^3. Symbols represent results from the MC simulation and solid lines show a best fit to the form $\mathscr{C}/\mathscr{C}_H = K \cdot (T^*)^{-1/3}$ for each density. Error bars are smaller than the symbol size.

These results should be contrasted with previous simulation studies [76, 77] of the capacitance of the RPM, in which the metallic electrode was replaced by a charged insulator with uniform charge density σ. These studies report a capacitance $\mathscr{C}(V = 0, T)$ that grows with decreasing T^* before reaching a peak at $T^* = T^*_p$ and then collapsing

rapidly at $T^* < T_p^*$. For $Na^3 = 0.08$ and 0.64, $T_p^* \approx 0.17$ and 0.28, respectively.

The collapse of the capacitance at low temperatures $T^* < T_p^*$ was interpreted by the authors of Refs. [76, 77] as the result of strong binding of positive and negative ions to form neutral pairs. Such binding leads to an extreme sparsity of free charges in the RTIL, so that their total concentration $N_f \ll N$. Substituting N_f for N into Eq. (3.1) at $T^* \ll 1$, we arrive at a large screening radius r_{DH} and therefore much smaller capacitance $\mathscr{C}(0)$. These arguments are generic and convincing. Why, then, does the capacitance in Fig. 3.1 continue to grow with decreasing temperature?

This question is the main focus of our discussion in Sec. 3.3. The remainder of the present section is devoted to describing our Monte Carlo procedure and may safely be skipped by those not interested in the details of our simulation method.

In our MC simulations, a canonical ensemble of M_a anions and M_c cations is placed in a square prism cell of dimensions $L \times L \times L/2$ and corresponding volume $\Omega = L^3/2$. The metallic electrode coincides with one of the cell's square faces. Every charge within the cell forms an electrostatic image in the electrode surface ($z = 0$), *i.e.* a charge $q = \pm e$ at position (x, y, z) has an image charge $-q$ located at $(x, y, -z)$. The total electrostatic energy $\mathcal{E}$ of the cell is calculated as 1/2 times the energy of a system twice as large composed of the real charges and their images, so that

$$\mathcal{E} = \frac{1}{2} \sum_{\{i,j\}}^{M_t} u(d_{i,j}), \tag{3.3}$$

where the indices i, j label the set of all particles in the system (ions and images), $M_t = 2(M_a + M_c)$ is the total number of these particles, $d_{i,j}$ is the distance between particles i and j, and the two-particle interaction energy $u(d_{i,j})$ is

$$u(d_{i,j}) = \begin{cases} \infty, & d_{i,j} < a \\ q_i q_j / 4\pi\varepsilon_0 d_{ij}, & d_{i,j} > a \end{cases}. \tag{3.4}$$

Here, $q_i = \pm e$ is the charge of particle i.

The charge of the electrode is varied by changing the number of anions M_a and cations M_c in the system by equal and opposite amounts, so that the total number of ions $M_a + M_c = N\Omega$ remains fixed for a given overall density N. The corresponding electronic charge (in the form of image charges) in the electrode is $Q = e(M_a - M_c)$

and the capacitance dQ/dV can be determined from the resulting voltage. We use the system size $L = 20a$ everywhere.

At the beginning of each simulation, positive and negative ions are placed within the simulation cell in such a way that they do not overlap with each other or with the metal surface. The MC program then selects an ion at random and attempts to reposition it to a random position within a cubic volume of $(2a)^3$ centered on the ion's current position. The change in the energy $\mathcal{E}$ associated with this move is then calculated, and the move is accepted or rejected based on the standard Metropolis algorithm. For one in every 100 attempted moves, the MC program chooses the random position from within a larger volume $(10a)^3$ as a means of overcoming the effects of any large, local energy barriers. The simulation cell is given periodic boundaries, so that an ion exiting one face of the cell re-enters at the opposite face. To ensure thermalization, 2,500 moves per ion are attempted before any simulation data is collected. After thermalization, simulations attempt 2×10^4 moves per ion, of which 15% – 50% are accepted.

The voltage of the electrode is measured by defining a "measurement volume" near the back of the simulation cell — occupying the range $-L/4 < x < L/4$, $-L/4 < y < L/4$, $L/4 < z < 3L/8$, where the origin $(x, y, z) = (0, 0, 0)$ is located at the center of the electrode surface — inside of which the electric potential is measured. After performing thermalization, the total electric potential is measured at 500 equally-spaced points within the measurement volume after every $3(M_a + M_c)$ attempted moves. These measured values of potential are then averaged both temporally and spatially to produce a value for the voltage V of the electrode relative to the bulk. There was no noticeable systematic variation in electric potential across the measurement volume. The capacitance $C(V = 0)$ is determined from the discrete derivative $\Delta Q/\Delta V$ at sufficiently small values of Q that the relationship Q vs. V is linear. This result is divided by L^2 to produce the capacitance per unit area $\mathscr{C}$.

Our results are shown in Fig. 3.1. For all Na^3 studied, the lowest value of T^* in Fig. 3.1 is larger than the corresponding liquid-gas or liquid-solid coexistence temperature. For comparison, the triple point in the phase diagram of the RPM ionic liquid is located at $Na^3 = 0.5$ and $T^* = 0.025$ while the gas-liquid critical point is at $Na^3 = 0.02$ and $T^* = 0.05$ [84]. We verified for each simulation that there was no phase separation within the simulation cell.

In order to quantify the finite-size effects of our simulation cell, we examined the capacitance at zero voltage, $\mathscr{C}(0, T^*)$, obtained from three simulation volumes of size $L = 10a$, $20a$, and $30a$. For $Na^3 = 0.4$, $\mathscr{C}(0, T^*)$ was seen to scale linearly with $1/L$ at all values of the temperature that we examined ($T^* = 0.042$, 0.072, and 0.14). In each case, the value of $\mathscr{C}(0, T^*)$ obtained by extrapolation to infinite system size was within 20% of the value of $\mathscr{C}(0, T^*)$ corresponding to $L = 20a$. These results allow us to conclude that the simulation cell with $L = 20a$ provides a reasonable approximation of an infinite system. All MC results presented below correspond to this choice.

3.3 An interpretation of the capacitance growth at small voltage and temperature

Our goal is to interpret the large capacitance of the metal/RTIL interface at $T^* \ll 1$. In this section we suggest an analytical, semi-quantitative theory of a mechanism which produces such large capacitance that is reminiscent of our classical theory in Ch. 2. This theory operates in the limited range of temperature $0.05 < T^* < 1$, where the RTIL does not freeze. Thus, our theory (as any theory of the liquid state) does not have any true asymptotically small parameters and should be considered only semi-quantitative.

We begin by observing that when the electrode is metallic, the energy of an ion binding to its image charge, $-e^2/8\pi\varepsilon_0 a$, is exactly half the energy of a bound ion pair, $-e^2/4\pi\varepsilon_0 a$. This fact implies that if an ion pair is separated in the bulk and then both ions are brought to the metal surface there is no net change in electrostatic energy. Thus, even in the absence of applied voltage there are plenty of free charges at the metallic surface. Roughly speaking, this allows the double-layer to be very thin and leads to the large capacitance shown in Fig. 3.1.

The zero-energy process of ion pairs dissociating and sticking to their images on the metal surface implies that at low temperatures $T^* \ll 1$ effectively all ions in the system are either paired in the bulk or bound to their images on the electrode.[1] At zero

[1] This statement is correct even in a relatively dense liquid, where a significant fraction of ion pairs in the bulk form larger neutral clusters, and ions sticking to the metal may be decorated by one or more neutral pairs. Let us imagine a bulk cluster made of $2m$ ions, where m is an odd number — for example, $m = 3$. If the cluster is sufficiently symmetric, then it can be dissociated into two smaller clusters, one positive and one negative, which have an equal number m of ions and which differ only by the inversion of the charge of each ion. When these two charged clusters stick to their images in the metal surface

applied voltage, equal numbers of positive and negative ions are bound to the metal surface. The area density n_0 of these ions can be estimated from the requirement that the chemical potential of pairs in the bulk be equal to the chemical potential of ions at the surface, which gives $\ln(2/Na^3) \simeq 2\ln(1/n_0a^2)$, so that $n_0 \simeq \sqrt{N/2a}$.

As the voltage V of the electrode is increased from zero, some number of pairs in the system are separated so that the free counterion can come to neutralize the electrode surface. The corresponding density of these "excess ions" δn on the metal surface is related to the charge density σ by $\delta n = |\sigma|/e$. If $\sigma > 0$, then δn represents an excess of anions on the surface; if $\sigma < 0$ the excess ions are cations. Naturally, excess ions condensed onto the metal surface repel each other. Since each ion on the metal surface is separated by a distance a from its image charge in the metal, ions and their images constitute compact ion-image dipoles with dipole moment ea, and so excess ions repel each other via a dipole-dipole interaction

$$u_{dd}(\delta n) = \frac{e^2a^2(\delta n)^{3/2}}{8\pi\varepsilon_0}. \tag{3.5}$$

Excess ions at the metal surface are surrounded by n_0 other ions per unit area, which effectively neutralize each other by forming $n_0/2$ bound pairs. These $n_0/2$ bound pairs, along with bound pairs in the bulk, may serve to modify the effective dielectric constant for the interaction of excess ions. We comment on this possibility at the end of the present section.

At low temperatures, the excess ions will seek to maximize their distance from each other while maintaining a given density δn. One can hypothesize a zero-temperature description of the resulting positional correlations, where excess ions form a strongly-correlated liquid reminiscent of a two-dimensional Wigner crystal. The corresponding total electrostatic energy per unit area of the system is

$$\mathscr{U} = \eta \cdot \delta n \cdot u_{dd}(\delta n), \tag{3.6}$$

where η is a numerical coefficient which describes the structure of the lattice of excess

they also recover the energy spent on their dissociation. Thus we are dealing with a statistical physics problem of very high degeneracy, which may have a beautiful exact solution. (Less symmetric clusters may have a small contribution to the partition function of the system.) In this chapter we use the term "excess ions" to refer to all charged objects at the surface, regardless of whether they are decorated by neutral pairs.

ions; for a triangular lattice, $\eta \approx 4.4$ [37]. The quantity $\mathscr{U} - e\delta n V$ is the total energy of the capacitor and voltage source together; $-e\delta n V$ is the source work per unit area.

The voltage V which corresponds to a given charge density $\sigma = e\delta n$ can be found by the equilibrium condition $d(\mathscr{U} - e\delta n V)/d(e\delta n) = 0$, which gives

$$V = \frac{5\eta e a^2}{16\pi\varepsilon_0}(\delta n)^{3/2}. \tag{3.7}$$

The resulting capacitance per unit area $\mathscr{C} = d\sigma/dV = e[dV/d(\delta n)]^{-1}$ is

$$\mathscr{C}(\delta n) = \frac{32\pi\varepsilon_0}{15\eta a\sqrt{\delta n a^2}}. \tag{3.8}$$

Substituting Eq. (3.7) into Eq. (3.8) gives the capacitance in terms of voltage:

$$\mathscr{C}(V) = \frac{32\pi}{3}\left(\frac{1}{10\eta}\right)^{2/3}\left(\frac{e}{4\pi\varepsilon_0 a V}\right)^{1/3}\frac{\varepsilon_0}{a} \approx 1.3\left(\frac{e}{4\pi\varepsilon_0 a V}\right)^{1/3}\mathscr{C}_H. \tag{3.9}$$

The expression of Eq. (3.9) implies that $\mathscr{C}$ can be significantly larger than $\mathscr{C}_H$ when V is small. At such small voltages, the fractional coverage of excess ions on the electrode surface $\delta n a^2 \ll 1$, so that it is incorrect to think of the double-layer in the mean-field way: as a series of uniform layers of charge. Rather, the neutralizing ionic charge consists of discrete ion-image dipoles. The correlated nature[2] of these dipoles allows for lower energy than what is possible in mean-field descriptions, and therefore larger capacitance that is not limited by the physical distance $a/2$ between the electrode and its countercharge.

Of course, the validity of Eqs. (3.5) – (3.9) is limited to the range of voltage where $\delta n a^2 \ll 1$. By Eq. (3.7), this corresponds to a dimensionless voltage $V^* = V/(e/4\pi\varepsilon_0 a) \ll 5\eta/4 \approx 5.5$. At large enough voltages that $\delta n a^2 \simeq 1$, excess ions constitute a uniform layer of charge, and therefore the capacitance approaches $\mathscr{C}_H$. At even larger voltages, the capacitance declines as complete layers of counterions accumulate next to the electrode and the double-layer becomes thicker. This leads to a mean-field capacitance $\mathscr{C} \propto V^{-1/2}$ at large voltages, as described in Ref. [12].

Formally, Eq. (3.9) diverges as the voltage goes to zero. Of course, this expression neglects entropic effects of the excess ions, which tend to destroy the lattice structure of

[2] In principle, the correlations among excess ions on the metal surface can be identified from MC data. This process is made difficult, however, by the large number of neutral pairs and larger neutral clusters present on the metal surface at small voltages. A more exhaustive MC investigation of the surface correlations will be the subject of future work.

excess ions on the metal surface. Such effects will truncate the low-voltage divergence of Eq. (3.9), resulting in a finite capacitance at zero voltage. Intuitively, one would expect that the value of this capacitance maximum can be estimated by evaluating the capacitance at the point where $u_{dd}(\delta n) = k_B T$. This procedure gives

$$\mathscr{C}_{max}(T) = \frac{K}{(T^*)^{1/3}} \mathscr{C}_H, \tag{3.10}$$

where $K \approx 0.6$. In other words, the effective thickness $d^* = a(T^*)^{1/3}/2K$. At $T^* \ll 1$, we find that $d^* \ll a$. The corresponding voltage at which the capacitance plateaus (u_{dd} becomes equal to $k_B T$) is $V_c^* \approx 11 T^*$.

Fig. 3.2 shows the capacitance as a function of V^*, as measured by our MC simulation, at density $Na^3 = 0.4$ and at two values of the temperature T^*. The inset shows the dimensionless charge density $\sigma^* = \sigma a^2/e$ of the electrode as a function of the voltage V^* for the temperature $T^* = 0.042$. The capacitance is determined by a numerical derivative of the σ vs. V curve. Here, e/a^2 is the maximal density for a square lattice of ions on the metal surface, so that σ^* can be interpreted as a filling factor of the first layer of ions. Note that the capacitance drops substantially even at low filling factor σ^*, so that the capacitance is already reduced by a factor two at $\sigma^* = 0.5$. This suggests that for $V^* \lesssim 2$ the decline in capacitance is not driven by the excluded volume effects emphasized in the theory of Ref. [12].

The conclusion $\mathscr{C}_{max}(T) \propto (T^*)^{-1/3}$ can also be reached by an analytical description of the metal surface which is appropriate for small charge density σ, where the excess ions can no longer be described as a strongly-correlated liquid. When the density of excess ions is small enough that $\delta n a^2 \ll (T^*)^{2/3}$, the total free energy $\mathscr{F}$ per unit area can instead be written using a virial expansion:

$$\mathscr{F} \simeq \mathscr{F}_{id} + (\delta n)^2 k_B T B(T) - e\delta n V. \tag{3.11}$$

Here, $\mathscr{F}_{id} = \delta n k_B T \ln(\delta n a^2)$ is the free energy of a two-dimensional ideal gas, $B(T)$ is the second virial coefficient, and $-e\delta n V$ is the source work term. $B(T)$ is calculated from the dipole-dipole interaction energy $u_{dd}(r)$ between two ion-image dipoles as

$$B(T) = \frac{1}{2} \int_0^\infty \left(1 - e^{-u_{dd}(r)/k_B T}\right) 2\pi r dr, \tag{3.12}$$

$$\approx 2.65 \left(\frac{e^2 a^2}{4\pi\varepsilon_0 k_B T}\right)^{2/3}. \tag{3.13}$$

As before, we can use the equilibrium condition $\partial F/\partial(e\delta n) = 0$ to define the voltage with respect to the density of excess ions δn, which gives

$$V^* \simeq T^* \left[5.3\delta n a^2 (T^*)^{-2/3} - \ln\left(1/\delta n a^2\right) \right]. \tag{3.14}$$

In the limit $V^* \to 0$, the two terms on the right hand side of Eq. (3.14) become equal, and the corresponding capacitance $d(e\delta n)/dV$ is $C_{max}(T) \simeq K \cdot C_H/(T^*)^{1/3}$. Hence, this approach arrives at the same conclusion as that of Eq. (3.10), although it gives a somewhat different estimate for the constant $K \approx 1.2$.

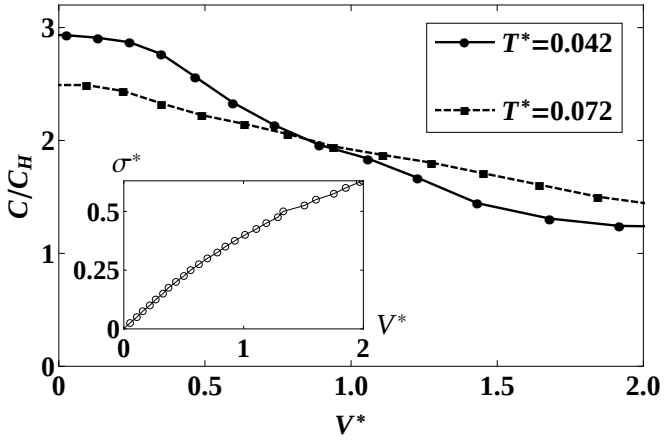

Figure 3.2: The capacitance as a function of the dimensionless voltage $V^* = V/(e/4\pi\varepsilon_0 a)$ at two different temperatures for a system with ion density $Na^3 = 0.4$. The inset shows a plot of the dimensionless charge density $\sigma^* = \sigma a^2/e$ as a function of the voltage V^* measured by the MC simulation at the temperature $T^* = 0.042$.

The prediction of Eq. (3.10) provides a good fit to the capacitance measured by our MC simulation over a range of ion densities, as shown in Fig. 3.1. The value of the coefficient K is found to be 0.6, 1.1, and 1.2 for $Na^3 = 0.08$, 0.4, and 0.64, respectively, which is consistent with our earlier estimates. The dependence of the constant K on the ion density, which produces larger capacitance at larger Na^3, is perhaps an indication that the dipole interaction suggested in Eq. (3.5) is weaker at higher ion density. One possible explanation is that at high densities ion pairs in the vicinity of two excess ions can polarize in the direction of the electric field, thereby producing an effective dielectric constant between them. If such a dielectric constant ε' is added to Eq. (3.5), then we

find that $K \approx 0.6(\varepsilon')^{2/3}$. The values of the constant K from above suggest that for bulk densities $Na^3 = 0.08, 0.4$, and 0.64, the value of ε' is $1.0, 2.4$, and 2.9, respectively. These values are consistent with our interpretation that the effective dielectric constant should increase with ion density, driving the capacitance upward. This increase is also reflected in Fig. 3.2, where the capacitance at finite voltage is somewhat larger than predicted by Eq. (3.9), consistent with the increase in the constant K.

Based on our arguments from this section about the dependence of the capacitance on voltage and temperature, we can hypothesize a general scaling relationship $\mathscr{C}(V^*, T^*)$ which reproduces Eqs. (3.9) and (3.10):

$$\frac{\mathscr{C}(V^*, T^*)}{\mathscr{C}_H} = \frac{\beta_1}{[(\beta_2 T^*)^2 + (V^*)^2]^{1/6}}. \tag{3.15}$$

Here, β_1 and β_2 are numerical coefficients. Applying this fit to the curves shown in Fig. 3.2 gives a reasonably good fit with $\beta_2 \approx 8$, suggesting that the capacitance plateaus at about $V^* = 8T^*$, as compared to the theoretically estimated value $V_c^* = 11T^*$.

3.4 Electrode material: from perfect to poor metal

So far we have assumed that the electrode is a perfect metal, or in other words, that the screening radius b of the metal is much smaller than the ion diameter a. This assumption is justified for RTILs with large ions and electrodes made from a good metal. Experiments on such systems have indeed reported large capacitance that declines with absolute value of voltage [85] (the C–V curve is "bell-shaped"). However, for smaller ions and for electrodes made from semi-metals, such as graphite or glassy carbon, experimental values of $C(V = 0)$ are smaller and the $C(V)$ curves are "camel-shaped", *i.e.* the capacitance grows parabolically near $V = 0$ [85, 86, 87].

In order to interpret this difference qualitatively, let us recall that in such poor metals the density of states at the Fermi level is relatively small and the screening radius b of the metal may become comparable to $a/2$. As a result, the image potential changes. When $b < a/2$ one can think that the electric field produced by ions at the metal surface is relatively weak and slowly-varying. In such a case the screening charge of the metal is effectively situated at the distance b away from the metal surface, *i.e.* at $z = -b$. Therefore, the reflection plane for the image charge is at $z = -b$, so that an ion

at distance z from the surface experiences a smaller attraction $-e^2/16\pi\varepsilon_0(z+b)$ to the surface, rather than the standard $-e^2/16\pi\varepsilon_0 z$ for a perfect metal. At the distance of closest approach $z = a/2$, the ion-to-surface attraction energy becomes $-e^2/8\pi\varepsilon_0(a+2b)$. This leads to a finite energy cost E_0 for dissociating a bulk ion pair and bringing it to the metal surface, given by $E_0 = e^2/4\pi\varepsilon_0[a^{-1} - (a+2b)^{-1}]^{-1}$. Thus, a finite voltage is necessary to break pairs in the bulk and obtain free ions which can provide screening. This means that, for an electrode with finite screening radius b, the bell-shaped $C(V)$ curve splits into two peaks located at $V = \pm E_0/e$, thereby becoming camel-shaped, in agreement with the above-mentioned data.

The capacitance $C(V)$ at $V > E_0/e$ can be estimated with the help of the theory in Sec. 3.3 leading up to Eq. (3.9). In this case, however, the voltage V in Eq. (3.9) should be replaced by $V - E_0/e$ and the dipole arm a should be replaced by the longer arm $a + 2b$. These substitutions give

$$\mathscr{C}(V) = 1.3\left(\frac{e}{4\pi\varepsilon_0(a+2b)(V-E_0/e)}\right)^{1/3}\frac{a}{a+2b}\mathscr{C}_H \tag{3.16}$$

for $V > E_0/e$. Since the dipole-dipole repulsion is much stronger due to the longer dipole arm, $\mathscr{C}(V)$ is substantially smaller and reaches its geometrical limit $\mathscr{C}_H(b) = \mathscr{C}_H \cdot a/(a+2b)$ at a smaller voltage $V - E_0/(e^2/4\pi\varepsilon_0 a) = 5\eta e/16\pi\varepsilon_0(a+2b)$, or $V^* - E_0/(e^2/4\pi\varepsilon_0 a) \approx 5.5/(1+2b/a)$. Starting from this voltage the capacitance saturates at the level of $\mathscr{C}_H(b)$.

Only at even larger voltage $V^* - E_0/(e^2/4\pi\varepsilon_0 a) \gtrsim [5.5a^2 + 8\pi b(a+b)]/[a(a+2b)]$ do counterions comprise a full layer at the surface, after which the theory of multi-layer arrangement of ions [12] becomes applicable. This same behavior for $\mathscr{C}(V)$ is expected in the case where a good metal is covered by a thin insulating layer, for example, its own oxide.

In order to verify this theory we repeated our MC calculations for $T^* = 0.04$ and $Na^3 = 0.5$ using a relatively large $b = a/2$, which is at the limit of applicability for linear screening by the electrode surface. For simplicity, we have also assumed that the metal ion lattice has the same dielectric constant as our RTIL. Results are shown on Fig. 3.3, plotted as a function of V^* and σ^*. As expected, the peak at $V = 0$ is split into a camel-like structure (we show only the positive half of the symmetric C–V curve). The characteristic dimensionless voltage of the peak is $V_p^* \approx 0.5$, in agreement with the

above estimate for E_0. Note that the capacitance maximum occurs at $\sigma^* = 0.1$ and is apparently not related to excluded volume effects among counterions. As predicted by Eq. (3.16), the peak capacitance $\mathscr{C}(V_p^*)$ is approximately 2.5 times smaller than at $b = 0$ [recall that $\mathscr{C}_H(b)$ in Fig. 3.3 is twice smaller than $\mathscr{C}_H$ in Fig. 3.2].

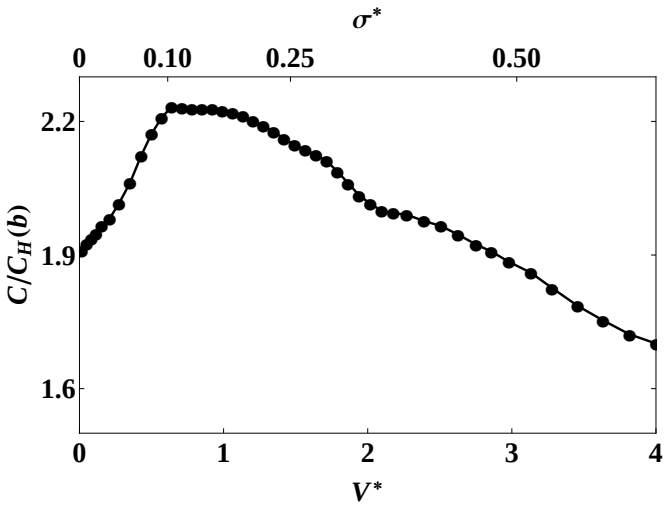

Figure 3.3: The ratio of the capacitance of the metal/RTIL interface C to the geometrical capacitance $C_H(b)$, plotted as a function of dimensionless voltage V^* (bottom axis) and charge density σ^* (top axis) for a system with ion density $Na^3 = 0.4$ and metal screening radius $b = a/2$. The capacitance is determined by a numerical derivative of the σ vs. V data obtained from a MC simulation at temperature $T^* = 0.042$.

3.5 Conclusion

To summarize, this chapter is concerned with Monte Carlo simulations of the restricted primitive model of a RTIL at a metal interface. Within this model, we obtain capacitance at zero voltage as large as $3\mathscr{C}_H$. We also find that for a good metallic electrode at small voltage, $\mathscr{C}$ decreases with T as $T^{-1/3}$. When the temperature is fixed and is relatively small, $\mathscr{C}(V)$ decreases as $1/V^{1/3}$ (the C–V curve is "bell-shaped"). On the other hand, when the electrode is made from a semi-metal the C–V curve is "camel-shaped", meaning that the capacitance first grows with V and then goes through a maximum and decays as $1/V^{1/3}$. We interpret these results with the help of a semi-quantitative analytical theory based on the weak repulsion between ion-image dipoles. Our conclusions

are in qualitative agreement with experimental data.

While there are a number of effects ignored by the primitive restricted primitive model — asymmetry of anion and cation sizes, polarizability of ions, and disorder at the electrode surface, to name a few — our results may be quite relevant for real-world experiments on room temperature ionic liquids. A typical ionic liquid has anions and cations with diameter $a \sim 1$ nm, which apparently corresponds to a Helmholtz capacitance $\mathscr{C}_H \sim 2\ \mu\mathrm{F/cm}^2$ and a dimensionless temperature $T^* \sim 0.02$. This temperature is extremely low, and within the assumptions of the RPM would imply crystallization of ions in the bulk. However, in real RTILs the ions are polarizable, which means that the bulk of the RTIL has a dielectric constant $\varepsilon > 1$ that reduces the magnitude of interactions at long distances; typically $\varepsilon \sim 3$. Thus, T^* should generally be replaced by $\varepsilon T^* \sim 0.06$ and $\mathscr{C}_H$ by $\varepsilon\mathscr{C}_H \sim 6\ \mu\mathrm{F/cm}^2$. In this sense, our result that in the RPM the capacitance can be as large as $3\mathscr{C}_H$ should be taken as an indication that polarizable RTILs can have $\mathscr{C} \sim 3\varepsilon\mathscr{C}_H = 18\ \mu\mathrm{F/cm}^2$, a value that is in agreement with typical capacitance measurements on RTILs [85, 86, 87]. The typical electrochemical stability window of about 6 Volts corresponds to $\varepsilon|V^*| \lesssim 12$, which is well within the range of our predictions [88].

Finally, we note that if both ionic species have the same polarizability, then our basic description of the interface remains valid. Polarizability of ions modifies both the attraction energy between ions and the attraction energy between an ion and its image. However, the attraction energy of a pair of oppositely-charged, polarizable ions in the bulk is still equal to the sum of the attraction energies of the two ions to the metal surface, so that at zero voltage the metal surface is highly populated by dissociated ions. At small finite voltage, excess ions seek to maximize their distance from each other, and the resulting correlations allow $\mathscr{C} > \mathscr{C}_H$ in the way described by Sec. 3.3.

Chapter 4

Volumetric capacitance of an electric double layer supercapacitor

4.1 Introduction

In an EDLC, energy is stored at the interface between an electron-conducting (metallic) electrode and an electrolyte or ionic liquid via the reversible adsorption of ions onto the electrode surface, as discussed in Sec. 1.1. In this way, counterions adsorbed onto the charged electrode effectively comprise the second half of a parallel-plane capacitor whose thickness is equal to the radius $a/2$ of the ions. If the charge of these ions is described as a uniformly charged plane, as in the mean-field approach, then one arrives at a capacitance C which is equal to the Helmholtz capacitance

$$C_H = 2\varepsilon_0 \varepsilon A/a. \tag{4.1}$$

In mean-field theories of the EDL, C_H/A plays the role of a maximum possible capacitance per unit area. As an example, for $\varepsilon = 2$ and $a = 1$ nm Eq. (4.1) gives $C_H/A \approx 3$ μF/cm^2.

For practical applications, a supercapacitor is best characterized not by its capacitance per unit area, C/A, but by its capacitance per unit mass or per unit volume ("volumetric capacitance"). For this reason, there has been much emphasis on the

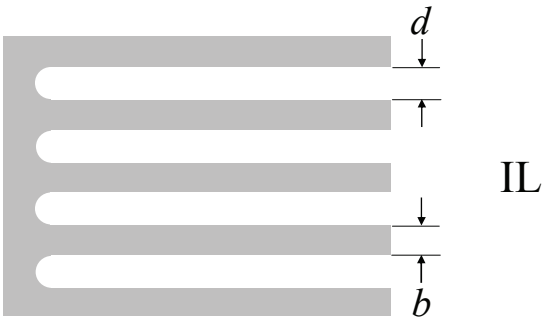

Figure 4.1: A schematic picture of the cross-section of a highly porous supercapacitor electrode. The solid, metallic electrode (gray area) has deep, planar pores of width d, separated by walls of thickness b. The electrode is open on one side to an ionic liquid (IL) or a concentrated electrolyte. See also Fig. 1.6.

development of conducting materials with very high specific surface area that can be used as electrodes. Among the more promising candidates are highly porous carbons [11, 89, 90] and carbon nanotube "forests" [91]. In such devices the specific surface area $\mathbb{A}$ can be as high as $\mathbb{A} = 1000$ m^2/cm^3. To understand how this is possible, one can imagine an electrode with slit-like pores of width $d = 1$ nm separated by conducting walls with thickness $b = 1$ nm (Fig. 4.1). For the sake of argument, we take this electrode to be the anode; one can imagine that the cathode is its mirror reflection to the right. In a supercapacitor device, the anode and cathode are electrically isolated by a membrane that is penetrable to the ions, so that the well-conducting ionic liquid between them forms EDLs on the tortuous surfaces of both electrodes. In this way the supercapacitor consists of two double layer capacitors in series; in this chapter we are concerned with calculating the anode capacitance.

If the electrode in Fig. 4.1 is placed in contact with an ionic solution with $\varepsilon = 2$ and $a = 1$ nm, then the Helmholtz expression of Eq. (4.1) predicts a volumetric capacitance $\mathbb{C} \approx 30$ F/cm^3. In fact, capacitance values as large as $\mathbb{C} = 100$ F/cm^3 have been reported for such devices [11, 92]. How is this possible?

In order to resolve this puzzle, let us briefly return to the problem of a planar, non-porous double layer capacitor. It has been shown (Ref. [35], Ch. 3) that the capacitance per unit area of an EDL is not necessarily limited by the Helmholtz value. When the charge on a planar electrode is small enough that adsorbed ions are separated from

each other by a distance much larger than their diameter a, the mean-field approach fails and the effects of electronic polarization of the electrode surface must be taken into account. In particular, when the electrode is made from a good metal, each ion forms an image charge in the electrode surface. The ion and its image charge together make an electric dipole which repels adjacent ions by a screened $1/r^3$ interaction rather than the normal $1/r$ interaction. Such a reduced interaction, along with the positional correlations between adsorbed ions, allows the capacitance of a single interface to be as much as three times larger than C_H in practical situations. The crucial importance of image forces for the structure and capacitance of the EDL has been recognized by a number of previous authors (see, for example, Refs. [82, 93, 94] and the very recent publication of Ref. [95]).

The notion of a double-layer comprised of ion-image dipoles is also relevant for describing porous, metallic supercapacitor electrodes (Fig. 4.1), provided that the width d of the pores is much larger than the ion diameter a, so that opposite walls of a pore have independent, non-interacting EDLs [see Fig. 4.2(a)]. For electrodes with such wide pores, enhanced capacitance can be explained using the theory of Ref. [35]. However, in supercapacitors where d is comparable to a, EDLs on opposite walls of a nanopore merge and new physics should emerge. Indeed, recent experiments by Gogotsi and co-workers have demonstrated a surprising increase in the capacitance as the width of pores in a carbon-based electrode is made comparable to the diameter of bare ions in an organic electrolyte [96] or in an ionic liquid [92].

In order to explain these results, one can try to extend the Helmholtz mean-field approach to the case of a narrow pore by replacing the charge of ions in the pore by two identical, coinciding, uniformly-charged planes located midway between the pore's two walls (see the result of a similar approach for cylindrical pores in Ref. [97]). In this picture, each of the charged planes forms a Helmholtz capacitor with one of the pore's metal walls, so that the total capacitance is $2C_H$, as it would be for a much wider pore. Thus, the mean-field approach cannot capture the unique effect of narrow pores.

Going beyond the mean-field level, however, one can recall that charges confined within a narrow nanopore create an infinite series of image charges in the two conducting electrode walls [Fig. 4.2(b)]. This leads to an interaction between ions which decays

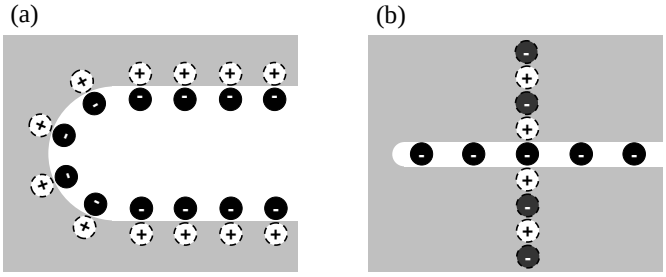

Figure 4.2: Schematic depiction of anions (black circles) neutralizing a positively charged nanopore in a metallic anode (solid gray area). (a) When the pore width is large compared to the ion diameter, opposite walls of the pore have independent EDLs and every anion can be said to have a single positive image charge (white circles with dashed outline). (b) When the pore width is comparable to the anion radius, anions form a two-dimensional (2D) charged layer within the pore. Each anion has an infinite series of image charges (white and dark gray circles with dashed outlines), which produce an exponential interaction between neighboring anions. For clarity of illustration, image charges are shown for one anion only.

exponentially with the distance between them.[1]

In a recent paper, Kondrat and Kornyshev [100] recognized that such an exponentially suppressed interaction can lead to large capacitance $C > C_H$ in the nanopore for reasons similar to those discussed in Ref. [35]. However, in calculating the capacitance, the authors of Ref. [100] imagined that the pore is filled with many anions and cations and they used a description where the small net charge is spread equally among *all* ions in the pore. The total electrostatic energy was then calculated using the exponential interaction evaluated at the average distance between all ions. Such an approach can be called a semi-mean-field approximation and does not lead to quantitatively correct results, as we will show below.

In the present chapter, as in Ch. 3, we completely abandon the mean-field approach in order to address a fundamental question: how large can the volumetric capacitance of an EDL supercapacitor be? We construct a theory which takes into account correlations between discrete anions and the screening of the Coulomb interaction by the conducting electrode surface. We consider explicitly two cases for the electrode material. First, we

[1] This exponential interaction has been used previously [98] in order to describe mesoscopic oscillations in the capacitance of a disc-like island of a classical two-dimensional electron gas between two metallic, planar electrodes as a function of the number of electrons in the island. Such an electron gas, confined at the periphery by a cylindrical later gate, constitutes a vertical quantum dot [99].

examine the case where the electrode can be considered a perfect metal (Sec. 4.2) and we verify our theoretical predictions with a simple Monte Carlo (MC) simulation (Sec. 4.3). We find that under realistic circumstances the capacitance per unit area can be up to ten times the Helmholtz value, with the corresponding volumetric capacitance as large as 150 F/cm^2. Secondly, we analyze the case where the electrode is an imperfect metal with a screening radius comparable to the pore width (Sec. 4.4). The crossover between this theory and that of Sec. 4.2 is carefully discussed. In Sec. 4.5 we consider how our theory applies to supercapacitors made with graphitic carbon electrodes, and we argue that at not-too-small voltages the graphite is well approximated as a good metal due to the strong effect of nonlinear screening. We close in Sec. 4.6 by briefly examining a different model of a porous supercapacitor, where the electrode is made from a random assembly of conducting spheres that are three-dimensionally connected, and show that very large volumetric capacitance can result in this situation as well.

4.2 Capacitance of a single 2D metal pore

In this section we consider an electrode made from a perfect metal which has deep, planar pores of width d (Fig. 4.1). Such pores are assumed to be in contact with an ionic liquid described by the restricted primitive model: a neutral mixture of hard-core monovalent ions with the same diameter a. We assume that $a \leq d$, so that ions can enter the pores. We also assume that $d - a \ll a$, so that ions in the pore can be described as a 2D liquid. A voltage source provides the positive potential difference V between the electrode and the bulk of the ionic liquid that attracts anions into the pore. If Q is the amount of electronic charge that has moved through the voltage source onto the electrode relative to the state at $V = 0$, then the differential capacitance of the EDL is defined as $C = dQ/dV$.

In principle, at $V = 0$ the pore may already contain some finite and equal number of anions and cations. In this case, a reliable analytical calculation of the total electrostatic energy $U(Q)$, which is necessary for calculating the capacitance, is very difficult. Therefore, the effect of allowing both ionic species to simultaneously enter the pore is examined only numerically at the end of Sec. 4.3.

This chapter concentrates instead on the case when the pore is empty at $V = 0$.

This situation results when the chemical potential of ions in the ionic liquid is lower than the free energy per ion in a filled, neutral pore. Such a difference in chemical potential can arise from two sources. First, ions in a three-dimensional (3D) ionic liquid are surrounded by a larger number of oppositely-charged neighbors, which lowers the interaction part of the chemical potential outside the pore. Second, when the width d of the pore is close to the ion diameter a, the entropic contribution to the chemical potential inside the pore increases sharply. For the case of electrolyte solutions, there is also a positive contribution to the chemical potential associated with the necessity of stripping the solvation shell from each ion that enters the pore.

We therefore assume that the pores are empty at $V = 0$. As the voltage is increased from zero, the pores remain empty until some finite voltage $V = V_t$. At $V > V_t$ the pores of the anode begin to fill with anions, while cations remain away from the anode. This picture allows us to formulate a simple analytical calculation of the total energy U, presented below, based on the repulsion between anions in the pore.

Our general approach to calculating the capacitance is as follows. We first describe the total electrostatic energy $U(n)$ associated with the lowest energy configuration of n anions per unit area in the pore. If entropic effects are ignored, then the value of the charge Q of the pore is that which minimizes the system's total energy $U - QV$, where the term $-QV$ represents the work done by the voltage source. Using the equilibrium condition $d(U - QV)/dQ = 0$ along with $Q = eAn$ gives

$$V = \frac{dU}{dQ} = \frac{1}{eA}\frac{dU}{dn}. \tag{4.2}$$

The differential capacitance of the pore $C = (dV/dQ)^{-1}$ can therefore be written

$$C = e^2A^2\left(\frac{d^2U}{dn^2}\right)^{-1}. \tag{4.3}$$

The capacitance can be expressed as a function of voltage, $C(V)$, by combining Eqs. (4.2) and (4.3).

In the remainder of this section we first calculate the capacitance of the pore in the zero temperature limit and then estimate the effect of the ions' finite thermal energy.

We begin our theoretical description by noting that a point charge e located in the plane halfway between two metal walls creates an electric potential within that plane

equal to [101]

$$\phi(r) = \frac{e}{\pi\varepsilon_0\varepsilon d}\sum_{n=1}^{\infty} K_0[\pi(2n-1)r/d]. \tag{4.4}$$

Here, r is the radial distance from the point charge, d is the distance between the metal walls (the pore width), and $K_0(x)$ is the zeroth order modified Bessel function of the second kind. At distances $r > d$, Eq. (4.4) can be expanded to lowest order to give

$$\phi(r) \simeq \frac{2\sqrt{2}\exp[-\pi r/d]}{\sqrt{r/d}}\frac{e}{4\pi\varepsilon_0\varepsilon d}. \tag{4.5}$$

Since the sub-leading-order term of Eq. (4.4) is exponentially smaller than that of Eq. (4.5), this approximation has a negligible effect on the capacitance and we use Eq. (4.5) everywhere in further calculations.

When a given area density n of anions is inside the metal pore, the repulsive interaction between anions induces strong positional correlations. In their lowest energy configuration, the anions form a strongly-correlated liquid, reminiscent of a 2D Wigner crystal, where anions are separated from their nearest neighbors by a well-defined spacing $\sim n^{-1/2}$. In such an arrangement the total repulsive energy among anions is minimized while maintaining the area density required to neutralize the electrode.

If we postulate a crystalline arrangement of the anions, then the electrostatic energy U of this state can be calculated exactly by making use of the interaction potential in Eq. (4.5). Due to the short-ranged nature of the interaction, this energy is well approximated by considering only nearest-neighbor interactions in a square lattice of anions. Such an approach gives

$$\begin{aligned} U(n) &= 2nAe\phi(n^{-1/2}) - (\mu-u)nA \\ &= 4\sqrt{2}\frac{A}{d^2}(nd^2)^{5/4}\exp\left[-\pi/\sqrt{nd^2}\right]\frac{e^2}{4\pi\varepsilon_0\varepsilon d} \\ &\quad -(\mu-u)nA. \end{aligned} \tag{4.6}$$

The term $-(\mu-u)nA$ takes into account the voltage-independent energy associated with bringing each anion from the bulk of the ionic liquid into the pore; μ is the chemical potential of ions in the bulk of the ion liquid and u is the self-energy of an anion in the pore. The term $-(\mu-u)nA$ is linear in n and therefore, by Eq. (4.3), disappears from the capacitance. Its only effect is to produce a finite threshold voltage $V_t = -(\mu-u)/e$

required to bring anions into the metal pore, as discussed above. Our theory treatment assumes that $-(\mu - u) > 0$.

Taking the derivative dU/dQ as in Eq. (4.2), we find an expression for the voltage in terms of the ion density:

$$V - V_t \simeq \frac{2\pi\sqrt{2}\exp[-\pi/\sqrt{nd^2}]}{(nd^2)^{1/4}}\frac{e}{4\pi\varepsilon_0\varepsilon d}. \tag{4.7}$$

Similarly, the capacitance can be evaluated by Eq. (4.3), which gives

$$C \simeq \frac{\sqrt{2}a}{\pi d}(nd^2)^{7/4}\exp[\pi/\sqrt{nd^2}]C_H. \tag{4.8}$$

In the limit $n \ll 1/d^2$, Eqs. (4.7) and (4.8) can be combined to give an analytical expression for the capacitance as a function of voltage at small $V - V_t$:

$$C \simeq 32\pi^3\left(\frac{e/4\pi\varepsilon_0\varepsilon d}{V - V_t}\right)\ln^{-3}\left[8\pi^2\left(\frac{e/4\pi\varepsilon_0\varepsilon d}{V - V_t}\right)^2\right]\frac{a}{d}C_H. \tag{4.9}$$

For larger voltages corresponding to $(V - V_t)/(e/4\pi\varepsilon_0\varepsilon d) \gtrsim 0.1$ the capacitance is well-described by the power law relation

$$C \simeq 3.5\left(\frac{V - V_t}{e/4\pi\varepsilon_0\varepsilon d}\right)^{-0.4}\frac{a}{d}C_H. \tag{4.10}$$

Eqs. (4.8) and (4.9) suggest that at low ion density (or small $V - V_t$) the capacitance can be much larger than the Helmholtz value. This result can be understood physically by noting that at such low ion densities the fractional coverage of excess ions on the electrode surface $na^2 \ll 1$, so that it is incorrect to think of the EDL in the mean-field way: as a uniform layer of surface charge. Rather, the neutralizing ionic charge consists of discrete ions whose interaction is exponentially small due to the aggressive screening by the metal pore. Positional correlations among these ions help them to avoid each other, resulting in a lower energy than what is possible in mean-field descriptions of the EDL and therefore in larger capacitance that is not limited by the physical distance $a/2$ between the electrode and its countercharge. With growing ion density, the capacitance decreases, until at some finite voltage V_{max} the density of ions in the pore reaches its steric limit: $n \simeq 1/a^2$. By Eq. (4.7),

$$V_{max} \simeq 2\pi\sqrt{\frac{2a}{d}}\exp[-\pi a/d]\frac{e}{4\pi\varepsilon_0\varepsilon d}. \tag{4.11}$$

Fig. 4.3 shows the capacitance as a function of voltage, $C(V)$, plotted for the cases $d = a, 1.5a, 2a$.

If the width of pores in the electrode is increased, the capacitance decreases, as shown in Fig. 4.3. In the limit where the pore thickness $d \gg a$, as in Fig. 4.2(a), the capacitance can be described using a theory of independent EDLs comprised of ion-image dipoles. Such an approach gives $C \approx 1.3C_H$ per interface [35] at $na^2 = 1$ (the relatively flat tail of the C–V curve) and $C_{max} \approx 3C_H$ per interface at $n \to 0$, so that the total capacitance per pore is smaller than the result shown in Fig. 4.3 by more than two times. As mentioned above, this "anomalous" increase in the capacitance for narrow pores is the result of the strong, exponential screening that results from the presence of two close metal walls [Fig. 4.2(b)].

Formally, Eq. (4.8) diverges as the density of ions vanishes ($V - V_t$ goes to zero). Of course, this expression neglects entropic effects among the ions, which are important in the limit where ions in the pore are so sparse that their typical interaction energy is smaller than the thermal energy k_BT. At such low densities the correlated, lattice-type structure of ions in the pore disappears and we obtain a finite capacitance at $(V - V_t) \to 0$.

In order to estimate the value of this capacitance maximum, we note that when $e\phi(n^{-1/2}) \ll k_BT$ the total free energy F can be written using a truncated virial expansion:

$$F \simeq F_{id} + An^2 k_BT B(T) - eAn(V - V_t). \tag{4.12}$$

Here, $F_{id} = Ank_BT \ln(na^2)$ is the free energy of a two-dimensional ideal gas and $B(T)$ is the second virial coefficient. $B(T)$ is calculated from the interaction energy $e\phi(r)$ between two ions [Eq. (4.5)] as

$$B(T) = \frac{1}{2}\int_0^\infty \left(1 - \exp\left[-\frac{e\phi(r)}{k_BT}\right]\right) 2\pi r dr \tag{4.13}$$

$$\simeq \frac{d^2}{8\pi} \ln^2\left[\frac{16\pi}{(T^*)^2}\right]. \tag{4.14}$$

Here, T^* is defined as the dimensionless temperature

$$T^* = \frac{k_BT}{e^2/4\pi\varepsilon_0\varepsilon d}. \tag{4.15}$$

As an example, room temperature corresponds to $T^* \approx 0.04$ for an ionic solution with dielectric constant $\varepsilon = 2$ in a pore with $d = 1$ nm. At temperatures that are not

very large, $T^* \lesssim 0.5$, the virial coefficient $B(T)$ is larger than the physical area $\pi a^2/4$ occupied by each ion, so that the hard-core interaction between ions is unimportant for the virial expansion.

As before, we can use the equilibrium condition $\partial F/\partial n = 0$ to give a relation between the voltage and the ion density n:

$$e(V - V_t) = k_B T \left[2nB(T) - \ln\left(1/na^2\right)\right]. \tag{4.16}$$

The capacitance can also be related to n according to $C = e^2 A^2 (\partial^2 F/\partial n^2)^{-1}$, which gives

$$C = \frac{nd^2}{T^*[1 + 2nB(T)]} \frac{a}{d} C_H. \tag{4.17}$$

According to Eq. (4.16), in the limit $(V - V_t) = 0$ the ion density approaches $n = W_0[2B(T)/a^2]/2B(T)$, where $W_0[x]$ is the principle branch of the Lambert W function ($W_0[x] \approx \ln x$ for $x \gg 1$). Over the experimentally relevant range of temperature $0.03 < T^* < 1$, the value of $W_0[2B(T)/a^2] \approx 1$, so that Eqs. (4.16) and (4.17) can be combined to give the following approximate relation for the capacitance at $V = V_t$ as a function of temperature:

$$C_{max}(T) = \frac{\gamma}{T^* \ln^2\left[16\pi/(T^*)^2\right]} \frac{a}{d} C_H. \tag{4.18}$$

Here γ is a numerical constant; Eq. (4.14) suggests $\gamma = 4\pi^2 \approx 39$, while MC simulations (see Fig. 4.4 in the following section) give $\gamma = 34 \pm 1$. This is a surprisingly good agreement, considering that C_{max} is determined by a relatively large ion density $n \sim 1/B(T)$, which is at the limit of applicability of the truncated virial expansion of Eq. (4.12). Indeed, Eq. (4.12) is applicable only in the "gas phase" corresponding to $nB(T) \ll 1$, which is realized at $V < V_t$. On the other hand, Eq. (4.12) fails completely in the high-density correlated liquid phase, where $nB(T) \gg 1$ and the potential energy of repulsion between anions [see Eq. (4.6)] dominates the entropic contribution to the free energy. A more complete theory of the capacitance at finite temperature and large ion density would require a theory of the free energy of ions in the liquid state and cannot be captured by the truncated virial expansion presented here. The zero temperature analytical result of Eq. (4.10), however, should be accurate in the limit where the thermal energy $k_B T$ is small compared to the typical interaction energy $e\phi(n^{-1/2})$. At

room temperature and for $d = 1$ nm and $\varepsilon = 2$, this corresponds to moderately large ion density $nd^2 \gtrsim 0.3$.

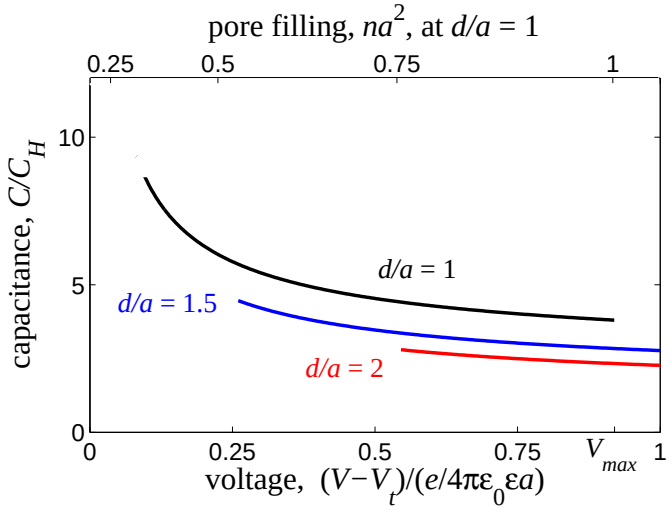

Figure 4.3: The capacitance in units of C_H of a 2D metal nanopore with width d, plotted as a function of dimensionless voltage (lower axis) according to Eqs. (4.7) and (4.8). Different curves are labeled by their corresponding value of d/a and are truncated at their corresponding value of C_{max} as given by Eq. (4.18); here, $T^*a/d = 0.04$. V_{max} is shown for $d/a = 1$, and the top axis shows the ion concentration for this same case.

The above results for the capacitance of a single metal pore can be used to calculate the total capacitance of the electrode by multiplying by the number of pores in the electrode. Thus, the total volumetric capacitance $\mathbb{C}$ is given by $\mathbb{C} = (\varepsilon_0\varepsilon\mathbb{A}/a) \cdot C/C_H$. As an example we can consider the electrode depicted in Fig. 4.1, with $d = b = 1$ nm, in contact with an ionic liquid with $\varepsilon = 2$ and $a = d$. For such a capacitor the mostly flat tail of the C–V curve of Fig. 4.3, where $C/C_H \approx 4.5$, corresponds to $\mathbb{C} \approx 90$ F/cm^3. If the electrode can be treated as a perfect metal, then such a capacitor would demonstrate a peak in the differential capacitance at a particular voltage V_t, as in Fig. 4.3. For $T^* = 0.04$, $\mathbb{C}_{max} \approx 150$ F/cm^3.

4.3 Monte Carlo simulation of a 2D metal pore

In order to verify the theoretical predictions of the previous section, we perform MC simulations of a 2D metal pore open to a reservoir of positive and negative hard-sphere ions. Our general approach is to use the Grand Canonical Monte Carlo (GCMC) method to impose a difference in chemical potential between positive and negative ions in the system, thereby simulating an applied voltage V. Specifically, the chemical potential of each ion type is specified according to

$$\mu_{\pm} = \mu \mp eV, \tag{4.19}$$

where μ is the chemical potential of the reservoir. The number of each ion species is allowed to fluctuate with time. We use our simulation to measure the resulting equilibrium number of positive and negative charges in the pore at a given V, which defines the net charge $Q(V)$. The capacitance of the pore is calculated by the discrete derivative dQ/dV.

The details of our simulation method are as follows. We begin each simulation by randomly placing 100 of each type of ion on a square 2D plane of area $A = 20 \times 20d^2$ and stipulating the dimensionless temperature T^* [see Eq. (4.15)] and the dimensionless voltage $V^* = V/(e/4\pi\varepsilon_0\varepsilon d)$. The ion diameter a is taken to be equal to the pore width d. Before any data is taken, ions are allowed to take 10^5 GCMC steps to reach equilibrium. The number of positive and negative ions, M_+ and M_-, respectively, are then averaged over the following 30 to 50×10^6 GCMC steps. The charge of the electrode is defined as $Q = e(M_- - M_+)$ and the capacitance is given by the discrete derivative $C(V) \approx [Q(V + \Delta V/2) - Q(V - \Delta V/2)]/\Delta V$. Care is taken to ensure that all results are independent of the initial ion configuration.

Following the standard GCMC procedure [102], one GCMC step consists of either an attempted move by a randomly-chosen ion or the attempted addition or removal of an ion from the system. Attempted moves occur more often than attempted addition/removal at a ratio of 9 : 1. We give the simulation area periodic boundaries, so that an ion leaving one edge enters at the opposite edge. The total electrostatic energy U_{tot} of a given configuration of ions is calculated as

$$U_{tot} = \frac{1}{2}\sum_{i,j} q_i q_j e\phi(r_{i,j}), \tag{4.20}$$

where r_{ij} is the distance between ions i and j (found using the minimum image convention [103]), $q_i = \pm 1$ is the sign of ion i, and $\phi(r)$ is the interaction law given by Eq. (4.5). Attempted moves and addition/removal events are accepted and rejected based on the corresponding change in U_{tot}, as given by the traditional acceptance rules for GCMC [102]. The ions are treated as hard spheres, so that only those moves/additions/removals resulting in non-overlapping ions are accepted. For a more detailed discussion of the GCMC method see Refs. [103, 104].

Fig. 4.4 shows the capacitance measured by our GCMC simulation as a function of voltage for a system with $V_t^* = V_t/(e/4\pi\varepsilon_0\varepsilon d) = -(\mu^* - u^*) = 0.3$, calculated at four different dimensionless temperatures. In this situation, the pore is essentially empty of ions at $V = 0$ and at positive voltages contains only one ionic species, so that its capacitance is well described by the analytical theory of Sec. 4.2. Both the voltage and temperature dependence of the capacitance correspond closely to analytical predictions. Larger voltages could not be examined by our simulation since these correspond to large ion fillings $na^2 \sim 1$ (see the top axis of Fig. 4.3), at which the simulation fails to reach equilibrium in a reasonable amount of time.

So far we have dealt only with pores that are empty at $V = 0$. In the remainder of this section we use the GCMC simulation to qualitatively examine a pore containing a substantial, neutral concentration of both anions and cations at $V = 0$. To arrive at such a situation, one should increase the chemical potential μ, causing the value of V_t to decline.[2]

Fig. 4.5 shows, as an example, the capacitance of a pore with $\mu^* - u^* = 0$, which corresponds to moderately large ion filling at $V = 0$. We also show a system with $V_t^* = 0.3$ for comparison. The pore with $\mu^* - u^* = 0$ (triangles) is more than half-filled at zero voltage: $(M_+ + M_-)a^2/L^2 \approx 0.63$. As the voltage is increased from zero, cations are driven out of the pore and anions are attracted to the pore until at $V^* \gtrsim 0.35$ only anions remain in the pore and the capacitance is reasonably well described by our

[2] In our MC simulations, we observe the value of the threshold voltage V_t^* to be equal to $-(\mu^* - u^*)$ when μ^* is large negative. At some particular value of $-(\mu^* - u^*) > 0$, however, the threshold voltage abruptly disappears and the pore is spontaneously filled with ions at zero voltage. Such a transition can be understood qualitatively by considering that when $(\mu^* - u^*) < 0$ it is not energetically favorable for single ions to enter the pore, but ions may still enter the pore in neutral pairs or larger neutral clusters. Thus, the location of the $V = 0$ empty-to-filled pore transition is related to the electrostatic energy per particle of an ion in a neutral cluster. For T^* between 0.02 and 0.07, we observe the threshold voltage to disappear at $-(\mu^* - u^*)$ between 0.08 and 0.12.

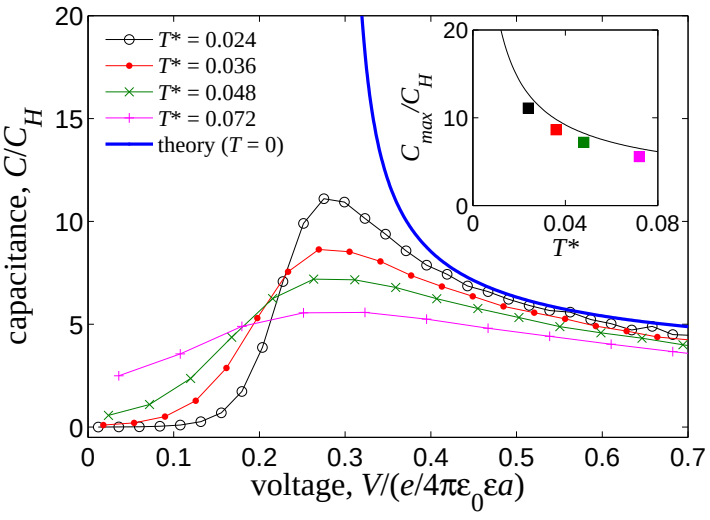

Figure 4.4: MC results for the capacitance C, in units of C_H, of a 2D metal pore with $V_t^* = 0.3$, plotted as a function of voltage for a range of temperatures T^*. The thick line shows the prediction of our analytical theory. For each temperature, the capacitance attains its maximum at $V^* \approx V_t^* = 0.3$. These maximum capacitances (shown in the inset by filled squares) can be described by Eq. (4.18) with $\gamma = 34 \pm 1$ (the theoretical curve with $\gamma = 4\pi^2$ is shown by the thin line).

analytic treatment of the previous section (as shown by the solid line). At $V^* < 0.35$, on the other hand, the strong attraction between cations and anions affects the capacitance. As a rough approach to explaining this data, one may imagine that at small voltage the net ionic charge consists of a small number Q/e of "excess anions" on the background of a large number of neutral, tightly-bound cation-anion pairs. These excess anions seek to maximize their distance from each other by forming a correlated, Wigner crystal-like arrangement in a way that is similar to the description of the previous section. Under this description, one may expect the same analytical theory to hold as for large negative μ^*, since the neutral pairs are essentially non-interacting and therefore play only a small role in determining the capacitance. Fig. 4.5 suggests that this approach gives a reasonably accurate description of the finite temperature truncation of the capacitance divergence. Indeed, the capacitance in limit $V^* + (\mu^* - u^*) = 0$ is very similar for the two C–V curves. However, this approach does not explain the weak capacitance maximum

at $V^* \approx 0.2$ in the C–V curve corresponding to $\mu^* - u^* = 0$, which remains a puzzle.

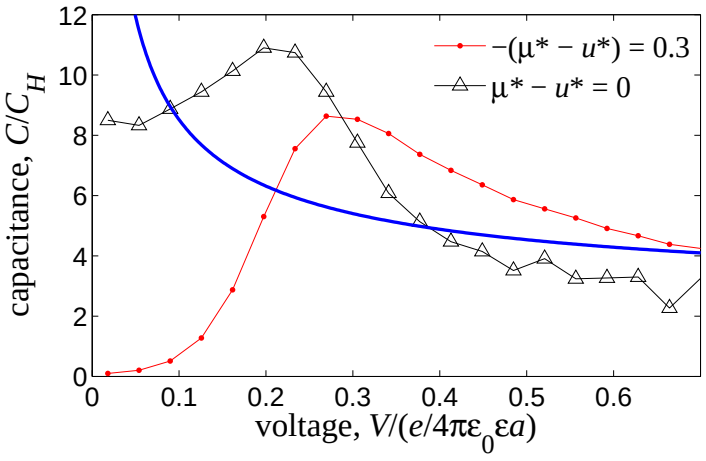

Figure 4.5: MC results for the capacitance of a 2D metal pore with $T^* = 0.04$ at $\mu^* - u^* = 0$ (triangles) and $-(\mu^* - u^*) = 0.3$ (circles). The thick line is the prediction of Eq. (4.10) with $V_t^* = -(\mu^* - u^*) = 0$.

This qualitative explanation of the filled pore data is similar to that of Ref. [35], but is fundamentally different from the approach of Ref. [100]. These authors assumed that the charge of excess anions is spread equally over all ions in the pore, with each ion getting a small fraction δe of the electron charge e. They further assumed [see their Eq. (3)] that every ion interacts with its nearest neighbors via the exponential interaction $(\phi(r)/e)(\delta e)^2$, where $\phi(r)$ is given by Eq. (4.5). Such a semi-mean-field approximation makes the total repulsive energy of excess anions larger than in our description of Sec. 4.2, since the distance between interacting ions is smaller and this changes the exponential factor of $\phi(r)$. Therefore, it seems reasonable that the pore capacitance evaluated in Ref. [100] is three times smaller than in our Fig. 4.5.

4.4 Capacitance of a porous imperfect metal

Thus far we have calculated the capacitance in situations where the electrode can be considered a perfect metal, or in other words where the electrode has a vanishing electronic screening radius. In this section we examine what happens to the capacitance when the electrode is not a perfect metal, but instead has a finite screening linear radius

r_s, given by

$$r_s = \sqrt{\frac{\varepsilon_0 \varepsilon}{e^2 \nu(\mu_F)}}, \tag{4.21}$$

where $\nu(\mu_F)$ is the electron density of states at the Fermi energy μ_F of the electrode.

Below we consider separately two limiting cases for r_s: (i) where $r_s \ll b$, the typical thickness of the wall separating adjacent pores, so that adjacent pores can be considered non-interacting, and (ii) where $r_s > b$, so that adsorbed ions interact three-dimensionally.

In the case where $r_s \ll b$, there is no interaction between adjacent pores and the volumetric capacitance can still be calculated as in the previous section, by considering the capacitance of a single pore. In this case the effect of finite screening radius is to shift the position of the reflection plane for image charges by a distance r_s beyond the surface of the pore wall [105]. This reflection plane coincides with the "electrostatic surface" of the pore, at which the center of gravity of the surface charge is effectively located. That is, a charge in the center of the pore becomes separated from its image charge by a distance $d + 2r_s$, as shown in Fig. 4.6. In this way the interaction between neighboring ions is stronger than what is given by Eq. (4.5) and the capacitance of the pore is reduced as compared to the results in Sec. 4.2. One can easily calculate the effect this has on the capacitance by replacing d with $d_{\text{eff}} = d + 2r_s$ in Eqs. (4.4) – (4.18). In other words, allowing for finite screening radius $r_s \ll b$ in the electrodes has the same effect as increasing the pore width (which is examined in Fig. 4.3). For example, a pore with width $d = 1$ nm and $r_s = 0.25$ nm would have $d_{\text{eff}}/d \approx 1.5$, and the capacitance would correspond to the middle (blue) curve in Fig. 4.3.

In the opposite limit, $r_s > b$, the wall of the pore does not completely screen the charge of an adsorbed cation and ions in adjacent pores interact with each other. In this limit ions interact three-dimensionally via a Yukawa-like potential

$$\phi(r) = \frac{e}{4\pi\varepsilon_0\varepsilon r} \exp\left[-\frac{r}{R_s}\right], \tag{4.22}$$

where R_s is the three-dimensional (3D) screening radius, determined from the volume-averaged density of states $\nu(\mu_F)b/(b+d)$:

$$R_s = \sqrt{\frac{\varepsilon_0 \varepsilon}{e^2 \nu(\mu_F)} \left(1 + \frac{d}{b}\right)} = r_s \sqrt{1 + \frac{d}{b}}. \tag{4.23}$$

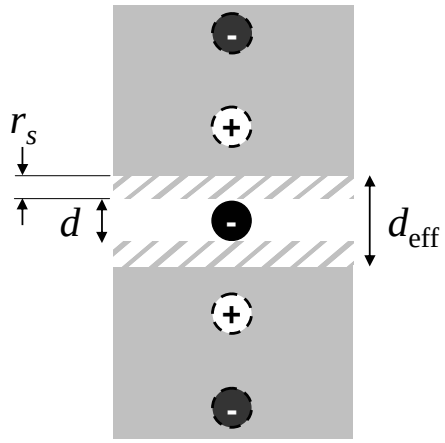

Figure 4.6: A schematic portrayal of the effect of finite screening radius $r_s \ll b$ in a conducting electrode (solid gray area). The reflection plane for image charges (black and white circles with dashed outlines) of an adsorbed cation (black circle) is shifted by a distance r_s from the wall of the pore (hatched area). Compare to Fig. 4.2(b).

For $d = b$ (as in Fig. 4.1), we get $R_s = \sqrt{2}r_s$.

In the limit of $R_s \gg N^{-1/3}$, where N is the three-dimensional concentration of ions inside the electrode, the electric potential Φ is uniform throughout the volume of the electrode and is given by

$$\Phi = eN \int_0^\infty \phi(r) 4\pi r^2 dr = \frac{eNR_s^2}{\varepsilon_0 \varepsilon}. \tag{4.24}$$

This gives for the volumetric capacitance

$$\mathbb{C} = \frac{\varepsilon_0 \varepsilon}{R_s^2}. \tag{4.25}$$

This result was first derived as the volumetric capacitance of charged DNA condensates with cationic polyelectrolytes in salty water [106, 107, 108].

At smaller $R_s < N^{-1/3}$, the discreteness of the ions plays an important role. In their lowest energy state, the ions form a correlated, 3D liquid in which they maximize their separation from each other while neutralizing the bulk charge of the electrode, as shown in Fig. 4.7. As in the previous section, we can calculate the capacitance by postulating a crystalline arrangement of the ions (a 3D Wigner crystal) and calculating the total electrostatic energy U. The capacitance can then be found using the 3D analogue of

Eqs. (4.2) and (4.3), namely

$$V = \frac{dU}{dQ} = \frac{1}{e\mathbb{V}}\frac{dU}{dN}, \tag{4.26}$$

$$C = e^2\mathbb{V}^2\left(\frac{d^2U}{dN^2}\right)^{-1}, \tag{4.27}$$

where $\mathbb{V}$ is the electrode volume.

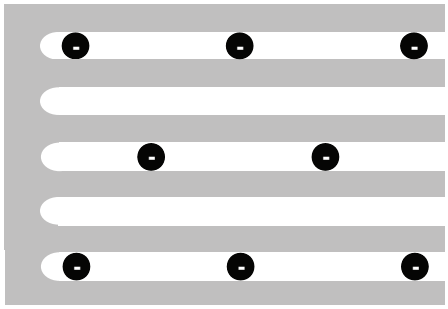

Figure 4.7: A schematic depiction of anions (black circles) arranging themselves within a porous supercapacitor electrode (solid gray area) in the limit $r_s > b$. Here, ions interact three-dimensionally, leading to a 3D Wigner-crystal-like arrangement of ions in the ground state.

This approach allows one to calculate $\mathbb{C}$ as a function of ion density N and as a function of voltage V. Using a numeric evaluation of the total energy U gives a capacitance that can be accurately fitted to the following power-law form at $(V - V_t)/(e/4\pi\varepsilon_0\varepsilon R_s) > 0.01$:

$$\mathbb{C}(V) = \left[1 + 0.22\left(\frac{V - V_t}{e/4\pi\varepsilon_0\varepsilon R_s}\right)^{-0.58}\right]\frac{\varepsilon_0\varepsilon}{R_s^2}. \tag{4.28}$$

This expression is plotted in Fig. 4.8.

Eq. (4.28) suggests that the capacitance diverges at small $V - V_t$, as in the case of 2D pores. To understand why this is the case, we can consider the limit where ions are sufficiently sparse that their separation is much larger than R_s. In this limit only the interactions between nearest-neighbors of the 3D Wigner crystal contribute significantly to the total energy. If we imagine a cubic lattice arrangement of ions, then we arrive at an energy

$$U \simeq 3\mathbb{V}\frac{e^2N^{4/3}}{4\pi\varepsilon_0\varepsilon}\exp\left[-\frac{1}{N^{1/3}R_s}\right]. \tag{4.29}$$

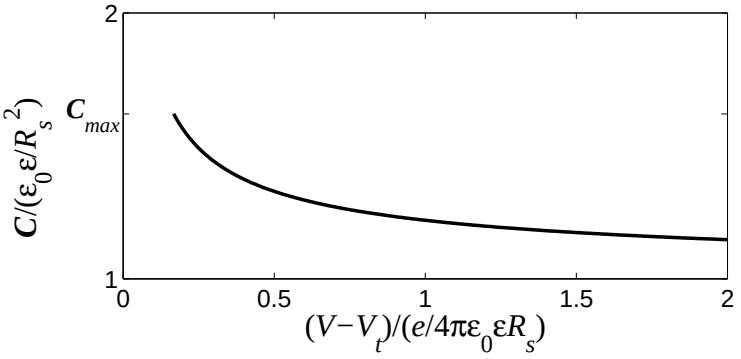

Figure 4.8: The volumetric capacitance $\mathbb{C}$, in units of $\varepsilon_0\varepsilon/R_s^2$, for the case where ionic charges obey the interaction law of Eq. (4.22), plotted as a function of dimensionless voltage. The curve is truncated at $\mathbb{C}_{max}$ as given by Eq. (4.38).

By Eqs. (4.26) and (4.27), this gives a voltage

$$V - V_t \simeq \frac{e}{4\pi\varepsilon_0\varepsilon R_s} \exp\left[-\frac{1}{N^{1/3}R_s}\right] \tag{4.30}$$

and a capacitance

$$C(N) \simeq 12\pi\varepsilon_0\varepsilon\mathbb{V}N^{4/3}R_s^2 \exp\left[\frac{1}{N^{1/3}R_s}\right]. \tag{4.31}$$

Combining these two relations gives an expression for the volumetric capacitance as a function of voltage, applicable at very small $V - V_t$:

$$\mathbb{C}(V) \simeq \frac{3}{R_s^3}\frac{e}{V - V_t} \ln^{-4}\left[\frac{e/4\pi\varepsilon_0\varepsilon R_s}{V - V_t}\right]. \tag{4.32}$$

Eq. (4.32) implies that at small $V - V_t$, where ions are sparse, the capacitance can be much larger than the mean-field result of Eq. (4.25). This growth in the capacitance is driven by the vanishing interaction [Eq. (4.22)] between discrete, correlated ions. The maximum value of the capacitance occurs at $(V - V_t) \to 0$ and is determined by thermal effects. This maximum can be estimated, as in the previous section, by making a virial expansion of the free energy

$$F \simeq F_{id} + \mathbb{V}N^2 k_B T B(T) - Q(V - V_t). \tag{4.33}$$

The value of the capacitance in this limit, as in Eqs. (4.17)–(4.18), is inversely related to the virial coefficient $B(T)$. At not too small R_s, such that $R_s \gtrsim a/2$,

$$\mathbb{C}_{max}(T) \simeq \frac{2\pi\varepsilon_0\varepsilon R_s}{\widetilde{T}B(T)}. \tag{4.34}$$

Here, $\widetilde{T}$ is a dimensionless temperature normalized to the interaction between two charges at a distance R_s:

$$\widetilde{T} = \frac{k_B T}{e^2/4\pi\varepsilon_0\varepsilon R_s} = \frac{R_s}{d} T^*. \tag{4.35}$$

The virial coefficient $B(T)$ is calculated as

$$B(T) = \frac{1}{2}\int_0^\infty \left(1 - \exp\left[-\frac{e\phi(r)}{k_B T}\right]\right) 4\pi r^2 dr \tag{4.36}$$

$$\simeq 2\pi R_s^3 \left(1 + \ln[1/\widetilde{T}] + \frac{1}{3}\ln^3[1/\widetilde{T}]\right), \tag{4.37}$$

so that Eq. (4.34) can be written

$$\mathbb{C}_{max}(T) \approx \frac{1}{\widetilde{T}\left(1 + \ln[1/\widetilde{T}] + \frac{1}{3}\ln^3[1/\widetilde{T}]\right)} \frac{\varepsilon_0\varepsilon}{R_s^2}. \tag{4.38}$$

If one wishes to formulate an approximate prediction for the capacitance at arbitrary values of screening radius, including values of r_s that are comparable to b, then one may evaluate separately the capacitance based on approach (i), where the 2D pore thickness is renormalized as $d \to d_{\text{eff}}$, and approach (ii), where ions interact three-dimensionally, and then take the smaller value. Since intra- and inter- pore interactions contribute additively to the total energy, these create series contributions to the capacitance, so that as a zero-order approximation one can take the smaller of the two capacitances. The result of this process is shown in Fig. 4.9, which constitutes a prediction for the volumetric capacitance $\mathbb{C}$ at arbitrary voltage and electrode screening radius.

4.5 Nonlinear screening in graphite (carbon) supercapacitors

The preceding sections outline a general theory for the volumetric capacitance of a supercapacitor made with electrodes that can either be considered metallic or can be characterized by some linear screening radius r_s. In this section we discuss specifically the case of graphite electrodes, which is among the most commonly-studied materials for supercapacitor devices [11, 90, 92, 96].

In graphite, the Fermi level density of states $\nu(\mu_F)$ is actually relatively small, so that the linear screening radius $r_s \approx 0.8$ nm cannot be considered much smaller

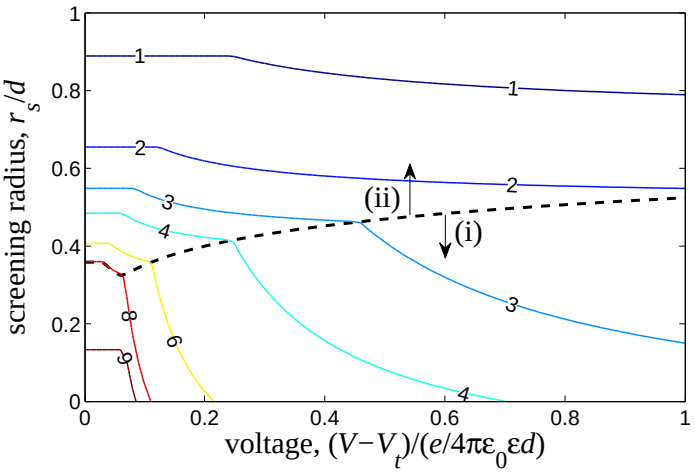

Figure 4.9: A contour plot of the volumetric capacitance $\mathbb{C}$ as a function of voltage V and electrode screening radius r_s for charges in an electrode with planar pores of width d separated by walls of thickness $b = d$ at room temperature. Contours are labeled by their values of $\mathbb{C}$ in units of $\varepsilon_0\varepsilon/d^2$. The dashed line separates the regions of validity of the two theories presented in this section: (i) where pores are non-interacting and the pore width can be renormalized according to $d \to d_{\text{eff}} = d + 2r_s$ (lower region), and (ii) where charges interact three dimensionally with the interaction law of Eq. (4.22) (upper region). For $\varepsilon = 2$ and $d = 1$ nm, the unit of volumetric capacitance $\varepsilon_0\varepsilon/d^2 = 18$ F/cm^3 and the unit of voltage $e/4\pi\varepsilon_0\varepsilon d = 0.7$ Volts.

than the spacing between pores [109]. For example, if $d = b = 1$ nm, then Fig. 4.9 would seem to imply a capacitance on the order of $\varepsilon_0\varepsilon/d^2 \approx 18$ F/cm^3. Experiments with graphite electrodes, however, yield a capacitance five times larger than this value [11, 92], suggesting that graphite screens over a much smaller distance than r_s and effectively behaves as a good metal.

This apparent discrepancy can be resolved if one recalls that the density of states in graphite is close to $\nu(\mu_F)$ only in a narrow range of energies, beyond which it increases linearly with energy on both sides of the Fermi level [109]. Such variation of the density of states suggests that screening by graphite is *non-linear* even when a relatively small electric field is applied to the surface of the pore, and that therefore the screening properties of the electrode material cannot be characterized by a constant linear screening radius r_s.

In order to estimate the distance over which the ions' potential is screened, one can consider the problem of a uniform applied electric field $\vec{E}_0$ orthogonal to the basal plane of graphite. It has been shown [110] that in this case the magnitude of the electric field $E(z)$ decays with the distance z beyond the graphite interface as

$$E(z) = \frac{E_0}{(1 + z/2z_0)^3}, \tag{4.39}$$

where

$$z_0 = \frac{\sqrt[3]{3}}{2} c \left(\frac{e}{4\pi\varepsilon_0 \varepsilon \alpha^2 c^2 E_0} \right)^{1/3} \tag{4.40}$$

is the centroid location of the counter-charge in the graphite (the non-linear screening radius), $c \approx 0.34$ nm is the distance between graphite planes (graphene sheets), and $\alpha \approx 2.2/\varepsilon$ is the effective fine structure constant of graphene. (See also recent discussions of screening in graphene multilayers in Refs. [111, 112]).

The implications of this result for the problem of screening of adsorbed ions in a graphite pore can be seen as follows. When the area density of ions inside a pore is large enough that $na^2 \simeq 1$, these ions can be said to produce a roughly uniform electric field at the wall of the pore whose strength is $E_0 \simeq e/2\varepsilon_0 \varepsilon a^2$. Inserting this relation into Eq. (4.40) yields a screening distance $z_0 \simeq 0.75c$, which suggests that the field is entirely screened within the first graphene layer. In other words, at dense ion filling the electric field between ions in the pore does not penetrate beyond the first graphene layer. Therefore, despite its relatively low density of states $\nu(\mu_F)$, graphite may be treated as a metal at not-too-small ion densities $na^2 \gtrsim 0.5$ (note that $na^2 > 0.5$ occupies the majority of the voltage range in Fig. 4.3).

We can also discuss what happens with the volumetric capacitance when the density of ions is smaller ($V - V_t$ decreases), so that the electric field E_0 produced by the ions becomes weaker. When $V - V_t$ is made moderately small, the effective density of states decreases, the nonlinear screening radius z_0 grows, and the nonlinear capacitance decreases. One can show using Eq. (4.40) that the capacitance $C \propto (V - V_t)^{1/2}$. Eventually, at larger $V - V_t$, the effective density of states saturates at the level of $\nu(\mu_F)$, so that the screening radius becomes constant and equal to the linear screening radius $r_s \approx 0.8$ nm. In this limit, the volumetric capacitance is relatively small and is given by the theory of Sec. 4.4, as was already discussed in the beginning of this section.

It is important to note that the discussion of this section has focused on the case where pores in the graphite electrode are *pre-prepared*, so that ions enter the pores individually. For many graphite- or graphene-based supercapacitors, however, there are no such pores, and instead the space between adjacent graphene planes is forcibly opened to accommodate ions when a sufficiently large voltage is applied. This process requires a large elastic energy associated with the deformation of the electrode around the intercalated ions. Such a high elastic energy cost can in fact be shared by a number of closely-spaced ions, so that as a result ions enter the electrode cooperatively as a bunch. This cooperative behavior dramatically modifies the C–V relationship and allows for a large maximum value of capacitance that persists even in the limit of vanishing electron density of states $\nu(\mu_F)$. A theory of the capacitance in such devices is presented in the next chapter.

4.6 Capacitance of a crystalline assembly of metallic spheres

So far we have restricted our discussion to the electrode geometry shown in Fig. 4.1. In practice, such electrodes with parallel planar pores are difficult to make. In many cases supercapacitor electrodes are simply a random assembly of conducting particles, arranged so that the particles form an infinite, conducting cluster through which electrons can percolate while the pores in this cluster form a separate percolating space through which the ionic liquid can freely pass. For such cases the model of Fig. 4.1 is a strong idealization. In this section we would like to briefly discuss another idealized electrode structure which captures the three-dimensional character of pores.

Consider an assembly of metallic nanospheres, each with the same radius R, arranged so that they form a cubic lattice with nearest neighbor spheres touching each other. As in previous sections, we imagine that this crystalline film is deposited onto a metallic contact plate, connected to a voltage source, and immersed in an ionic liquid. A voltage V is applied between the contact plate and the bulk of the ionic liquid. If the diameter of the ions within the ionic liquid is small enough, then this arrangement produces an effective supercapacitor electrode, where ions may percolate through the spaces between conducting spheres and neutralize the electronic charge provided by the voltage source.

In order to calculate the capacitance of this electrode, we first analyze the interaction between two ions that enter into the bulk of the electrode. This can be done by calculating the potential as a function of distance produced by a single ion in the center of a pore deep inside the electrode bulk. We calculate this potential numerically using the relaxation method for solving the Laplace equation, where each of the conducting spheres is held at zero potential. We find that potential decays exponentially with radial distance from the ion with a characteristic screening length $R_s = R \times (0.26 \pm 0.01)$. The reason for this sharp decay is the same as for the decay of the potential in 2D, slit-like pores [Eq. (4.5)]: electric field lines emanating from the ion are adsorbed by the surface of nearby conducting spheres, and the number of these field lines that survive by passing through the narrow, tortuous pores between spheres decays exponentially with distance.

Once the interaction law is known, one can calculate the capacitance in a way similar to the analysis of Sec. 4.4. We arrive then at a relation $C(V)$ which has the maximum given by Eq. (4.38). For $R = 4$ nm, $T = 300$ K, and $\varepsilon = 2$ this relation gives a volumetric capacitance $\mathbb{C}_{max} = 1.7\varepsilon_0\varepsilon/R_s^2 = 25\varepsilon_0\varepsilon/R^2 \approx 28$ F/cm^3. Remarkably, in this arrangement the capacitance per sphere is roughly 16 times larger than the capacitance of a single, isolated sphere in a medium with dielectric constant ε.

One can reach even larger volumetric capacitance if the spheres are densely packed rather than arranged in a cubic lattice. Reducing the radius R of the spheres also sharply increases the capacitance.

Chapter 5

Capacitance of a graphene supercapacitor

5.1 Introduction

In the previous chapter we derived a theory of volumetric capacitance in supercapacitor devices, where energy is stored through the reversible absorption of ions into the volume of a porous, charged electrode. We showed that when the electrode is a good conductor the strong screening of discrete ionic charges by the electrode allows the capacitance to be large. On the other hand, for an electrode made from a poorly-conducting material, there is no *a priori* reason to expect large capacitance. If one were to repeat the arguments of Ch. 4 for an electrode with vanishingly small Fermi level density of states $\nu(\mu_F)$, one might arrive at the conclusion that ionic charges are poorly screened and therefore there is no enhancement of the capacitance above the relatively low mean-field value. Indeed, a naïve application of formulas (4.21), (4.25), and (4.32) would suggest that for $\nu(\mu_F) \to 0$ the linear screening radius $r_s \to \infty$ and therefore the capacitance collapses to zero. More realistically, one might expect that the capacitance should not exceed the values predicted by the mean-field description.

It is somewhat surprising, then, that EDLC devices with very large capacitance can be made from graphene. The Dirac-like dispersion relation of electrons in undoped graphene implies a vanishing Fermi level density of states, so that one would expect graphene to screen ionic charges only very weakly. Nonetheless, experiments

on graphene-based EDLCs generally report capacitance on the order of a few hundred F/cm^3 (see Ref. [113] and references therein), a value which is too large to be explained by simple mean-field descriptions. In this chapter we consider such graphene-based supercapacitors and show that, indeed, their capacitance can be much larger than would be predicted by mean-field theories. As suggested in Sec. 4.5, this behavior can be understood as a result of the strong *non-linear* screening properties of layered graphene and the cooperative entrance of ion bunches into the electrode.

The remainder of this chapter is organized as follows. In Sec. 5.2 we discuss experimental realizations of graphene-based supercapacitors and define the system to be studied. Sec. 5.3 presents the mean-field prediction for the capacitance of a graphene stack. Sec. 5.4 presents an alternate prediction, based on the known "staging" behavior of graphite intercalation compounds. In Sec. 5.5 a picture is presented that reconciles these two opposing theories; the discussion of Sec. 5.5 can be considered a summary of the main results of this chapter. In Sec. 5.6 a general theory for the capacitance is developed at arbitrary values of the fine structure constant α, and a wealth of different scaling behaviors are uncovered. We conclude in Sec. 5.8 with a discussion of our results and their implication for the development of graphene supercapacitors.

5.2 Graphene-based supercapacitor electrodes

Over the past few years, graphene has become a popular topic of study as an electrode material for EDLC devices [11, 113, 114, 115, 116, 117, 118, 119] owing to its high electrical conductivity and large surface area. In such devices individual graphene layers are arranged in parallel stacks and placed in contact with a reservoir of ionic liquid or some other concentrated electrolyte solution. Most commonly, graphene layers are ordered in the transverse direction, but have random translations or rotations between adjacent layers ("turbostratic disorder"), so that on average the electronic dispersion relation of each graphene layer is unaltered. Below we refer to this arrangement as a "graphene stack" (GS). In practice, the layered ordering of graphene sheets within the GS electrode is preserved only over some mesoscopic length scale, usually on the order of tens of nanometers [11, 119]. In the remainder of this chapter we make the assumption that ordering of graphene planes within the electrode is preserved over arbitrarily large

distances. This assumption does not significantly affect any results, as demonstrated in Sec. 5.6.

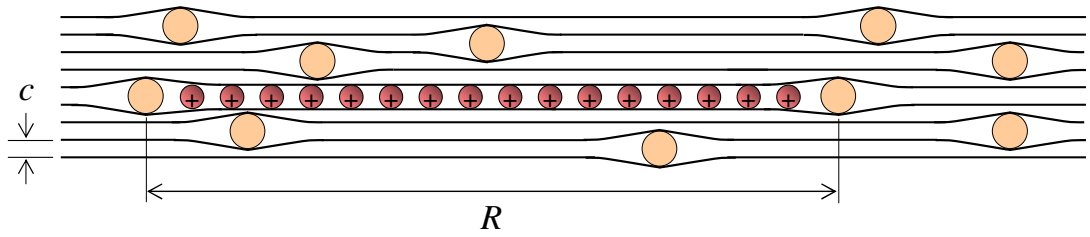

Figure 5.1: A schematic picture of a portion of the GS electrode, shown in a side view. The stack of graphene layers (black lines), arranged with a separation c between layers, has some density of "spacer" molecules (filled circles) in it. When a voltage is applied, ions (circles with +'s) enter the electrode collectively in the form of a disk whose size is determined by the average distance R between spacers.

A capacitor is formed from the GS by connecting it to a voltage source that maintains a constant electrochemical potential V between electrons in the GS and the bulk of the ionic liquid. The individual graphene sheets are in electrical contact with each other, so that the electrochemical potential of electrons with the GS is uniform. A functional EDLC device contains two such GS electrodes with a voltage applied between them, usually with a porous separator between the electrodes that isolates them from each electronically while allowing ions to flow from one electrode to the other. In this chapter we concern ourselves with the capacitance of a single GS electrode (say, the anode); the functional device consists of two such capacitances in series.

In the fabrication of EDLC electrodes, the effectiveness of the electrode is often limited by the strong binding of graphene sheets to each other through van der Waals (vdW) attraction [113, 115]. The short-ranged vdW interaction between sheets produces a large contact energy $\gamma = (1.5 \pm 0.4)$ eV/nm^2 [120], and in the absence of any modification to the graphene this interaction results in dense, graphite-like agglomerates whose interior surface area is not readily accessible to ions. In this case only a large applied voltage can induce ions to enter the electrode by forcibly separating the space between adjacent graphene sheets. This process is often too slow to meet the fast charging/discharging requirements of practical devices. Further, such agglomeration can require the device to operate at large voltages that are outside the limited

electrochemical stability window of the electrolyte.

Given these difficulties, it is often necessary to take steps during fabrication to reduce the strong binding between adjacent graphene sheets. One method of doing so is by fabricating electrodes from chemically modified graphene, in which graphene sheets are bonded to polymers or some other "spacer" molecule before being condensed into a stack similar to the one shown in Fig. 5.1. In this arrangement each spacer provides sufficient steric hindrance to separate adjacent graphene layers at a given point. Electrodes with such spacers have recently been constructed and shown to generate capacitance values in excess of 100 F/cm^3 even at relatively low voltages [115].

In the region surrounding each spacer, there is a competition between the attractive vdW energy between the two separated sheets and the elastic energy associated with bending them to bring them together. This competition results in regions of intense elastic stress surrounding each spacer. When a voltage is applied between the electrode and the ionic liquid, ions are induced to intercalate between graphene sheets in the GS. Since the diameter of the ions is also larger than the spacing c between adjacent graphene sheets (and is typically comparable to the size of the spacers), the intercalation of ions requires additional separation of graphene sheets. This separation occurs in a way that best relieves the elastic stress surrounding the spacers – namely, through the formation of filled "pockets" of ions rather than through the introduction of scattered, individual ions. The size of these pockets is defined by the average distance R between spacers.

One can explain the formation of these pockets of ions using the language of elastic energy-mediated attraction. When a single ion enters the GS, it creates a region of intense elastic stress around itself. If two such ions are introduced to the GS, they can reduce the total elastic energy of the system by approaching each other closely, so that together they share the elastic energy associated with deforming the GS around them. Thus, there is an effective attraction between ions in the GS mediated by the elastic strain they induce. This attraction has been observed experimentally in intercalation experiments [121] and has been described theoretically as an effective lateral attraction between intercalated ions [122, 123].

When there is some finite density of ions within the electrode, scattered ions between two adjacent sheets in the GS attract each other to form a large "disk" of ionic charge.

The 2D charge density σ of this disk is determined by the balance between the elastic energy-mediated attraction and the Coulomb repulsion between ions. The disk continues to grow until it reaches the size R, at which point its growth is truncated by the presence of spacer molecules, which are generally massive enough that they can be considered immobile on the time scales of charging/discharging of the electrode. The result is that, as a voltage is applied, the electrode is charged by the incremental addition of two-dimensional (2D) "disks" of ions that enter the electrode collectively. In our derivation of the capacitance below (Secs. 5.5 and 5.6), we assume that ionic charges indeed enter the electrode in the form of these charged disks with size R and uniform 2D charge density σ.

One may well notice that in the limit where there are no spacers at all in the GS, the electrode is simply turbostratic graphite. In this case $R \to \infty$, which suggests that ions enter the GS as infinite, uniform planes of ionic charge. In fact, this phenomenon is well-known: it is referred to as "staging" of graphite intercalation compounds and has been studied for more than eighty years [124]. In such compounds, guest ions such as Li^+, K^+, or Ca^{2+} are forcibly introduced into pure graphite by an applied voltage. In most cases, the elastic energy-mediated attraction between ions causes the intercalated ions to arrange themselves in an ordered sequence of filled and empty planes of ions, with each filled plane having some fixed 2D density of ions and the distance between filled planes varying with the overall density of intercalated ions. The number of graphene sheets between two subsequent filled layers is called the "stage" of the compound: low densities of intercalated ions corresponds to large stage, while the maximum filling of ions is called "stage 1". The density σ/e of ions in a filled plane is determined by the balance between their Coulomb repulsion and the elastic energy-mediated attraction, and therefore it depends in general on the ions' size: small ions tend to have stoichiometry XC_6 in their stage 1 form, while larger ions form less dense arrangements such as XC_8 or XC_{12} [125]. In each case, $\sigma/(e/c^2)$ is of order unity. The capacitance resulting from this staged intercalation is discussed in Sec. 5.4.

5.3 Mean-field predictions of capacitance in a graphene stack

As a first attempt at describing the capacitance of a GS, one could ignore the discrete, bunched nature of the ionic charge suggested in Sec. 5.2 and instead imagine that ions form uniform planes of charge. In this section we present the results of this mean-field picture. It will be shown in Secs. 5.5 and 5.6 that, surprisingly, the capacitance is actually parametrically larger than the mean-field prediction over a significant range of voltage. Here and in the remainder of this chapter, all formulas are approximate; we drop all numerical coefficients and focus instead on the parametric dependencies and ranges of behavior of the capacitance.

Consider, for example, the problem of the capacitance of a single graphene sheet gated by a flat, parallel metal electrode separated by a distance d from the sheet. In this problem there is no issue of charge discreteness, and the arrangement can be described as a parallel-plate capacitor with thickness d. The total energy $\mathscr{U}$ per unit area of this capacitor can be written as $\mathscr{U} = \mathscr{U}_{el} + \mathscr{U}_k$, where $\mathscr{U}_{el}$ is the electrostatic energy and $\mathscr{U}_k$ is the quantum kinetic energy of electrons within the graphene.

The electrostatic energy $\mathscr{U}_{el}$ is equivalent to that of a standard parallel plate capacitor,

$$\mathscr{U}_{el} \sim \mathscr{Q}^2 d/\varepsilon_0 \varepsilon, \tag{5.1}$$

where $\mathscr{Q}$ is the charge of the capacitor per unit area, ε_0 is the vacuum permittivity and ε is the static dielectric constant. The quantum kinetic energy per unit area

$$\mathscr{U}_k \sim \epsilon_g(n) n, \tag{5.2}$$

where

$$\epsilon_g(n) \sim \hbar v_g \sqrt{n} \tag{5.3}$$

is the Fermi energy of undoped graphene with a 2D concentration $n = \mathscr{Q}/e$ of electrons and $v_g \approx 10^6$ m/s is the Fermi velocity in graphene. $\mathscr{U}_k$ can be written in terms of $\mathscr{Q}$ as

$$\mathscr{U}_k \sim \frac{\sqrt{e\mathscr{Q}^3}}{\alpha \varepsilon_0 \varepsilon}, \tag{5.4}$$

where $\alpha \sim e^2/\varepsilon_0 \varepsilon \hbar v_g \lesssim 1$ is the effective fine structure constant of graphene.

Eqs. (5.1) and (5.4) imply that when the charge of the capacitor is small enough that $\mathscr{Q} \ll e/\alpha^2 d^2$, the quantum kinetic energy $\mathscr{U}_k \gg \mathscr{U}_{el}$, and so $\mathscr{U} \sim \mathscr{U}_k$. Conversely, at $\mathscr{Q} \gg e/\alpha^2 d^2$ we have $\mathscr{U} \sim \mathscr{U}_{el}$. Using the thermodynamic relations between the total energy $\mathscr{U}$ and the capacitor voltage V and capacitance per unit area $\mathscr{C}$, as defined by Eqs. (2.5) and (2.6), gives the following mean-field prediction:

$$\mathscr{C}(V) \sim \begin{cases} (\varepsilon_0 \varepsilon \alpha)^2 V/e & , \quad V \ll e/\alpha^2 \varepsilon_0 \varepsilon d \\ \varepsilon_0 \varepsilon / d & , \quad V \gg e/\alpha^2 \varepsilon_0 \varepsilon d \end{cases} \tag{5.5}$$

The low voltage result in Eq. (5.5), $C \propto \alpha^2 V$, is often referred to as the "quantum capacitance" of graphene. It has been accurately observed for systems where a single sheet of graphene is gated by a metal electrode [44] or an ionic liquid [42].

For a stack of many graphene sheets, one can try to extend the result of Eq. (5.5) by imagining that the GS consists of many such parallel plate capacitors, each of thickness $d \sim c$, connected in parallel. This is equivalent to assuming that the ionic charge consists of a series of uniformly charged planes located at the midplane between every adjacent pair of graphene sheets. Multiplying the result of Eq. (5.5) by the number of graphene sheets per unit distance, $1/c$, gives for the "quantum capacitance" per unit volume

$$\mathbb{C}(V) \sim \alpha^2 \frac{V - V_t}{e/\varepsilon_0 \varepsilon c} \frac{\varepsilon_0 \varepsilon}{c^2}, \tag{5.6}$$

where eV_t is the energy required to bring a single ion from the external ionic liquid reservoir to the interior of the GS. We refer to V_t as the "threshold voltage"; it is the voltage at which the capacitor has zero charge. The value of V_t depends in general on the chemical potential of ions in the ionic liquid.

In the remainder of this chapter we employ dimensionless variables, defined so that the quantities e, $\varepsilon_0 \varepsilon$, and c are all set to unity. In other words, all energies are in units of $e^2/\varepsilon_0 \varepsilon c$, all distances are in units of c, and the volumetric capacitance is in units of $\varepsilon_0 \varepsilon / c^2$. Dimensionless variables are indicated with a bar superscript. The symbol $\bar{V}$ is used to denote the dimensionless voltage relative to the threshold value, $\bar{V} \equiv (V - V_t)/(e/\varepsilon_0 \varepsilon c)$. In these units Eq. (5.6) takes the compact form

$$\bar{\mathbb{C}}(\bar{V}) \sim \alpha^2 \bar{V}. \tag{5.7}$$

It should be noted that for a real GS, the large voltage regime of Eq. 5.5, where the capacitance plateaus at a constant value $\bar{\mathbb{C}} \sim 1$, is not generally accessible, since this

implies a volume density of ions that is larger than $1/c^3$. Since the ion size is typically larger than c, this high density of ions does not fit sterically within the electrode and the capacitance should collapse at $\bar{V} \gg 1/\alpha$ (and therefore also at $\bar{V} \gg 1/\alpha^2 \gtrsim 1/\alpha$) since no further capacitor charging is possible. We can therefore conclude that in the relevant range of voltage the mean-field approach outlined in this section predicts a capacitance equal to that of Eq. (5.7).

5.4 Capacitance of staged graphite

The mean-field picture of the previous section, wherein it is assumed that each graphene sheet forms a parallel plate capacitor with an adjacent layer of ions, is apparently incompatible with the phenomenon of staging in graphite intercalation compounds that is described in Sec. 5.2. Indeed, in staged graphite ions do not intercalate uniformly into all interstitial spaces between graphene sheets. Rather, the ions form a correlated arrangement of filled and empty planes.

To understand how this staged structure affects the capacitance, one can first consider the problem of the potential ϕ surrounding a single, infinite charged plane with (dimensionless) charge density $\bar{\sigma}$ in an otherwise empty GS. This problem was first solved in Ref. [110]; the solution is briefly repeated here. Since in this problem there is no variation of the potential in the direction parallel to the graphene sheets, one can calculate the potential everywhere using the Thomas-Fermi (T-F) approximation: $\bar{\phi}(\bar{z}) = \bar{\epsilon}_g(\bar{n}(\bar{z}))$, where $\bar{z}$ is the (dimensionless) distance from the charged plane. Inserting the graphene dispersion relation [Eq. (5.3)] and invoking the Poisson equation $\bar{\nabla}^2\bar{\phi} = \bar{n}$ gives the T-F relation for the potential:

$$\bar{\nabla}^2\bar{\phi} \sim \alpha^2\bar{\phi}^2. \tag{5.8}$$

Making use of the boundary condition $(d\bar{\phi}/d\bar{z})|_{\bar{z}=0} \sim \bar{\sigma}$ imposed by Gauss's law, one can solve Eq. (5.8) to find

$$\bar{\phi}(\bar{z}) \sim \frac{1}{\alpha^2(\bar{z} + \bar{z}_0)^2}, \tag{5.9}$$

where $\bar{z}_0$ is the characteristic distance over which the potential decays, given by

$$\bar{z}_0 \sim \frac{1}{\alpha^{2/3}\bar{\sigma}^{1/3}}. \tag{5.10}$$

The length scale z_0 can be thought of as the characteristic size of the plane's screening atmosphere of neutralizing electrons.

When two such infinite planes of charge are separated by a finite distance h in the GS, there is a repulsive interaction between them. The interaction energy per unit area between these planes, $u(h)$, has been derived previously [123] and shown to be proportional to $1/h^5$. This relation can be understood via the following argument.

When the separation h between the planes is finite, the planes' screening atmospheres overlap, and this overlap produces a repulsive pressure P between them. The value of the pressure can be found by considering the midplane between the two charged planes, at which the electric field is zero by symmetry. Since the electric field is zero, the pressure at the midplane is entirely determined by the kinetic energy density of electrons,[1] which is given by $\bar{P} \sim \bar{n}_m^{3/2}/\alpha$, where $\bar{n}_m$ is the (dimensionless) 2D electron density at the midplane. When h/z_0 is moderately large, one can estimate that the electron density at any given point between the planes is roughly equal to the sum of the electron densities created by each plane in isolation. This gives an estimate for the repulsive pressure $P(h)$ which can be integrated to find the total repulsive energy per unit area: $u(h) = \int_h^\infty P(h')dh'$, which gives $\bar{u}(\bar{h}) \sim 1/(\alpha^4 \bar{h}^5)$.

From this interaction law, one can derive a relation for the capacitance of staged intercalation compounds. Namely, when the GS electrode has some charge $\mathbb{Q}$ per unit volume, the (dimensionless) spacing between charged planes is $\bar{h} \sim \bar{\sigma}/\bar{\mathbb{Q}}$. At $h \gg z_0$, the total interaction energy per unit volume is dominated by nearest-neighbor interactions between planes, and is therefore equal to $\bar{\mathbb{U}} \sim \bar{u}(\bar{h})/\bar{h} \sim \bar{\mathbb{Q}}^6/\alpha^4\bar{\sigma}^6$. Using the thermodynamic relations for capacitance and voltage [Eqs. (4.26) and (4.27)] gives

$$\bar{\mathbb{C}}(\bar{V}) \sim \frac{\alpha^{4/5}\bar{\sigma}^{6/5}}{\bar{V}^{4/5}}. \tag{5.11}$$

This relationship for $\mathbb{C}(V)$ is markedly different from the mean-field quantum capacitance of Eq. (5.7). Most strikingly, it *diverges* at small voltage rather than collapsing to zero. In fact, the "staging capacitance" of Eq. (5.11) remains parametrically larger than that of Eq. (5.7) up until $\bar{V} \sim 1$, which is at the limit of steric filling of the electrode.

[1] This argument is similar to the one used to evaluate the repulsive pressure between two charged planes in an aqueous electrolyte solution, where repulsive forces result from the confinement entropy of the counterions [126].

5.5 Main results for $\alpha \sim 1$

For the main problem of this chapter, as defined in Sec. 5.2, the vastly different results of Eq. (5.7) and Eq. (5.11) present something of a puzzle. One the one hand, when the spacers in the GS electrode are plentiful, the graphene sheets are fully separated and ions are free to enter the GS individually and fill its volume uniformly. In this case, the capacitance should be similar to the mean-field result of Eq. (5.7). On the other hand, when the spacers in the GS are sparse, the intercalating ionic charges arrange themselves in the staged structure discussed in Sec. 5.4 and the capacitance should follow the prediction of Eq. (5.11). The central problem of this chapter is how the capacitance should behave when the density of spacers is finite. In this case, ionic charge enters the GS in the form of disks with finite size R, and there should be a crossover between the two regimes of behavior. However, since Eqs. (5.7) and (5.11) do not meet anywhere except at the steric limit $\bar{V} \sim 1$, it is not obvious how this crossover can occur.

In this section we briefly explain how this puzzle can be resolved. For the purpose of this brief discussion we focus on the most experimentally-relevant case where $\alpha \sim 1$ and $\bar{\sigma} \sim 1$. The dimensionless radius $\bar{R}$ can therefore be thought of as the square root of the number of ions within each disk. A more thorough derivation of the capacitance is given in Sec. 5.6, and includes a discussion of additional regimes of behavior that appear when α is a small parameter.

The essence of our resolution to the problem is that when disks of charge enter the GS, each disk draws around itself a strongly-bound, nonlinear screening atmosphere of electrons that *renormalizes* the disk's effective charge. To see how this happens, consider first the case where a single disk of charge is introduced into the GS.

At very small distances z from the surface of the disk, the disk behaves like an infinite plane and the electric potential can be described by Eq. (5.15). This formula for the potential is derived under the T-F approximation, which neglects any quantum effects associated with finite electron wavelength, and therefore its applicability is limited to regions where the Fermi wavelength λ_F is much smaller than the length scale over which the potential is varying in the transverse direction. Thus, to find the distance z_{TF} at which T-F screening ends, one can equate $\bar{\lambda}_F \sim 1/\sqrt{\bar{n}} \sim 1/(\bar{\phi})$ to the disk size R, which

gives

$$\bar{z}_{TF} \sim \sqrt{\bar{R}}. \tag{5.12}$$

Since $z_{TF} \ll R$, the region over which the T-F approximation is applicable can be described as a disk-shaped volume with some thickness $z_{TF} \ll R$ and width $\sim R$. For larger z the T-F approximation fails, and the potential can instead by described by linear screening.

The net effect of the strong, T-F screening at $|z| < z_{TF}$ is to renormalize the disk's charge. To see the extent of this renormalization, one can calculate the charge enclosed within the region $|z| < z_{TF}$. In this case Gauss's law can be written as $\bar{q} \sim -\bar{R}^2(d\bar{\phi}/d\bar{z})|_{\bar{z}=\bar{z}_{TF}}$, which gives $\bar{q} \sim \sqrt{\bar{R}}$. This charge q enclosed within the T-F region is much smaller than the bare disk charge σR^2.

Outside of the T-F region, the potential created by the reduced charge q is not strongly screened. Indeed, at these large distances the potential is affected only by the relatively weak dielectric response of graphene layers with vanishing Fermi level density of states. Such linear screening is described in detail in Sec. 5.7.1. For the purpose of later calculations of the capacitance, however, it is sufficient to think that outside of the T-F region there is no screening of the disk charge. Instead, the remaining negative charge $-q$ required to make the system electroneutral is essentially distributed uniformly throughout the available volume of the electrode.

We can now consider what happens when there is some finite concentration N of these charge-renormalized disks within the volume of the electrode. When the density of the disks is low enough that $N \ll 1/(R^2 z_{TF})$, the disks are well-separated from each other and their nonlinear screening atmospheres do not overlap. One can think, then, that in this low density limit the capacitor charge consists of a dilute gas of disks with volume density N and effective charge q neutralized by a uniform background of electronic charge with charge density $-qN$.

In this configuration, the total capacitor energy U has three components: the self-energy of the disks with effective charge q, the electrostatic energy U_{el} associated with the Coulomb interaction between the disks and the uniform background, and the quantum kinetic energy U_k of the uniform, neutralizing electronic charge. The self-energy component affects only the threshold voltage V_t, and we absorb it into the dimensionless

voltage $\bar{V}$, as described in Sec. 5.3. The Coulomb energy U_{el} is much smaller in magnitude than U_k in the limit $N \ll 1/(R^2 z_{TF})$; this is shown explicitly in Sec. 5.7.2. Thus, in the regime where the disks' screening atmospheres do not overlap, the capacitance is dominated by the quantum kinetic energy of the uniform electronic charge.

The quantum kinetic energy $_k$ can be derived in a way that is similar to the derivation of Eq. (5.4). Here, the 2D electron density in each graphene sheet (in regions outside the T-F screening atmospheres of each disk) is given by $n = qNc/e$. Using $q \sim \sqrt{\bar{R}}$ and the expression of Eq. (5.2) gives for the (dimensionless) energy per unit volume $\bar{\mathbb{U}}_k \sim \bar{N}^{3/2}\bar{R}^{3/4}$. Since N is related to the total capacitor charge per unit volume by $\mathbb{Q} = \sigma R^2 N$, one can use the thermodynamic relations for capacitance and voltage in Eqs. (4.26) and (4.27) to get

$$\bar{\mathbb{C}}(\bar{V}) \sim \bar{R}^{9/2}\bar{V}, \qquad (\bar{V} \ll 1/\bar{R}^{5/2}). \tag{5.13}$$

Corrections to this result associated with the Coulomb energy are discussed in Appendix 5.7.2.

In Eq. (5.13) one can see the strong effect of the renormalization of the disk charge. This equation is similar the mean-field relation of Eq. (5.7) in that both give $C \propto V$, but Eq. (5.13) has a significantly larger coefficient. Indeed, the slope of the C–V relation in Eq. (5.13) is larger than that of the mean-field result by a factor $\bar{R}^{9/2} \gg 1$. This large enhancement of the capacitance can be viewed as a direct result of the nonlinear screening of each disk. That is, the strong T-F screening atmosphere surrounding each disk greatly reduces the uniform electron concentration in the electrode for a given capacitor charge $\mathbb{Q}$ and therefore leads to a smaller quantum kinetic energy cost for capacitor charging.

When the capacitor charge is made larger, such that the density of disks $N \gg 1/(R^2 z_{TF})$, the nonlinear screening atmospheres of adjacent disks overlap, and one can no longer talk about a uniform electron charge $-qN$ filling the space between disks. Instead, the capacitance is dominated by the repulsive interaction between neighboring disks, and the capacitance is described by the staging theory of Eq. 5.11:

$$\bar{\mathbb{C}}(\bar{V}) \sim 1/\bar{V}^{4/5}, \qquad (V \gg 1/\bar{R}^{5/2}). \tag{5.14}$$

The resulting C–V relation is shown schematically in Fig. 5.2.

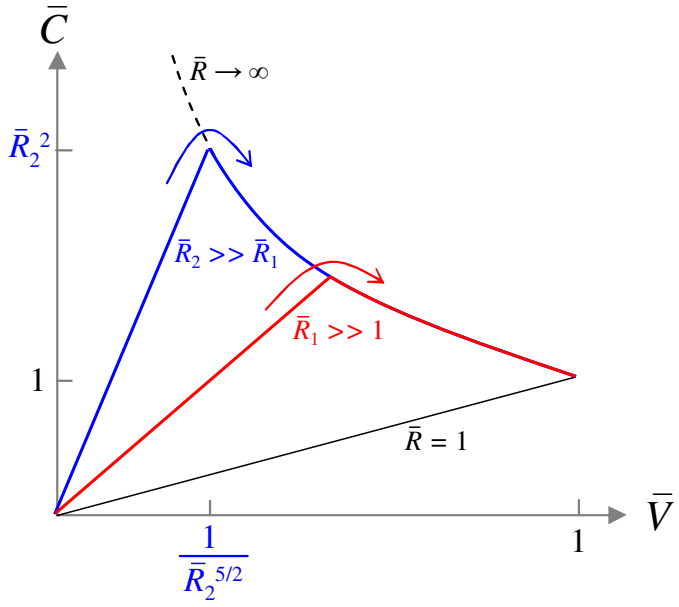

Figure 5.2: A schematic picture of the capacitance as a function of voltage for $\alpha \sim 1$ and $\bar{\sigma} \sim 1$ at different values of the disk size R. At $\bar{R} = 1$, the GS is filled by individual ions and the capacitance collapses to the mean-field result of Eq. (5.7) (thin, black line). At $R \to \infty$, ions enter the GS in stages and the capacitance follows the result of Eq. (5.11) (dashed curve). The behavior for finite R is shown by the red and blue thick lines for two different values of R_1 and R_2 (red/blue thick curves).

In this way the puzzle of the crossover between Eqs. (5.7) and (5.11) is resolved. At low voltages, one can still think that the result $C \propto V$ is a consequence of uniformly raising the electron Fermi level throughout the GS in order to provide a neutralizing electron concentration. However, this neutralizing concentration should be thought of as a compensation not to the *total* ionic charge but to the much smaller *renormalized* ionic charge. It is this renormalization that allows the capacitance to be large and produces a smooth crossover to the behavior $C \propto V^{-4/5}$ associated with staging.

5.6 General results for $\alpha < 1$

In the previous section we presented results for the capacitance, focusing on the special case $\alpha, \bar{\sigma} \sim 1$. In this section we calculate the capacitance as a general function of voltage and σ, examining different cases for the value of the fine structure constant α.

In traditional quantum electrodynamics problems, the fine structure constant $\alpha_{QED} \approx 1/137$ is a small parameter. For graphene, on the other hand, the fine structure constant $\alpha \approx 2.2/\varepsilon$ is usually of order unity. Nonetheless, our theory below considers α as an arbitrary small parameter whose value is between 0 and 1. In this way we illustrate the full range of screening behaviors that are in principle present in graphene, and we highlight the aspects of the problem that are interesting from a fundamental physics standpoint.

5.6.1 Screening of a disk of charge in a graphene stack

As discussed in Sec. 5.2, when a voltage is applied between the GS and the external ionic liquid reservoir, ions intercalate into the GS in the form of discrete disks with size R and charge density σ. The capacitance $C(V)$ of the electrode is determined by the mutual repulsion of these disks. This repulsion depends in general on the nature of the screening atmosphere surrounding each disk. Sec. 5.5 discussed this screening atmosphere for the case $\alpha \sim 1$. In this section, before proceeding to calculate the capacitance, we first discuss the screening of a single disk for general values of α.

When a single disk is introduced into the GS, it draws a neutralizing concentration of electrons into the graphene layers surrounding it. The distance over which these neutralizing electrons are distributed depends on the value of the fine structure constant α. The case of very large α, for example, corresponds to the classical limit $\hbar \to 0$, where electrons can be accumulated at arbitrarily large densities with vanishingly small quantum kinetic energy cost. Thus, at large α each disk of charge is screened effectively over a fairly short distance: electronic charge can freely coalesce to the surface of the disk and screen it entirely. Conversely, at small α the screening of a single disk is poor and occurs over a large distance.

To understand more precisely how the disk is screened, one can first solve for the electric potential surrounding the disk in the T-F approximation, $\bar{\nabla}^2\bar{\phi} \sim \alpha^2\bar{\phi}^2$, as was done for the case of $R \to \infty$ in Sec. 5.4. The resulting potential has a simple expression in two limiting cases: the "infinite plane" limit, where $\rho, z \ll R$, and the "point charge" limit, where $\rho^2 + z^2 \ll R^2$. In the former case the potential depends only on the z

coordinate:

$$\bar{\phi}(\bar{z}) \sim \frac{1}{\alpha^2(\bar{z}+\bar{z}_0)^2}, \quad (\rho, z \ll R) \tag{5.15}$$

as in Eq. (5.9). In the latter case, the potential is spherically symmetric:

$$\bar{\phi}(\bar{\rho}, \bar{z}) \sim \frac{1}{\alpha^2(\bar{\rho}^2+\bar{z}^2)}, \quad (\rho^2 + z^2 \gg R) \tag{5.16}$$

The applicability of formulas (5.15) and (5.16) is limited to regions where the Fermi wavelength $\bar{\lambda}_F \sim 1/\sqrt{\bar{n}}$ is much smaller than the length scale over which the potential is varying in the ρ direction. The distance at which the T-F approximation becomes invalid depends in general on the value of α.

In fact, one can discuss four ranges of α, each with a distinct screening behavior. The screening over each of these ranges is summarized schematically in Fig. 5.3. In each range, the screening is characterized by the distance over which T-F screening is applicable, denoted z_{TF} or r_{TF}, the characteristic decay length of the potential, z_0 or r_0, and the total charge q enclosed within the range of T-F screening. The following subsections discuss each range individually, beginning with the largest value of α.

$\alpha \gg 1/\bar{R}$

When α is large enough that $\alpha \gg 1/\bar{R}$, the screening atmosphere surrounding each disk is similar to the case described in Sec. 5.5 for $\alpha \sim 1$. That is, the region over which the T-F approximation is applicable can be described as a disk-shaped volume with some thickness

$$\bar{z}_{TF} \sim \sqrt{\bar{R}/\alpha} \ll \bar{R} \tag{5.17}$$

and width $\sim R$. The net effect of the strong, T-F screening at $z < z_{TF}$ is to produce a renormalized disk charge $\bar{q} \sim -\bar{R}^2(d\bar{\phi}/d\bar{z})|_{\bar{z}=\bar{z}_{TF}} \sim \sqrt{\bar{R}/\alpha}$, which is much smaller than the bare disk charge σR^2. Outside of the T-F region, the reduced charge q creates a relatively weakly-varying potential that is described by linear response theory. This situation is shown schematically in Fig. 5.3a.

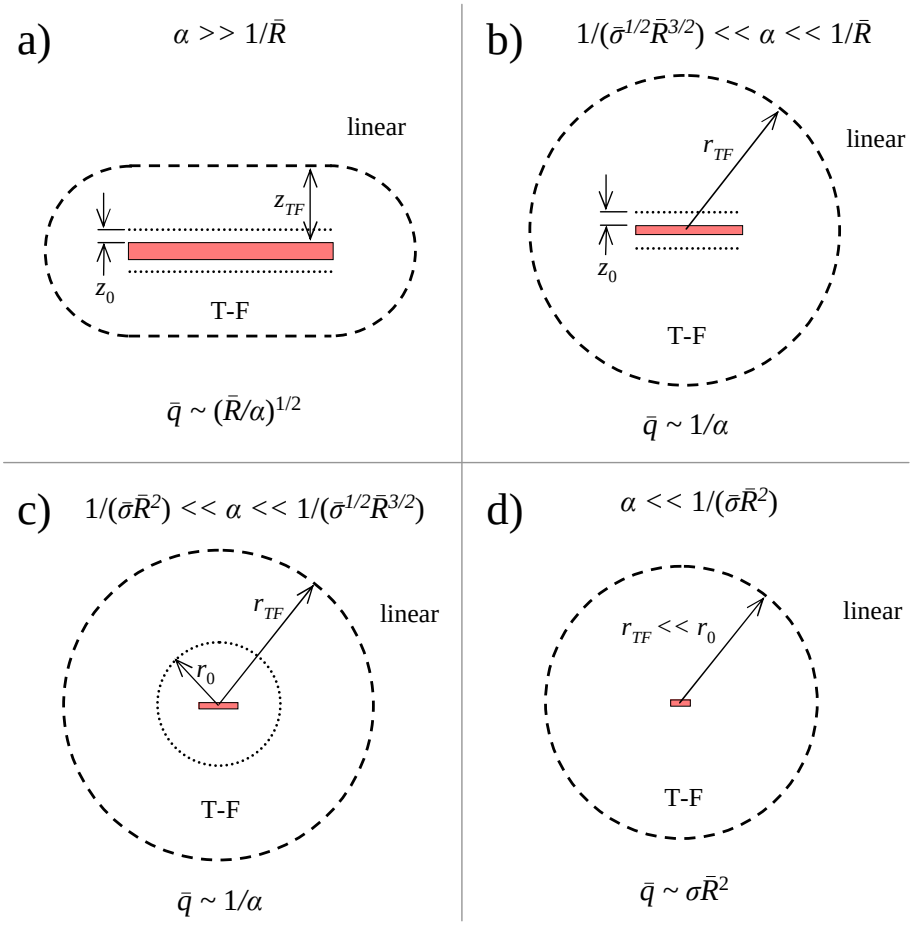

Figure 5.3: A schematic summary of screening of the disk of ionic charge (rectangle) in different ranges of α (quadrants a, b, c, d). Each quadrant is labeled by its corresponding range of α (top) and by the renormalized charge $\bar{q}$ of the disk (bottom). The limit of T-F screening is shown for each regime by a dashed line, and the characteristic decay length of the nonlinear potential is shown as a dotted line. In each picture the disk has the same size R; one can say that the pictures a – d have progressively larger scale.

$1/(\bar{\sigma}^{1/2}\bar{R}^{3/2}) \ll \alpha \ll 1/\bar{R}$

When α is small enough that $\alpha \ll 1/\bar{R}$, the distance z_{TF} calculated in Sec. 5.6.1 becomes much larger than R. This implies that at the limit of T-F screening the potential becomes spherically symmetric, as described by Eq. (5.16), so that the region

over which T-F screening is applicable is a sphere with radius r_{TF}. When α is still large enough that $\alpha \gg 1/(\bar{\sigma}^{1/2}\bar{R}^{3/2})$, however, the potential still decays rapidly at short distances $z \sim z_0 \ll R$ from the electrode, which implies that the majority of the screening charge resides within a surface layer with thickness $z_0 \ll R$ at the sides of the disk. This situation is shown schematically in Fig. 5.3b.

The value of r_{TF} can be found by setting the Fermi wavelength λ_F equal to the size r_{TF} of the T-F region. This procedure gives

$$\bar{r}_{TF} \sim \frac{1}{\alpha} \gg \bar{R}. \tag{5.18}$$

The total charge q within the T-F region can be found by Gauss's law, as in the previous case, and is equal to $\bar{q} \sim 1/\alpha$.

$1/(\bar{\sigma}\bar{R}^2) \ll \alpha \ll 1/(\bar{\sigma}^{1/2}\bar{R}^{3/2})$

If α is reduced even further, so that $\alpha \ll 1/(\bar{\sigma}^{1/2}\bar{R}^{3/2})$, the distance z_0 becomes much larger than R. This implies that the potential is roughly constant at distances shorter than R and at larger distances decays in a spherically symmetric way. The characteristic length r_0 for the decay of the potential in the radial direction can be found by equating the screened T-F potential of Eq. (5.16) to the unscreened Coulomb potential $\sim \sigma R^2/r$, where r is the radial distance from the center of the disk. This process gives

$$\bar{r}_0 \sim 1/(\alpha^2\bar{\sigma}\bar{R}^2) \gg \bar{R}. \tag{5.19}$$

As in the previous case, the renormalized charge $\bar{q} \sim 1/\alpha$. Here, however, one can think that the screening electronic charge resides in a ball of size $\sim r_0$ around the disk rather than in a flat layer. This situation is shown schematically in Fig. 5.3c.

$\alpha \ll 1/(\bar{\sigma}\bar{R}^2)$

Finally, if α is made so small that $\alpha \ll 1/(\bar{\sigma}\bar{R}^2)$, the characteristic decay length r_0 of the T-F potential becomes much larger than the distance r_{TF} over which T-F screening is applicable. This implies that the potential is roughly uniform within the range of T-F screening, and therefore that the disk charge is not significantly screened. In other words, $q \sim \sigma R^2$. This situation is shown schematically in Fig. 5.3d.

5.6.2 Capacitance of a graphene stack

Given the picture of Fig. 5.3 for the screening atmosphere surrounding each disk of charge, one can calculate the capacitance of the GS based on the repulsive energy between disks. Naturally, this energy depends both on the density of the disks (which increases with increasing voltage) and on the value of α, which determines the nature of the screening atmosphere surrounding each disk.

In the following subsections we calculate the capacitance $C(V)$ over the two highest ranges of α, namely $\alpha \gg 1/\bar{R}$ and $1/\bar{R} \ll \alpha \ll 1/(\bar{\sigma}^{1/2}\bar{R}^{3/2})$, which correspond to quadrants a and b of Fig. 5.3. A wealth of different behaviors are demonstrated, as shown in Fig. 5.4. We close this subsection by commenting on the behavior of the capacitance at even smaller α.

$\alpha \gg 1/\bar{R}$

When α is sufficiently large that $\alpha \gg 1/\bar{R}$, each disk of charge draws around itself a disk-shaped screening atmosphere of thickness $\bar{z}_{TF} \sim \sqrt{\bar{R}/\alpha} \ll \bar{R}$ and width $\sim R$, as described in Sec. 5.6.1. When the capacitor is given only a small charge, such that the density N of these disks per unit volume is small enough that $N \ll 1/(R^2 z_{TF})$, the capacitor charge consists of a dilute gas of disks with volume density N and effective charge q neutralized by a uniform background of electronic charge with charge density $-qN$, as discussed in Sec. 5.5. At such low densities the capacitance is dominated by the quantum kinetic energy of the uniform electronic charge, $\bar{\mathbb{U}}_k \sim \bar{N}^{3/2}\bar{R}^{3/4}/\alpha^{7/4}$. The resulting capacitance is

$$\bar{\mathbb{C}}(\bar{V}) \sim \alpha^{7/2}\bar{\sigma}^3\bar{R}^{9/2}\bar{V}, \qquad \left(\bar{V} \ll \frac{1}{\alpha^{3/2}\bar{\sigma}\bar{R}^{5/2}}\right) \tag{5.20}$$

as in Eq. (5.13).

When the capacitor charge is made larger, such that the density of disks $N \gg 1/(R^2 z_{TF})$, the nonlinear screening atmospheres of adjacent disks overlap, and the capacitance is dominated by the staging energy discussed in Sec. 5.4. Thus, the capacitance is described by Eq. (5.11):

$$\bar{\mathbb{C}}(\bar{V}) \sim \frac{\alpha^{4/5}\bar{\sigma}^{6/5}}{\bar{V}^{4/5}}, \qquad \left(\frac{1}{\alpha^{3/2}\bar{\sigma}\bar{R}^{5/2}} \ll \bar{V} \ll \frac{\bar{\sigma}^{2/3}}{\alpha^{2/3}}\right). \tag{5.21}$$

The upper limit for the voltage in Eq. (5.21) comes from the requirement that $N \ll 1/(R^2 z_0)$, which is necessary for the assumption that only nearest-neighbor interactions between disks are important.

On the other hand, when the capacitor charge is so large that the concentration of disks $N \gg 1/(R^2 z_0)$, the distance between disks is much smaller than the characteristic decay length z_0 of the potential. This implies that the electron charge becomes roughly uniform throughout the GS. In this limit the quantum kinetic energy $\mathbb{U}_k$ of electrons again dominates the total energy. Unlike at small voltage, however, in this dense limit there is no concept of renormalized charge, since the space between neighboring disks is much smaller than any screening length. Thus at large voltages the capacitance returns to the conventional quantum expression:

$$\bar{\mathbb{C}}(\bar{V}) = \alpha \bar{V}^2, \qquad \left(\frac{\bar{\sigma}^{2/3}}{\alpha^{2/3}} \ll \bar{V} < \frac{\bar{\sigma}^{1/2}}{\alpha} \right). \tag{5.22}$$

The upper limit on voltage in Eq. (5.22) comes from the requirement that $N < 1/(R^2 c)$, which is the maximum possible steric filling of the electrode by ions.

The three regimes of voltage, as characterized by Eqs. (5.20) – (5.22), are depicted in Fig. 5.4a. Notice that in the derivation of these results it was not necessary to assume ordering of the graphene sheets over distances larger than R. Indeed, the low- and high-density results of Eqs. (5.20) and (5.22) assume only that the density of graphene sheets is roughly uniform throughout the GS, while Eq. (5.21) is based on disks interacting over a distance $z \ll z_{TF} \ll R$. Therefore, our earlier assumption of long-range ordering of the GS does not significantly alter any results. Notice also that when $\alpha, \bar{\sigma} \sim 1$ the range of validity of Eq. (5.22) collapses, and we regain the picture of Fig. 5.2.

$1/\bar{R} \ll \alpha \ll 1/(\bar{\sigma}^{1/2} \bar{R}^{3/2})$

When α is small enough that $\alpha \ll 1/\bar{R}$ but still large enough that $\alpha \gg 1/(\bar{\sigma}^{1/2} \bar{R}^{3/2})$, the nonlinear screening atmosphere surrounding each disk is spherical in shape with radius $\bar{r}_{TF} \sim 1/\alpha$ and encloses a total charge $q \sim 1/\alpha$, as indicated in Fig. 5.3b. When the capacitor charge is small enough that the density of disks $N \ll 1/r_{TF}^3$, the nonlinear screening atmospheres of neighboring disks do not overlap. In this case, then, similar to the low-density limit of large α, the capacitor charge consists of a dilute gas of disks

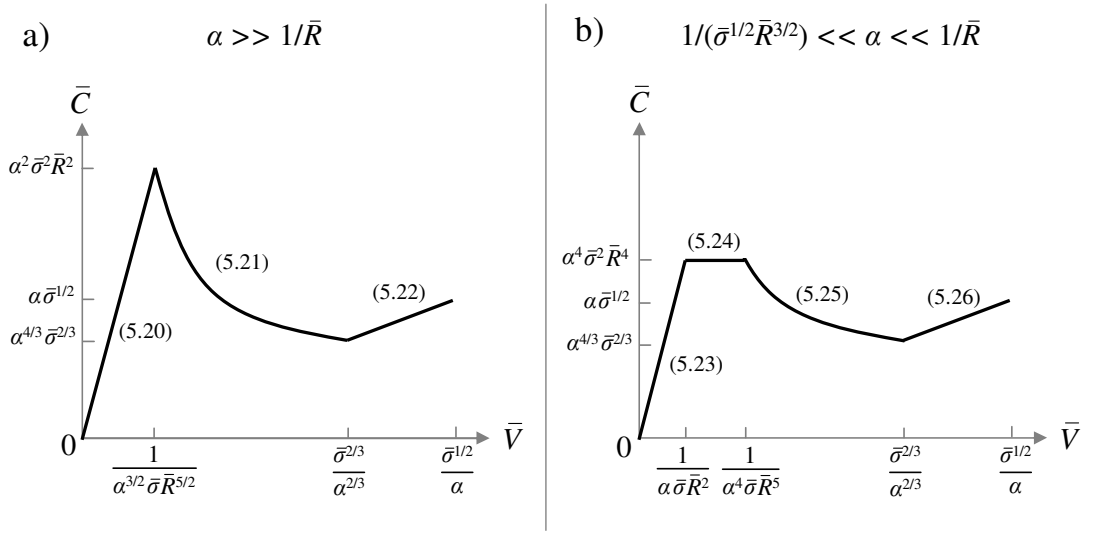

Figure 5.4: Schematic depiction of the capacitance $\bar{\mathbb{C}}$ as a function of voltage $\bar{V}$, shown for the two largest regimes of α (a and b). Each distinct range of voltage is labeled by the formula that describes the capacitance in that range. Important values of $\bar{V}$ and $\bar{\mathbb{C}}$ are labeled on their respective axes. The x and y axes have been somewhat distorted in order to clearly show the different ranges.

with volume density N and effective charge e/α neutralized by a uniform background of electronic charge with charge density $-eN/\alpha$. The capacitance in this limit is again dominated by the quantum kinetic energy of the uniform electron charge, which yields

$$\bar{\mathbb{C}}(\bar{V}) \sim \alpha^5\bar{\sigma}^5\bar{R}^6\bar{V}, \qquad \left(\bar{V} \ll \frac{1}{\alpha\bar{\sigma}\bar{R}^2}\right). \tag{5.23}$$

This result for capacitance is somewhat smaller than that of the low voltage limit for $\alpha \gg 1/\bar{R}$ [Eq. (5.20)]. This can be seen as a direct consequence of the reduced effectiveness of T-F screening implied by smaller α. Nonetheless Eq. (5.23) still represents a significant enhancement over the mean-field result of Eq. (5.7).

When N is large enough that $N \gg 1/r_{TF}^3$, the nonlinear screening atmospheres of the disks begin to overlap. If N remains small enough that $N \ll 1/R^3$, then the distance between neighboring disks is much larger than R and the two disks repel each other via the spherically symmetric potential of Eq. (5.16). In order to determine the repulsive energy $u(r)$ between them, where r is the distance between disks, one can calculate the pressure at the midplane between them, as in the derivation of Eq. (5.21). This pressure

has two components: the quantum kinetic energy of electrons at the midplane $\sim \bar{n}_m^{3/2}/\alpha$ and the electric field energy density $\sim \varepsilon_0\varepsilon(\vec{\nabla}\phi)^2$. Integrating both of these over the midplane area gives a repulsive force $\sim 1/(\alpha^4\bar{r}^4)$, so that the repulsive energy between the disks is $\bar{u}(\bar{r}) \sim 1/(\alpha^4\bar{r}^3)$.

In their lowest energy state, the disks remain separated from each other by a distance $r \sim N^{-1/3}$, which gives a total energy per unit volume $\bar{\mathbb{U}} \sim \bar{N}^2/\alpha^4$. This result, $\mathbb{U} \propto N^2$, implies a *constant* capacitance

$$C(\bar{V}) \sim \alpha^4\bar{\sigma}^2\bar{R}^4, \qquad \left(\frac{1}{\alpha\bar{\sigma}\bar{R}^2} \ll \bar{V} \ll \frac{1}{\alpha^4\bar{\sigma}\bar{R}^5}\right). \tag{5.24}$$

When the density of disks becomes large enough that $N \gg 1/R^3$, the distance between disks becomes smaller than the disk size R, so that the interaction between disks becomes plane-like rather than point charge-like. This suggests that the interaction energy between disks takes the form of the $1/h^5$ interaction described in Sec. 5.6.2, and the capacitance is the same as in Eq. (5.21). Specifically,

$$\bar{\mathbb{C}}(\bar{V}) \sim \frac{\alpha^{4/5}\bar{\sigma}^{6/5}}{\bar{V}^{4/5}}, \qquad \left(\frac{1}{\alpha^4\bar{\sigma}\bar{R}^5} \ll \bar{V} \ll \frac{\bar{\sigma}^{2/3}}{\alpha^{2/3}}\right). \tag{5.25}$$

Finally, when disks are so dense that the space between them is much shorter than the characteristic decay length of the potential z_0, the electron charge becomes uniform throughout the electrode and the capacitance becomes equal to the mean-field value:

$$\bar{\mathbb{C}}(\bar{V}) = \alpha\bar{V}^2, \qquad \left(\frac{\bar{\sigma}^{2/3}}{\alpha^{2/3}} \ll \bar{V} < \frac{\bar{\sigma}^{1/2}}{\alpha}\right). \tag{5.26}$$

Very small α

Generally speaking, as α is reduced the capacitance becomes smaller. One can see this, for example, by examining parts a and b Fig. 5.4. All capacitance scales in these plots are proportional to a positive power of α, so that reducing α reduces the capacitance. Further, when α is made smaller than $1/\bar{R}$ the strong maximum in capacitance associated with the transition from dilute to overlapping disks is eliminated. One can therefore expect additional reduction of the capacitance, particularly at small voltage, when α is even smaller than $1/(\bar{\sigma}^{1/2}\bar{R}^{3/2})$.

In principle, one can repeat the procedure of Secs. 5.6.2 and 5.6.2 for the cases c and d shown in Fig. 5.3, where $\alpha \ll 1/(\bar{\sigma}^{1/2}\bar{R}^{3/2})$. One finds a capacitance that continues to shrink and at small voltages approaches more closely the mean-field value $\bar{\mathbb{C}}(\bar{V}) \sim \alpha\bar{V}^2$. The results of this procedure are not presented here in detail, but they can easily be outlined conceptually.

In regime c, where $1/(\bar{\sigma}\bar{R}^2) \ll \alpha \ll 1/(\bar{\sigma}^{1/2}\bar{R}^{3/2})$ the characteristic decay length of the potential becomes larger than the disk size. This suggests that as the concentration of disks is increased the electron charge becomes uniform throughout the GS *before* the disks are strongly overlapping. As a result, there is no regime of voltage in which the disks interact like infinite planes, so that the regime where $C \propto V^{-4/5}$ shown in Fig. 5.4 a and b disappears. Rather, the capacitance in this range of α increases monotonically with voltage: at small voltages the capacitance increases linearly with V with a large slope, followed by a plateau of constant C, after which the capacitance follows the mean-field prediction $\bar{\mathbb{C}} \sim \alpha^2\bar{V}$.

Finally, in regime d, where α is so small that $\alpha \ll 1/(\bar{\sigma}\bar{R}^2)$, there is no significant screening of the disk charge at all. This implies that the regime of constant C disappears and the capacitance becomes equal to the mean-field value $\bar{\mathbb{C}} \sim \alpha^2\bar{V}$ everywhere. One might well have anticipated this result from the beginning, since $\alpha \to 0$ corresponds to the limit where the quantum kinetic energy dominates all Coulomb energies, so that screening is unimportant and the capacitance is determined solely by the energy required to raise the Fermi level in graphene.

5.7 Linear screening

In Secs. 5.5 and 5.6.1 we discussed the screening of a disk of charge in a graphene stack (GS), focusing primarily on the Thomas-Fermi (T-F) screening atmosphere surrounding each disk. Here we describe the relatively weakly-varying potential associated with linear screening outside the T-F region. In Sec. 5.7.1 we first calculate the potential surrounding a point charge in the GS under the assumptions of linear response theory. In Sec. 5.7.2 we show how this result guarantees that the Coulomb interaction between distant disks can be safely ignored.

5.7.1 Derivation of the linear potential

Consider the problem of a point charge q inside the GS, which has ordered graphene sheets layered in the z direction with spacing c. We take the point charge to be at the origin of a cylindrical coordinate system with radial and axial coordinates ρ and z. Under the random phase approximation, the potential $\phi(\rho, z)$ is determined by the dielectric function $\epsilon(k, k_z)$, where k and k_z are the Fourier wave vectors in the ρ and z directions. For distances $\sqrt{\rho^2 + z^2} \gg c$ from the point charge, one can describe the GS as a continuum, three-dimensional medium, so that the dielectric function is given by

$$\epsilon(k, k_z) = 1 - ev(k, k_z)\Pi(k, k_z). \tag{5.27}$$

Here, $v(k, k_z) = q/[\varepsilon_0\varepsilon(k^2 + k_z^2)]$ is the Fourier transform of the bare Coulomb potential $q/[4\pi\varepsilon_0\varepsilon(\rho^2 + z^2)]$ and $\Pi(k, k_z)$ is the polarization function. If adjacent graphene layers are assumed to have no electronic interlayer coupling (as in turbostratic graphite), then $\Pi(k, k_z)$ is related to the polarization function of 2D monolayer graphene, Π_{2D}, simply by $\Pi(k, k_z) = \Pi_{2D}(k)/c$.

The polarization function $\Pi_{2D}(k)$ has been previously calculated [127] to be

$$\Pi_{2D} = -\frac{1}{4}\frac{|k|}{\hbar v} = -\frac{\pi\alpha\varepsilon_0\varepsilon|k|}{e^2}, \tag{5.28}$$

where $\alpha = e^2/(4\pi\varepsilon_0\varepsilon\hbar v)$ is the effective fine structure constant of graphene. With this result one can define the potential $\tilde{\phi}(k, k_z)$ in Fourier space:

$$\tilde{\phi}(k, k_z) = \frac{v(k, k_z)}{\epsilon(k, k_z)} = \frac{q}{\varepsilon_0\varepsilon[k^2 + k_z^2 + (\pi\alpha q/e)(|k|/c)]} \simeq \frac{q}{\varepsilon_0\varepsilon[k_z^2 + (\pi\alpha q/e)(|k|/c)]}. \tag{5.29}$$

The last, approximate relation in Eq. (5.29) is valid for distances $\rho \gg c$, so that $k^2 \ll |k|/c$. Taking the Fourier transform of this equation gives the following result for the potential:

$$\phi(\rho, z) \simeq \frac{q}{4\pi\varepsilon_0\varepsilon c}\left[A_\rho^{-2/3}\frac{\rho}{c} + A_z^{-2/3}\frac{z^2}{c^2}\right]^{-3/2}, \tag{5.30}$$

where A_ρ and A_z are numeric coefficients of order unity, given by $A_\rho = \Gamma(3/4)^2/\sqrt{\pi^3\alpha}$ and $A_z = 4/(\pi^2\alpha^2)$. $\Gamma(x)$ is Euler's gamma function.

For the case of a disk of charge within the GS, Eq. (5.30) can be used to describe the potential outside the T-F screening atmosphere by substituting for q the renormalized

disk charge $q \sim e\sqrt{R/\alpha c}$. It is worth noting that, to within numerical coefficients, Eq. (5.30) smoothly matches the T-F result of Eq. (5.15) at the boundary of the T-F region. That is, Eqs. (5.15) and (5.30) are equal at the points $\rho = 0$, $z = z_{TF} \sim \sqrt{Rc/\alpha}$ and $z = 0$, $\rho \sim R$, which lie on the same equipotential contour. Thus the potential surrounding a charged disk can be described by the T-F result of Eq. (5.15) at $|z| < z_{TF}$, $\rho < R$ and by the linear response result of Eq. (5.30) otherwise, with no parametric intermediate regime.

5.7.2 Proof that the Coulomb energy is smaller than the quantum kinetic energy in the low-density limit

In Secs. 5.5 and 5.6 we calculated the capacitance and neglected the electrostatic energy associated with the configuration of positively-charged disks residing on a negatively-charged background. This approach was justified because when the density of disks N is smaller than $1/(R^2 z_{TF})$ the Coulomb energy is much smaller than the quantum kinetic energy associated with the uniform electron charge. Here, we explicitly prove this inequality, focusing on the most practically relevant case $\alpha \gg 1/\bar{R}$.

As explained in Sec. 5.5, when the density of disks is very small the capacitor charge consists of a sparse arrangement of charge-renormalized disks with charge q and density N surrounded by a uniform electron charge with density $-qN$. The quantum kinetic energy per unit volume associated with the uniform electron charge is

$$\bar{\mathbb{U}}_k \sim \bar{N}^{3/2}\bar{R}^{3/4}/\alpha^{7/4}. \tag{5.31}$$

Here we have used the dimensionless units described in Sec. 5.3.

In order to estimate the magnitude of the Coulomb energy, one can consider that in their lowest energy configuration, the disks form a correlated arrangement on the uniform background, such that the disks minimize their repulsive energy while maintaining the fixed concentration N. This arrangement is characterized by the average spacing between disks in the ρ and z directions, which we denote d_ρ and d_z, respectively. The repulsive interaction between disks is dictated by the linear potential given in Eq. (5.30). Since this potential is anisotropic, one can expect that the spacing between disks is also anisotropic. In other words, the minimum energy arrangement of disks constitutes an anisotropic Wigner crystal.

The distances d_ρ and d_z can be found by noting that in their minimum energy configuration, disks are arranged within the GS so that all nearest-neighbor interactions are equal in magnitude. This implies that d_ρ and d_z are determined by the relation $q\phi(d_\rho, 0) \sim q\phi(0, d_z)$. Since the density of ions $N \sim (d_\rho^2 d_z)^{-1}$, one can solve for d_ρ and d_z as a function of N. This process gives $\bar{d}_\rho \sim \alpha^{1/5}\bar{N}^{-2/5}$ and $\bar{d}_z \sim \alpha^{-2/5}\bar{N}^{-1/5}$, so that the typical nearest-neighbor interaction energy is $\bar{u}_{\rm nn} \sim \bar{q}^2\bar{\phi}(\bar{d}_\rho, 0) = \bar{q}^2\bar{\phi}(0, \bar{d}_z) \sim \bar{N}^{3/5}\bar{R}/\alpha^{9/5}$.

From the nearest-neighbor interaction energy $u_{\rm nn}$ one can estimate the total Coulomb energy of the anisotropic Wigner crystal. This total energy is, in fact, negative, as in the case of an ordinary isotropic Wigner crystal, since the attraction of each disk to its cell of negative background charge is stronger than the repulsion between neighboring disks. The magnitude of the Coulomb energy per disk is similar in magnitude to the nearest-neighbor interaction energy $\bar{u}_{\rm nn}$. Therefore the total Coulomb energy per unit volume $\bar{\mathbb{U}}_{el} \sim -N u_{\rm nn}$, so that

$$\bar{\mathbb{U}}_{el} \sim -\bar{N}^{8/5}\bar{R}/\alpha^{9/5}. \tag{5.32}$$

Comparing Eqs. (5.31) and (5.32) suggests that $|\mathbb{U}_{el}| \ll |\mathbb{U}_k|$ whenever $\bar{N} \ll \sqrt{\alpha/\bar{R}^5} \sim 1/(\bar{R}^2\bar{z}_{TF})$. So our assumption that the Coulomb interaction is unimportant for the capacitance is justified.

Finally, even though the Coulomb energy of Eq. (5.32) is never larger than the quantum kinetic energy over the relevant range of voltage, $V \ll 1/(\alpha^{3/2}\bar{\sigma}\bar{R}^{5/2})$, one can nevertheless describe the correction that it produces to the main term of the capacitance, $\bar{\mathbb{C}}_k \sim \alpha^{7/2}\bar{\sigma}^3\bar{R}^{9/2}\bar{V}$. Specifically, since the Coulomb energy is negative and small, one can say that it produces a large negative capacitance $\mathbb{C}_{el}$ per unit volume that is added in series with the relatively smaller $\mathbb{C}_k$, so that $\mathbb{C} = (\mathbb{C}_k^{-1} + \mathbb{C}_{el}^{-1})^{-1}$. This negative capacitance $\mathbb{C}_{el}$ is an extension of the well-known "negative compressibility" of a conventional Wigner crystal [128]. Expanding for $|\mathbb{C}_{el}| \gg |\mathbb{C}_k|$ gives $\mathbb{C} \simeq \mathbb{C}_k(1 - \mathbb{C}_k/\mathbb{C}_{el})$. Taking the appropriate derivatives of Eq. (5.32) gives $\bar{\mathbb{C}}_{el} \sim -\alpha^{16/5}\bar{\sigma}^{14/5}\bar{R}^4\bar{V}^{4/5}$, so that all together

$$\bar{\mathbb{C}} \sim \bar{\mathbb{C}}_k\left[1 + \left(\alpha^{3/2}\bar{\sigma}\bar{R}^{5/2}\bar{V}\right)^{1/5}\right]. \tag{5.33}$$

Notice that the correction term in Eq. (5.33) grows to order unity precisely at the crossover point $V \sim 1/(\alpha^{3/2}\bar{\sigma}\bar{R}^{5/2})$, where the T-F screening atmospheres of neighboring

disks begin to overlap and the capacitance transitions to the "staging" result $\mathbb{C} \propto V^{-4/5}$ of Eq. (5.11).

5.8 Discussion

In this chapter we have presented a theory of the capacitance of a graphene stack as a function of the capacitor voltage and the effective fine structure constant α. We have showed how large capacitance can result from the charge renormalization effected by T-F screening and explored the different physically interesting regimes associated with small α. In this closing discussion we focus again on practical devices, for which $\alpha \sim 1$.

Most likely, in practical realizations of graphene supercapacitors, the sharp maximum of capacitance at small voltages shown in Fig. 5.2 will be somewhat smeared by temperature or by strong disorder in the graphene stack. Such disorder eliminates the positional correlations among disks of ionic charge when their density is low, leading to a somewhat larger average interaction energy between disks and therefore to smaller capacitance. In traditional graphite intercalation experiments, for example, the vertical ordering of charged planes generally disappears for vertical spacing $h \gtrsim 4c$ [129]. Nonetheless, the formulas of Sec. 5.6.2 suggest that even if correlations are lost at $h > 4c$ the capacitance may still reach values on the order of hundreds of F/cm^3, which is consistent with experiment.

Finally, our results suggest a capacitance that quickly reaches a maximum value with increasing voltage before slowly declining over a much larger voltage range. This is much more compatible with experiment than the traditional mean-field prediction of Sec. 5.3. Experiments on graphene EDLCs generally report a capacitance that varies only slightly with voltage and retains a value of several hundreds of F/cm^3 over several volts [11, 113, 114, 115, 116, 117, 118, 119]. This is in direct contradiction to the mean-field prediction, which says that the capacitance should collapse at small voltage and rise to its maximum value of ~ 100 F/cm^3 only after V has increased to several volts. This large discrepancy can be taken as an indication that nonlinear screening of the ionic charge indeed plays an important role in creating the unusually large capacitance of graphene supercapacitors.

Chapter 6

Conclusions and Discussion

In this thesis we have examined four types of capacitor devices, each of which exhibits surprisingly large capacitance. We have shown that in each case the dependence of the capacitance on applied voltage can be described by relatively simple analytical theories. Our theories rely on two crucial ingredients that are often neglected in mean-field approaches. The first is the description of the capacitor charge as an arrangement of discrete objects, whose repulsive interaction induces positional correlations. The second is the screening of these discrete charges by the conducting electrode. Taken together, these two ingredients allow one to understand the existence of large capacitance.

Before concluding, we briefly re-summarize the main results from each chapter of the thesis. For a capacitor made from a 2DEG next to a metal electrode, as considered in Ch. 2, the capacitor charge can be thought of as a correlated arrangement of electron-image dipoles. The resulting short-ranged interaction between these dipoles allows the capacitance per unit area to be as large as $\sim \varepsilon_0 \varepsilon / a_B$ when the 2DEG is sparse, so that the capacitance is not limited by the physical separation between the 2DEG and its countercharge. This large capacitance can be largely understood on the basis of a classical calculation, summarized in Fig. 2.3 and Eq. (1.5), and is confirmed by a more detailed quantum mechanical calculation, presented in Fig. 2.7.

For a capacitor made from an ionic liquid between metal electrodes, as examined in Ch. 3, the electric double-layer at each electrode can also be thought of as an arrangement of ion-image dipoles. The $1/r^3$ interaction between these dipoles leads to a capacitance that decays at large voltage as $C \propto V^{-1/3}$ and has a maximum value that

varies with temperature as $C_{max} \propto T^{-1/3}$. These dependencies are summarized in Eqs. (3.9) and (3.10), and are confirmed by Monte Carlo simulations, as shown in Figs. 3.1 and 3.2.

In Ch. 4 we consider a simple model of real supercapacitor devices, in which the electrode is filled with deep planar pores into which ions can enter when a voltage is applied. When the electrode is metallic, there is a strong, exponential screening of the repulsive interaction between ions, and this allows the capacitance per pore to be nearly an order of magnitude larger than the Helmholtz value. Our analytical theory, as summarized by Eqs. (4.9), (4.10), and (4.18), is confirmed by a Monte Carlo simulation, as shown in Fig. 4.4. When the electrode has a finite electronic screening radius, the capacitance is reduced. If the screening radius is larger than the distance between pores in the electrode, then the capacitor charge can be described as a 3D arrangement of correlated, Yukawa-interacting charges. The resulting capacitance is described by Eqs. (4.25), (4.32), and (4.38) and plotted as a function of voltage and screening radius in Fig. 4.9.

Finally, in Ch. 5 we examine a model of a capacitor made from a graphene stack, and we show that ionic charge enters the electrode collectively in the form of large disks. These disks become renormalized through nonlinear screening by the graphene, and this renormalization weakens their interaction and allows for capacitance that is much larger than what would be predicted based on the large quantum kinetic energy of electrons in graphene. The resulting capacitance is described at small voltages by Eq. (5.13) and at large voltages by Eq. (5.14), as shown in Fig. 5.2. A number of additional scaling regimes appear when the fine structure constant α is treated as a small parameter; these are summarized in Figs. 5.3 and 5.4.

Taken individually, each of these four chapters provides some new understanding of the operation of an experimentally-relevant device by presenting a description of the microscopic structure of the electronic charge within it and showing how this structure can lead to large capacitance. Perhaps more importantly, when taken together the four theories developed here establish a recipe for addressing the question "how large can the capacitance be?". In doing so, they provide insight that may prove instrumental in our search for new, efficient methods of electrical energy storage and they also shed light on an important question in fundamental physics.

References

[1] Shahriar Shafiee and Erkan Topal. When will fossil fuel reserves be diminished? *Energy Policy*, 37(1):181 – 189, 2009.

[2] Naomi Oreskes. The scientific consensus on climate change. *Science*, 306(5702):1686, 2004, http://www.sciencemag.org/content/306/5702/1686.full.pdf.

[3] William R. L. Anderegg, James W. Prall, Jacob Harold, and Stephen H. Schneider. Expert credibility in climate change. *Proceedings of the National Academy of Sciences*, 2010, http://www.pnas.org/content/early/2010/06/04/1003187107.full.pdf+html.

[4] George W. Crabtree and Nathan S. Lewis. Solar energy conversion. *Physics Today*, 60(3):37–42, 2007.

[5] Héctor D. Abruña, Yasuyuki Kiya, and Jay C. Henderson. Batteries and electrochemical capacitors. *Physics Today*, 61(12):43, 2008.

[6] B. E. Conway. *Electrochemical supercapacitors: scientific fundamentals and technological applications*. Springer, 1999.

[7] J. Schindall. The charge of the ultracapacitors. *Spectrum, IEEE*, 44(11):42 –46, 2007.

[8] R. Ktz, P.W. Ruch, and D. Cericola. Aging and failure mode of electrochemical double layer capacitors during accelerated constant load tests. *Journal of Power Sources*, 195(3):923 – 928, 2010.

[9] H. L. F. von Helmholtz. Ueber einige gesetze der vertheilung elektrischer strme in krperlichen leitern, mit anwendung auf die thierischelektrischen versuehe. *Ann. Phys. (Leipzig)*, 165:353, 1853.

[10] H. L. F. von Helmholtz. Some laws concerning the distribution of electric currents in volume conductors with applications to experiments on animal electricity. *P. IEEE*, 92(5):868 – 870, May 2004.

[11] Patrice Simon and Yury Gogotsi. Materials for electrochemical capacitors. *Nat. Mater.*, 7(11):845–854, November 2008.

[12] Alexei A. Kornyshev. Double-Layer in ionic liquids: paradigm change? *The Journal of Physical Chemistry B*, 111(20):5545–5557, May 2007.

[13] Lu Li, C. Richter, S. Paetel, T. Kopp, J. Mannhart, and R. C. Ashoori. Very large capacitance enhancement in a two-dimensional electron system. *Science*, 332(6031):825–828, 2011, http://www.sciencemag.org/content/332/6031/825.full.pdf.

[14] M. S. Bello, E. I. Levin, B. I. Shklovskii, and A. L. Efros. Density of localized states in the surface impurity band of a metal-insulator-semiconductor structure. *Sov. Phys. JETP*, 53:822, 1981.

[15] Serge Luryi. Quantum capacitance devices. *Applied Physics Letters*, 52(6):501–503, 1988.

[16] S. V. Kravchenko, D. A. Rinberg, S. G. Semenchinsky, and V. M. Pudalov. Evidence for the influence of electron-electron interaction on the chemical potential of the two-dimensional electron gas. *Phys. Rev. B*, 42(6):3741–3744, 1990.

[17] J. P. Eisenstein, L. N. Pfeiffer, and K. W. West. Negative compressibility of interacting two-dimensional electron and quasiparticle gases. *Physical Review Letters*, 68(5):674, February 1992.

[18] J. P. Eisenstein, L. N. Pfeiffer, and K. W. West. Compressibility of the two-dimensional electron gas: Measurements of the zero-field exchange energy and fractional quantum hall gap. *Phys. Rev. B*, 50(3):1760–1778, 1994.

[19] S. Shapira, U. Sivan, P. M. Solomon, E. Buchstab, M. Tischler, and G. Ben Yoseph. Thermodynamics of a charged fermion layer at high rs values. *Phys. Rev. Lett.*, 77(15):3181–3184, Oct 1996.

[20] S. C. Dultz and H. W. Jiang. Thermodynamic signature of a two-dimensional metal-insulator transition. *Phys. Rev. Lett.*, 84(20):4689–4692, 2000.

[21] S. Ilani, A. Yacoby, D. Mahalu, and Hadas Shtrikman. Unexpected behavior of the local compressibility near the $b =$ metal-insulator transition. *Phys. Rev. Lett.*, 84(14):3133–3136, Apr 2000.

[22] G. Allison, E. A. Galaktionov, A. K. Savchenko, S. S. Safonov, M. M. Fogler, M. Y. Simmons, and D. A. Ritchie. Thermodynamic density of states of two-dimensional gaas systems near the apparent metal-insulator transition. *Phys. Rev. Lett.*, 96(21):216407, 2006.

[23] B. I. Shklovskii and A. L. Efros. *JETP Lett.*, 44:669, 1987.

[24] A. L. Efros. Homogeneous and inhomogeneous states of a two-dimensional electron liquid in a strong magnetic field. *Phys. Rev. B*, 45(19):11354–11357, May 1992.

[25] A.L. Efros, F.G. Pikus, and V.G. Burnett. Thermodynamic density of states of two-dimensional electron gas in a strong magnetic field. *Solid State Communications*, 84(1-2):91 – 94, 1992. A Festschrift Issue of Solid State Communication to Pay Tribute to Professor Ellias Burstein.

[26] F. G. Pikus and A. L. Efros. Distribution of electron density and magnetocapacitance in the regime of the fractional quantum hall effect. *Phys. Rev. B*, 47(24):16395–16403, Jun 1993.

[27] Junren Shi and X. C. Xie. Droplet state and the compressibility anomaly in dilute 2d electron systems. *Phys. Rev. Lett.*, 88(8):086401, Feb 2002.

[28] Michael M. Fogler. Nonlinear screening and percolative transition in a two-dimensional electron liquid. *Phys. Rev. B*, 69(12):121409(R), 2004.

[29] A. L. Efros. Negative density of states: Screening, einstein relation, and negative diffusion. *Physical Review B*, 78(15):155130, oct 2008.

[30] Thilo Kopp and Jochen Mannhart. Calculation of the capacitances of conductors: Perspectives for the optimization of electronic devices. *J. Appl. Phys.*, 106(6):064504, 2009.

[31] D. Ceperley. Ground state of the fermion one-component plasma: A monte carlo study in two and three dimensions. *Phys. Rev. B*, 18(7):3126–3138, Oct 1978.

[32] L D Landau, L. P. Pitaevskii, and E.M. Lifshitz. *Electrodynamics of Continuous Media, Second Edition: Volume 8*. Butterworth-Heinemann, 2 edition, January 1984.

[33] Brian Skinner, M. S. Loth, and B. I. Shklovskii. Capacitance of the double layer formed at the metal/ionic-conductor interface: How large can it be? *Phys. Rev. Lett.*, 104(12):128302, Mar 2010.

[34] M. S. Loth, Brian Skinner, and B. I. Shklovskii. Non-mean-field theory of anomalously large double layer capacitance. *Physical Review E*, 82(1):016107, July 2010.

[35] M. S. Loth, Brian Skinner, and B. I. Shklovskii. Anomalously large capacitance of an ionic liquid described by the restricted primitive model. *Phys. Rev. E*, 82(5):056102, Nov 2010.

[36] A. Widom and R. Tao. Coulomb energy and correlations of inversion-layer electrons in metal-oxide-semiconductor field-effect transistor devices. *Phys. Rev. B*, 38(15):10787–10790, 1988.

[37] J. Topping. On the mutual potential energy of a plane network of doublets. *Proceedings of the Royal Society of London. Series A, Containing Papers of a Mathematical and Physical Character*, 114(766):67–72, February 1927. ArticleType: research-article / Full publication date: Feb. 1, 1927 / Copyright 1927 The Royal Society.

[38] G. Goldoni and F. M. Peeters. Stability, dynamical properties, and melting of a classical bilayer wigner crystal. *Physical Review B*, 53(8):4591, February 1996.

[39] G. F. Giuliani and G. Vignale. *Quantum Theory of the Electron Liquid*. Cambridge University Press, Cambridge, 2005.

[40] Lorenzo Zecca, Paola Gori-Giorgi, Saverio Moroni, and Giovanni B. Bachelet. Local density functional for the short-range part of the electron-electron interaction. *Phys. Rev. B*, 70(20):205127, 2004.

[41] D. Ceperley, G. V. Chester, and M. H. Kalos. Monte carlo simulation of a many-fermion study. *Phys. Rev. B*, 16(7):3081–3099, 1977.

[42] Jilin Xia, Fang Chen, Jinghong Li, and Nongjian Tao. Measurement of the quantum capacitance of graphene. *Nat. Nano*, 4(8):505–509, 2009.

[43] A. F. Young, C. R. Dean, I. Meric, S. Sorgenfrei, H. Ren, K. Watanabe, T. Taniguchi, J. Hone, K. L. Shepard, and P. Kim. Electronic compressibility of gapped bilayer graphene. (unpublished), 1004.5556.

[44] L. A. Ponomarenko, R. Yang, R. V. Gorbachev, P. Blake, A. S. Mayorov, K. S. Novoselov, M. I. Katsnelson, and A. K. Geim. Density of states and zero landau level probed through capacitance of graphene. *Phys. Rev. Lett.*, 105(13):136801, Sep 2010.

[45] B. Tanatar and D. M. Ceperley. Ground state of the two-dimensional electron gas. *Phys. Rev. B*, 39(8):5005–5016, 1989.

[46] Claudio Attaccalite, Saverio Moroni, Paola Gori-Giorgi, and Giovanni B. Bachelet. Correlation energy and spin polarization in the 2d electron gas. *Phys. Rev. Lett.*, 88(25):256601, 2002.

[47] Paola Gori-Giorgi, Saverio Moroni, and Giovanni B. Bachelet. Pair-distribution functions of the two-dimensional electron gas. *Phys. Rev. B*, 70(11):115102, 2004.

[48] Brian Skinner and B. I. Shklovskii. Anomalously large capacitance of a plane capacitor with a two-dimensional electron gas. *Phys. Rev. B*, 82(15):155111, Oct 2010.

[49] A. D. Meyertholen and M. M. Fogler. Biexcitons in two-dimensional systems with spatially separated electrons and holes. *Phys. Rev. B*, 78:235307, 2008.

[50] Jan R. Engelbrecht, Mohit Randeria, and Lizeng Zhang. Landau f function for the dilute fermi gas in two dimensions. *Phys. Rev. B*, 45(17):10135–10138, 1992.

[51] Mohit Randeria, Ji-Min Duan, and Lih-Yir Shieh. Superconductivity in a two-dimensional fermi gas: Evolution from cooper pairing to bose condensation. *Phys. Rev. B*, 41(1):327–343, 1990.

[52] Paola Gori-Giorgi, Francesco Sacchetti, and Giovanni B. Bachelet. Analytic static structure factors and pair-correlation functions for the unpolarized homogeneous electron gas. *Phys. Rev. B*, 61(11):7353–7363, 2000.

[53] John P. Perdew and Yue Wang. Accurate and simple analytic representation of the electron-gas correlation energy. *Phys. Rev. B*, 45(23):13244–13249, Jun 1992.

[54] Michael M. Fogler. Ground-state energy of the electron liquid in ultrathin wires. *Phys. Rev. Lett.*, 94(5):056405, 2005.

[55] Boris Spivak and Steven A. Kivelson. Transport in two dimensional electronic micro-emulsions. *Ann. Phys.*, 321(9):2071 – 2115, 2006.

[56] Jian Huang, J. S. Xia, D. C. Tsui, L. N. Pfeiffer, and K. W. West. Disappearance of metal-like behavior in gaas two-dimensional holes below 30 mk. *Phys. Rev. Lett.*, 98(22):226801, 2007.

[57] L. H. Ho, W. R. Clarke, A. P. Micolich, R. Danneau, O. Klochan, M. Y. Simmons, A. R. Hamilton, M. Pepper, and D. A. Ritchie. Effect of screening long-range coulomb interactions on the metallic behavior in two-dimensional hole systems. *Phys. Rev. B*, 77(20):201402(R), 2008.

[58] L. A. Tracy, E. H. Hwang, K. Eng, G. A. Ten Eyck, E. P. Nordberg, K. Childs, M. S. Carroll, M. P. Lilly, and S. Das Sarma. Observation of percolation-induced two-dimensional metal-insulator transition in a si mosfet. *Phys. Rev. B*, 79(23):235307, 2009.

[59] L. H. Ho, A. P. Micolich, A. R. Hamilton, and O. P. Sushkov. Ground-plane screening of coulomb interactions in two-dimensional systems: How effectively can one two-dimensional system screen interactions in another. *Phys. Rev. B*, 80(15):155412, 2009.

[60] S. Dröscher, P. Roulleau, F. Molitor, P. Studerus, C. Stampfer, K. Ensslin, and T. Ihn. Quantum capacitance and density of states of graphene. *Appl. Phys. Lett.*, 96(15):152104, 2010.

[61] E. A. Henriksen and J. P. Eisenstein. Measurement of the electronic compressibility of bilayer graphene. *Phys. Rev. B*, 82(4):041412(R), 2010.

[62] Jian Huang, D. S Novikov, D. C Tsui, L. N Pfeiffer, and K. W West. Interaction effects in the transport of two-dimensional holes in GaAs. *cond-mat/0610320*, October 2006.

[63] C. C. Grimes and G. Adams. Evidence for a Liquid-to-Crystal phase transition in a classical, Two-Dimensional sheet of electrons. *Physical Review Letters*, 42(12):795, March 1979.

[64] Denis Konstantinov and Kimitoshi Kono. Photon-induced vanishing of magnetoconductance in 2d electrons on liquid helium. *Phys. Rev. Lett.*, 105(22):226801, Nov 2010.

[65] M. Sing, G. Berner, K. Goß, A. Müller, A. Ruff, A. Wetscherek, S. Thiel, J. Mannhart, S. A. Pauli, C. W. Schneider, P. R. Willmott, M. Gorgoi, F. Schäfers, and R. Claessen. Profiling the interface electron gas of $laalo3/srtio3$ heterostructures with hard x-ray photoelectron spectroscopy. *Phys. Rev. Lett.*, 102(17):176805, Apr 2009.

[66] Zhicheng Zhong, P. X. Xu, and Paul J. Kelly. Polarity-induced oxygen vacancies at $laalo3?srtio3$ interfaces. *Phys. Rev. B*, 82(16):165127, Oct 2010.

[67] Wolter Siemons, Mark Huijben, Guus Rijnders, Dave H. A. Blank, Theodore H. Geballe, Malcolm R. Beasley, and Gertjan Koster. Dielectric-permittivity-driven charge carrier modulation at oxide interfaces. *Phys. Rev. B*, 81(24):241308, Jun 2010.

[68] O. Copie, V. Garcia, C. Bödefeld, C. Carrétéro, M. Bibes, G. Herranz, E. Jacquet, J.-L. Maurice, B. Vinter, S. Fusil, K. Bouzehouane, H. Jaffrès, and A. Barthélémy. Towards two-dimensional metallic behavior at $laalo3/srtio3$ interfaces. *Phys. Rev. Lett.*, 102(21):216804, May 2009.

[69] E. V. Bursian, Ya. G. Girshberg, and E. N. Starov. Small polarons in conducting barium titanate crystals. *physica status solidi (b)*, 46(2):529–533, 1971.

[70] W Meevasana, X J Zhou, B Moritz, C-C Chen, R H He, S-I Fujimori, D H Lu, S-K Mo, R G Moore, F Baumberger, T P Devereaux, D van der Marel, N Nagaosa, J Zaanen, and Z-X Shen. Strong energymomentum dispersion of phonon-dressed carriers in the lightly doped band insulator srtio 3. *New Journal of Physics*, 12(2):023004, 2010.

[71] Maciej Galinski, Andrzej Lewandowski, and Izabela Stepniak. Ionic liquids as electrolytes. *Electrochimica Acta*, 51(26):5567–5580, August 2006.

[72] John O'M. Bockris, Amulya K.N. Reddy, and Maria E. Gamboa-Aldeco. *Modern Electrochemistry 2A: Fundamentals of Electrodics*. Springer, 2nd edition, January 2001.

[73] M. Gouy. Sur la constitution de la charge lectrique la surface d'un lectrolyte. *Journal de Physique Thorique et Applique*, 9(1):12, 1910.

[74] David Leonard Chapman. LI. a contribution to the theory of electrocapillarity. *Philosophical Magazine Series 6*, 25(148):475, 1913.

[75] O. Stern. Zur theorie der elektrolytischen doppelschicht. *Zeitschrift fr Elektrochemie*, 30:508–516, 1924.

[76] Dezso Boda, Douglas Henderson, Kwong-Yu Chan, and Darsh T. Wasan. Low temperature anomalies in the properties of the electrochemical interface. *Chemical Physics Letters*, 308(5-6):473–478, July 1999.

[77] Dezso Boda, Douglas Henderson, and Kwong-Yu Chan. Monte carlo study of the capacitance of the double layer in a model molten salt. *The Journal of Chemical Physics*, 110(11):5346, 1999.

[78] Maxim V. Fedorov and Alexei A. Kornyshev. Ionic liquid near a charged wall: Structure and capacitance of electrical double layer. *The Journal of Physical Chemistry B*, 112(38):11868–11872, 2008.

[79] Michael B. Partenskii and Peter C. Jordan. Limitations and strengths of uniformly charged double-layer theory: Physical significance of capacitance anomalies. *Physical Review E*, 77(6):061117, June 2008.

[80] Stanislaw Lamperski and Jacek Klos. Grand canonical monte carlo investigations of electrical double layer in molten salts. *The Journal of Chemical Physics*, 129(16):164503, 2008.

[81] Stanislaw Lamperski, Christopher W. Outhwaite, and Lutful B. Bhuiyan. The electric Double-Layer differential capacitance at and near zero surface charge for a restricted primitive model electrolyte. *The Journal of Physical Chemistry B*, 113(26):8925–8929, July 2009.

[82] L. B. Bhuiyan, C. W. Outhwaite, D. Henderson, and M. Alawneh. A modified poissonboltzmann theory and monte carlo simulation study of surface polarization effects in the planar diffuse double layer. *Mol. Phys.*, 105:1395, 2007.

[83] M Pounds, S Tazi, M Salanne, and P A Madden. Ion adsorption at a metallic electrode: an ab initio based simulation study. *Journal of Physics: Condensed Matter*, 21(42):424109, 2009.

[84] Yan Levin and Michael E. Fisher. Criticality in the hard-sphere ionic fluid. *Physica A: Statistical and Theoretical Physics*, 225(2):164–220, March 1996.

[85] Md. Mominul Islam, Muhammad Tanzirul Alam, and Takeo Ohsaka. Electrical Double-Layer structure in ionic liquids: A corroboration of the theoretical model by experimental results. *The Journal of Physical Chemistry C*, 112(42):16568–16574, October 2008.

[86] Md. Mominul Islam, Muhammad Tanzirul Alam, Takeyoshi Okajima, and Takeo Ohsaka. Electrical double layer structure in ionic liquids: An understanding of the unusual CapacitancePotential curve at a nonmetallic electrode. *The Journal of Physical Chemistry C*, 113(9):3386–3389, March 2009.

[87] Vera Lockett, Rossen Sedev, John Ralston, Mike Horne, and Theo Rodopoulos. Differential capacitance of the electrical double layer in Imidazolium-Based ionic

liquids: Influence of potential, cation size, and temperature. *The Journal of Physical Chemistry C*, 112(19):7486–7495, May 2008.

[88] J. S. Wilkes and M. J. Zaworotko. Air and water stable 1 - ethyl - 3 - methylimidazolium based ionic liquids. *J. Chem. Soc. Chem. Commun*, 13:965967, 1992.

[89] Patrice Simon and Yury Gogotsi. Charge storage mechanism in nanoporous carbons and its consequence for electrical double layer capacitors. *Phil. Trans. R. Soc. A*, 368(1923):3457–3467, 2010.

[90] Zhiyong Wang, Fan Li, Nicholas S. Ergang, and Andreas Stein. Effects of hierarchical architecture on electronic and mechanical properties of nanocast monolithic porous carbons and carboncarbon nanocomposites. *Chemistry of Materials*, 18(23):5543–5553, 2006.

[91] R. Signorelli, D.C. Ku, J.G. Kassakian, and J.E. Schindall. Electrochemical double-layer capacitors using carbon nanotube electrode structures. *P. IEEE*, 97(11):1837 –1847, 2009.

[92] Celine Largeot, Cristelle Portet, John Chmiola, Pierre-Louis Taberna, Yury Gogotsi, and Patrice Simon. Relation between the ion size and pore size for an electric double-layer capacitor. *J. Am. Chem. Soc.*, 130(9):2730–2731, 2008.

[93] G. M. Torrie, J. P. Valleau, and G. N. Patey. Electrical double layers. ii. monte carlo and hnc studies of image effects. *J. Chem. Phys.*, 76(9):4615–4622, 1982.

[94] M. Alawneh, D. Henderson, C. W. Outhwaite, and L. B. Bhuiyan. The effect of dielectric polarization of the electrode on anomalous temperature effects in the electrical double layer. *Mol. Sim.*, 34:501, 2008.

[95] Christopher W. Outhwaite, Stanislaw Lamperski, and Lutful Bari Bhuiyan. Influence of electrode polarization on the capacitance of an electric double layer at and around zero surface charge. *Mol. Phys.*, 109:21, 2011.

[96] J. Chmiola, G. Yushin, Y. Gogotsi, C. Portet, P. Simon, and P. L. Taberna. Anomalous Increase in Carbon Capacitance at Pore Sizes Less Than 1 Nanometer. *Science*, 313(5794):1760–1763, 2006.

[97] Jingsong Huang, Bobby G. Sumpter, and Vincent Meunier. A universal model for nanoporous carbon supercapacitors applicable to diverse pore regimes, carbon materials, and electrolytes. *Chem. Eur. J.*, 14(22):6614–6626, 2008.

[98] A. A. Koulakov and B. I. Shklovskii. Charging spectrum and configurations of a wigner crystal island. *Phys. Rev. B*, 57(4):2352–2367, Jan 1998.

[99] T. H. Oosterkamp, J. W. Janssen, L. P. Kouwenhoven, D. G. Austing, T. Honda, and S. Tarucha. Maximum-density droplet and charge redistributions in quantum dots at high magnetic fields. *Phys. Rev. Lett.*, 82(14):2931–2934, Apr 1999.

[100] S. Kondrat and A. Kornyshev. Superionic state in double-layer capacitors with nanoporous electrodes. *J. Phys.: Condens. Matter*, 23:022201, 2011.

[101] William Ralph Smythe. *Static and Dynamic Electricity.* McGraw-Hill, 1 edition, 1939.

[102] Daan Frenkel and Berend Smit. *Understanding Molecular Simulation, Second Edition: From Algorithms to Applications.* Academic Press, 2 edition, November 2001.

[103] John P. Valleau and L. Kenneth Cohen. Primitive model electrolytes. i. grand canonical monte carlo computations. *J. Chem. Phys.*, 72(11):5935, 1980.

[104] John P. Valleau, L. Kenneth Cohen, and Damon N. Card. Primitive model electrolytes. II. the symmetrical electrolyte. *J. Chem. Phys.*, 72(11):5942, 1980.

[105] M. S. Loth and B. I. Shklovskii. Non-mean-field screening by multivalent counterions. *J. Phys.: Condens. Matter*, 21:424104, 2009.

[106] R. Zhang and B. I. Shklovskii. Phase diagram of aggregation of oppositely charged colloids in salty water. *Phys. Rev. E*, 69(2):021909, Feb 2004.

[107] Rui Zhang and B. I. Shklovskii. The pulling force of a single dna molecule condensed by spermidine. *Physica A*, 349(3-4):563 – 570, 2005.

[108] Brian Skinner and B.I. Shklovskii. Non-monotonic swelling of a macroion due to correlation-induced charge inversion. *Physica A*, 388(1):1 – 8, 2009.

[109] H. Gerischer. An interpretation of the double layer capacity of graphite electrodes in relation to the density of states at the fermi level. *J. Phys. Chem.*, 89:4249–4251, 1985.

[110] L. Pietronero, S. Strässler, H. R. Zeller, and M. J. Rice. Charge distribution in c direction in lamellar graphite acceptor intercalation compounds. *Phys. Rev. Lett.*, 41(11):763–767, Sep 1978.

[111] F. Guinea. Charge distribution and screening in layered graphene systems. *Phys. Rev. B*, 75(23):235433, Jun 2007.

[112] Mikito Koshino. Interlayer screening effect in graphene multilayers with *aba* and *abc* stacking. *Phys. Rev. B*, 81(12):125304, Mar 2010.

[113] Li Li Zhang, Rui Zhou, and X. S. Zhao. Graphene-based materials as supercapacitor electrodes. *J. Mater. Chem.*, 20:5983–5992, 2010.

[114] Kai Zhang, Li Li Zhang, X. S. Zhao, and Jishan Wu. Graphene/polyaniline nanofiber composites as supercapacitor electrodes. *Chemistry of Materials*, 22(4):1392–1401, 2010, http://pubs.acs.org/doi/pdf/10.1021/cm902876u.

[115] Tae Young Kim, Hyun Wook Lee, Meryl Stoller, Daniel R. Dreyer, Christopher W. Bielawski, Rodney S. Ruoff, and Kwang S. Suh. High-performance supercapacitors based on poly(ionic liquid)-modified graphene electrodes. *ACS Nano*, 5(1):436–442, 2011, http://pubs.acs.org/doi/pdf/10.1021/nn101968p.

[116] Meryl D. Stoller, Sungjin Park, Yanwu Zhu, Jinho An, and Rodney S. Ruoff. Graphene-based ultracapacitors. *Nano Letters*, 8(10):3498–3502, 2008, http://pubs.acs.org/doi/pdf/10.1021/nl802558y. PMID: 18788793.

[117] Yan Wang, Zhiqiang Shi, Yi Huang, Yanfeng Ma, Chengyang Wang, Mingming Chen, and Yongsheng Chen. Supercapacitor devices based on graphene materials. *The Journal of Physical Chemistry C*, 113(30):13103–13107, 2009, http://pubs.acs.org/doi/pdf/10.1021/jp902214f.

[118] S. Vivekchand, Chandra Rout, K. Subrahmanyam, A. Govindaraj, and C. Rao. Graphene-based electrochemical supercapacitors. *Journal of Chemical Sciences*, 120:9–13, 2008. 10.1007/s12039-008-0002-7.

[119] Yanwu Zhu, Shanthi Murali, Meryl D. Stoller, K. J. Ganesh, Weiwei Cai, Paulo J. Ferreira, Adam Pirkle, Robert M. Wallace, Katie A. Cychosz, Matthias Thommes, Dong Su, Eric A. Stach, and Rodney S. Ruoff. Carbon-based supercapacitors produced by activation of graphene. *Science*, 332(6037):1537–1541, 2011, http://www.sciencemag.org/content/332/6037/1537.full.pdf.

[120] Leonardo Spanu, Sandro Sorella, and Giulia Galli. Nature and strength of interlayer binding in graphite. *Phys. Rev. Lett.*, 103(19):196401, Nov 2009.

[121] Tatsumi Ishihara, Yuji Yokoyama, Futoshi Kozono, and Hidemi Hayashi. Intercalation of pf6- anion into graphitic carbon with nano pore for dual carbon cell with high capacity. *Journal of Power Sources*, 196(16):6956 – 6959, 2011. 15th International Meeting on Lithium Batteries (IMLB).

[122] S. A. Safran. Phase diagrams for staged intercalation compounds. *Phys. Rev. Lett.*, 44(14):937–940, Apr 1980.

[123] S. A. Safran and D. R. Hamann. Electrostatic interactions and staging in graphite intercalation compounds. *Phys. Rev. B*, 22(2):606–612, Jul 1980.

[124] John E. Fischer and Thomas E. Thompson. Graphite intercalation compounds. *Physics Today*, 31:36, 1978.

[125] R. A. Huggins. *Advanced Batteries: Materials Science Aspects*. Springer Science, 2009.

[126] D. Fennell Evans and Håkan Wennerström. *The Colloidal Domain*. Wiley-VCH, 1999.

[127] Tsuneya Ando. Screening effect and impurity scattering in monolayer graphene. *Journal of the Physical Society of Japan*, 75(7):074716, 2006.

[128] Gerald D. Mahan. *Many Particle Physics*. Springer, 3nd edition, January 2000.

[129] J. R. Dahn. Phase diagram of $lixc6$. *Phys. Rev. B*, 44(17):9170–9177, Nov 1991.

Appendix A

Acronyms and List of Symbols

This appendix provides a summary of the most common acronyms and symbols that are used in the thesis.

A.1 Acronyms

Table A.1: Acronyms

Acronym	Meaning
2D	Two-Dimensional
2DEG	Two-Dimensional Electron Gas
3D	Three-Dimensional
EDL	Electric Double Layer
EDLC	Electric Double Layer Capacitor
GS	Graphene Stack
H-F	Hartree-Fock
MC	Monte Carlo (simulation)
RPM	Restricted Primitive Model
RTIL	Room Temperature Ionic Liquid
T-F	Thomas-Fermi

A.2 List of Symbols

Table A.2: List of Symbols

Symbol	Description	SI Units
a	ion diameter	m
a_B	effective Bohr radius	m
α	effective fine structure constant	unitless
A	area	m^2
$\mathbb{A}$	specific surface area (surface area per unit volume)	1/m
C	capacitance	F
C_H	Helmholtz capacitance, $C_H = 2\varepsilon_0\varepsilon/a$	F
$\mathscr{C}$	capacitance per unit area	F/m^2
$\mathbb{C}$	capacitance per unit volume	F/m^3
d	physical capacitor thickness	m
d^*	effective capacitor thickness	m
e	elementary charge, $e \sim 1.602 \times 10^{-9}$ C	C
ϵ	electron energy; $\epsilon(\vec{k})$ is the electron dispersion relation	J
ε	dielectric constant	unitless
ε_0	permittivity of free space, $\varepsilon_0 \approx 8.854 \times 10^{-12}$ F/m	F/m
F	Helmholtz free energy	J
$\mathscr{F}$	Helmholtz free energy per unit area	J/m^2
ϕ	electric potential	V
$\vec{k}$	wave vector	1/m
k_B	Boltzmann's constant, $k_B \approx 1.380 \times 10^{-23}$ J/K	J/K
k_F	Fermi wave vector	1/m
μ	chemical potential	J
μ_F	Fermi energy	J
n	2D electron/ion concentration	$1/m^2$
N	3D electron/ion concentration	$1/m^3$
ν	3D density of states	$1/(J\ m^3)$

Continued on next page

Table A.2 – continued from previous page

Symbol	Description	SI Units
q	charge (microscopic)	C
Q	capacitor charge	C
$\mathscr{Q}$	capacitor charge per unit area	C/m^2
$\mathbb{Q}$	capacitor charge per unit volume	C/m^3
r_s	electron screening radius	m
R_s	3D, volume-averaged electron screening radius	m
ρ_s	dimensionless screening parameter	unitless
$\tilde{\rho}_s$	variational parameter that labels the electron correlation function	unitless
σ	2D charge density	C/m^2
T	temperature	K
u	(microscopic) interaction energy between two charges	J
U	total system energy	J
$\mathscr{U}$	system energy per unit area	J/m^2
$\mathbb{U}$	system energy per unit volume	J/m^3
V	voltage	V
V_t	"threshold voltage" – voltage at which the capacitor charge is zero	V
$\mathbb{V}$	volume	m^3